Structural Investigation of Melatonin and its Metabolites as Possible Calmodulin Antagonists and Nitric Oxide Synthase Inhibitors

by

Douglas Pimlott

A thesis

presented to the University of Waterloo

in fulfillment of the

thesis requirement for the degree of

Master of Science

in

Chemistry

Waterloo, Ontario, Canada, 2020

AUTHOR'S DECLARATION

I hereby declare that I am the sole author of this thesis. This is a true copy of the thesis, including any required final revisions, as accepted by my examiners.

I understand that my thesis may be made electronically available to the public.

Abstract

Calmodulin (CaM) is a small, highly conserved and ubiquitous calcium (Ca^{2+})-sensing protein that coordinates signal transduction through interactions with over 300 target molecules. It is composed of N- and C-terminal globular domains separated by a central flexible linker region. Each domain contains two EF hands that each coordinate one Ca^{2+}. CaM exists primarily as either Ca^{2+}-deplete apo-CaM or Ca^{2+}-saturated holo-CaM. Ca^{2+} binding causes a conformational change that exposes hydrophobic regions within each domain which facilitates binding to various targets, although apo-CaM is also able to bind to certain molecular targets as well.

An important set of targets for CaM are the nitric oxide synthase (NOS) isozymes. NOS catalyzes the conversion of L-arginine to L-citrulline in the production of nitric oxide (•NO). There are three isoforms of mammalian NOS: neuronal NOS (nNOS), endothelial NOS (eNOS) and inducible (iNOS). All three isoforms possess an N-terminal oxygenase domain containing the active site and a C-terminal reductase domain containing binding sites for FAD, FMN and NADPH. CaM binds to a region situated between these two domains, enabling interdomain electron transfer *via* a highly dynamic process. Ca^{2+}-dependent nNOS and eNOS isoforms are expressed constitutively, whereas Ca^{2+}-independent iNOS is regulated transcriptionally and expressed transiently. NOS isozymes perform various biologically important functions yet represent important therapeutic targets for inhibition in certain cases of overexpression. In one such instance, the overexpression of nNOS and subsequent overproduction of •NO in the central nervous system have been implicated in the pathogenesis of many neurodegenerative conditions including ischemic brain injury and epilepsy.

One approach that has yielded success in the selective inhibition of nNOS is the use of CaM antagonists such as trifluoperazine (TFP). TFP is available commercially as an antipsychotic medication and is used to treat symptoms of schizophrenia. The strong nature of its antagonism towards CaM corresponds to high levels of cytotoxicity as TFP has been shown to negatively impact various cellular processes. There is some evidence suggesting that melatonin (aMT) and one of its metabolites, N1-acetyl-5-methoxykynuramine (AMK), act as CaM antagonists and are able to appreciably inhibit nNOS activity. These naturally occurring hormones could prove to be milder and less cytotoxic alternatives to TFP, yet their mechanism of action remains poorly understood. A structural understanding of how these compounds interact with CaM and nNOS are important in further elucidating their value as therapeutic agents.

We sought to evaluate the nature of these interactions, with a particular focus on AMK, using numerous biophysical techniques at saturating levels of Ca^{2+}. Far-UV CD, gel mobility assays and ITC experiments demonstrated that the association of aMT and AMK with CaM is very weak, as had been seen in previous studies with aMT alone. CD and SPR competition assays showed a subtle AMK-mediated selective reduction in complex formation between CaM and the CaM-binding domain peptide of nNOS. NMR solution structures of CaM bound to AMK revealed that the ligand does not cause significant conformational changes in the protein, with the globular domains retaining their orientational independence from one another. The strengths of residue-specific interactions with AMK were determined to be in the low millimolar range using ^{15}N-HSQC NMR titrations, with N- and C-terminal domains possessing comparable affinities. Likely binding surfaces were determined to be located primarily in the hydrophobic cavities within each domain. This was corroborated by molecular dynamics studies, in which the most stable binding modes occurred when AMK was localized hydrophobic patches in the N-

terminal domain. We propose that the inhibitory effects of AMK are likely the result of a modulation of cellular function *via* gentle antagonism of CaM. The low affinity of CaM-AMK complexation would suggest allosteric alteration of the CaM-nNOS complex rather than direct competition for the binding pockets of CaM.

Acknowledgements

I would like to thank my supervisor Dr. Guy Guillemette for his guidance over the course of my studies. I will always be grateful for his insight, leadership and sharp wit that has made working with him so enjoyable. I consider myself very fortunate to be among the many minds he has helped mould.

I would also like to thank my advisory committee members Dr. Thorsten Dieckmann and Dr. Elizabeth Meiering for their time and advice. Dr. Dieckmann was a supervisor in all but name, never hesitating to help with whatever NMR issues I might have, sparing me many headaches in the process. Dr. Meiering's input was always extremely helpful in steering the direction of the project. I would also like to thank Dr. Subha Kalyaanamoorthy for kindly helping me with computational work.

Many thanks to members of the Dieckmann and Meiering Lab, Kyle Piccolo, Volition La, Harmeen Deol and Jeff Palumbo for making the lab such a fun place to work. I would be remiss not to extend a special thanks to Kyle and Harmeen, who were very generous with their time in training me on various instruments. The contributions of 4th year students Victoria Robertson and Joe Bui to our project are also greatly appreciated.

I wish to extend profound gratitude to my family. There is no building without a foundation, and truly none of this would have been possible without them. I am especially thankful for Danyon, whose support has helped me overcome every obstacle. My studies would be immeasurably more difficult without her kindness and encouragement.

Table of Contents

AUTHOR'S DECLARATION ii
Abstract iii
Acknowledgements vi
List of Figures x
List of Tables xii
List of Abbreviations xiii
Chapter 1 Literature Review 1
1.1 Calcium Signalling Pathway 1
1.2 Calmodulin Overview 2
1.2.1 CaM Structure 3
1.2.2 CaM Binding to Target Proteins 5
1.3 Nitric Oxide Synthase 6
1.3.1 NOS Isoforms 7
1.3.2 Validation of nNOS as a Drug Target 10
1.4 Trifluoperazine 13
1.5 Melatonin and its Metabolites 14
1.6 Molecular Docking and Dynamics Simulations 20
1.7 Research Objectives 21
Chapter 2 Biophysical Characterization of AMK interactions with CaM and NOS peptides 23
2.1 Introduction 23
2.2 Methods and Experiments 24
2.2.1 Wildtype CaM Protein Expression 24
2.2.2 Purification of Wildtype CaM 25
2.2.3 NOS CaM-Binding Domain Peptides 25
2.2.4 Circular Dichroism Spectroscopy 26
2.2.5 Isothermal Titration Calorimetry 26
2.2.6 Gel Mobility Assays 27
2.2.7 Surface Plasmon Resonance 28
2.2.7.1 Sample Preparation for SPR 28
2.2.7.2 SPR Protocol 29
2.2.8 Enzyme Kinetics Assays 30
2.2.8.1 Oxyhemoglobin Preparation 30
2.2.8.2 Oxyhemoglobin Calibration 31
2.2.8.3 Oxyhemoglobin Capture Assay 32
2.3 Results and Discussion 35
2.3.1 Circular Dichroism Spectroscopy 35

2.3.2 Isothermal Titration Calorimetry....43
2.3.3 Gel Mobility Assays....48
2.3.4 Enzyme Kinetics and SPR Studies....50
2.4 Conclusions....56
Chapter 3 Chemical Shift Perturbation and Solution Structures of the CaM-AMK Complex....58
3.1 Introduction....58
3.2 Methods and Experiments....59
3.2.1 Expression and Purification of Isotopically labelled CaM....59
3.2.2 NMR Spectroscopy Data Acquisition and Analysis....59
3.2.3 ^{15}N-HSQC NMR Titration....60
3.2.4 Structure Calculations of the CaM-AMK Complex....60
3.3 Results and Discussion....61
3.3.1 3D CaM-AMK Complex Structure Calculations.....61
3.4 Conclusions....70
Chapter 4 Molecular Dynamics Simulations of AMK-CaM-nNOS Interactions....72
4.1 Introduction....72
4.2 Methods and Experiments....73
4.2.1 Molecular Docking Simulations....73
4.3 Results and Discussion....74
4.3.1 Molecular Docking Simulations....74
4.3.1.1 CaM-AMK Docking Simulations....74
4.3.1.2 AMK-nNOS Docking Simulations....76
4.3.1.3 AMK-CaM-nNOS Docking Simulations....78
4.3.2 Molecular Dynamics Simulations....79
4.3.2.1 Molecular Dynamics Simulations of CaM-AMK Complexation....79
4.3.2.2 Molecular Dynamics Simulations of AMK-nNOS Peptide Complexation....86
4.3.3.3 Molecular Dynamics Simulations of AMK-CaM-nNOS Peptide Complexation .87
4.4 Conclusions....89
Chapter 5....91
Summary and Future Work....91
5.1 Summary....91
5.2 Recommendations for Future Work....93
5.2.1 Binding Analysis under Physiological Ca^{2+} Concentrations.....93
5.2.2 Recreation of Previously Conducted Biophysical Analyses....94
5.2.3 Solution Structure of CaM-AMK in complex with nNOS.....94
Appendix A Calmodulin Expression Information....95
Appendix B NMR Pulse Program Information....96
Appendix C CaM-AMK Assigned Chemical Shifts....98

Bibliography 103

List of Figures

Figure 1.1 EF hand structure and Ca^{2+} coordination. 2
Figure 1.2 Structures of CaM and the eNOS CaM-binding region in complex with holo-CaM.4
Figure 1.3 Reaction scheme of NOS-catalyzed conversion of L-arginine to L-citrulline and •NO7
Figure 1.4 Domain structure of NOS isozymes. 8
Figure 1.5 Structures of domains NOS aligned by amino acid sequence. 9
Figure 1.6 Structure of TFP and the Holo-CaM-TFP complex. 13
Figure 1.7 Structures of aMT, AFMK and AMK. 15
Figure 1.8 Molecular mechanics of the CHARMM forcefield. 20
Figure 2.1 Sequence of CaM-binding domains of NOS isoforms. 25
Figure 2.2 Far-UV CD CaM-antagonist titrations. 37
Figure 2.3 Far-UV CD CaM-antagonist titration curves. 38
Figure 2.4 Changes in α-helical content predicted by BestSel. 39
Figure 2.5 Antagonist-induced changes in subtractive Far-UV CD analyses of CaM and peptide-bound CaM. 41
Figure 2.6 Results from CaM-AMK ITC experiments. 43
Figure 2.7 Representative curves of CaM, nNOS and eNOS peptides with and without AMK ...45
Figure 2.8 Results from AMK-nNOS and AMK-eNOS ITC experiments. 46
Figure 2.9 Representative ITC results from CaM and rNSCaTE peptides with and without AMK. 47
Figure 2.10 4 M Urea-PAGE gel at with 1000-fold excess antagonist concentrations. 48
Figure 2.11 Oxyhemoglobin capture assays. 52
Figure 2.12 ITC competition assays with nNOS and eNOS peptides. 55
Figure 3.1 Composite figure of NMR structural data. 62
Figure 3.2 Structures of CaM when in complex with AMK. 64
Figure 3.3 ^{15}N-HSQC titration spectral overlay and chemical shift changes. 66
Figure 3.4 ^{15}N-HSQC titration curves of residues with largest chemical shift changes. 67
Figure 3.5 Impact of AMK on the CaM-nNOS ^{15}N-HSQC spectrum. 70
Figure 4.1 20 highest affinity docking poses of AMK bound to CaM generated by AutoDock Vina. 75
Figure 4.2 Hydrophobicity surface mapping of CaM near predicted AMK binding sites. 76
Figure 4.3 20 highest affinity docking poses of AMK bound to the nNOS peptide generated by AutoDock Vina. 77

Figure 4.4 20 Highest affinity docking poses of AMK bound to the CaM-nNOS peptide complex generated by Autodock Vina. 78
Figure 4.5 RMSD of CaM-AMK MD simulations and geometrical parameterization of trajectories. 79
Figure 4.6 Model 1 minimization and equilibrium MD trajectory. 80
Figure 4.7 Model 1 production MD trajectory. 81
Figure 4.8 Model 1 protein-ligand contact analysis for CaM and AMK during the production MD simulation. 82
Figure 4.9 Heat map of AMK localization in the N-terminal domain over the course of minimization and production MD simulations 83
Figure 4.10 Model 5 and model 9 MD production trajectories. 85
Figure 4.11 Visual CaM-nNOS MD trajectory. 86
Figure 4.12 RMSD of AMK-CaM-nNOS minimization MD simulation 87
Figure 4.13 Visual AMK-CaM-nNOS minimization MD trajectory 88
Figure 4.14 Proximal residues of AMK during the production MD simulations 89

List of Tables

Table 1.1 Overview of some CaM-target proteins 5
Table 2.1 Substrate solution of enzyme-initiated assays 32
Table 2.2 Enzyme solution of enzyme-initiated assays 32
Table 2.3 Substrate solution of substrate-initiated assays 33
Table 2.4 Enzyme solution of substrate-initiated assays. 34
Table 2.5 Comparison of experimentally determined binding parameters from SPR 54
Table 3.1 Estimation of N-terminal domain K_d from ^{1}H and ^{15}N chemical shifts 68
Table 3.2 Estimation of C-terminal domain K_d from ^{1}H and ^{15}N chemical shifts 69
Table 4.1 Scoring for 20 highest affinity AutoDock Vina-generated CaM-AMK models. 75
Table 4.2 Distribution of 20 highest affinity models from AutoDock Vina across 6 identified docking sites. 76
Table 4.3 Scoring for 20 highest affinity AutoDock Vina-generated nNOS-AMK models. 77
Table 4.4 Scoring for 20 highest affinity AutoDock Vina-generated AMK-CAM-nNOS models. 78

List of Abbreviations

AFMK	N1-Acetyl-N2-formyl-5-methoxykynuramine
AMK	N1-Acetyl-5-methoxykynuramine
aMT	Melatonin
Ca^{2+}	Calcium
CaM	Calmodulin
cAMP	Cyclic adenosine monophosphate
CARA	Computer Aided Resonance Assignment
CD	Circular dichroism
cNOS	Constitutive nitric oxide synthase
CNS	Central nervous system
DTT	Dithiothreitol
eNOS	Endothelial nitric oxide synthase
FAD	Flavin adenine dinucleotide
FMN	Flavin mononucleotide
H_4B	Tetrahydrobiopterin
HSQC	Heteronuclear single quantum correlation
IET	Interdomain electron transfer
iNOS	Inducible nitric oxide synthase
LTP	Long-term potentiation
MD	Molecular dynamics
MLC	Myosin light chain
MLCK	Myosin light chain kinase
NAMD	Nanoscale Molecular Dynamics
NMDA	N-methyl-D-aspartate
NMR	Nuclear magnetic resonance
nNOS	Neuronal nitric oxide synthase
•NO	Nitric oxide
NOE	Nuclear Overhauser enhancement
NOESY	Nuclear Overhauser Effect SpectroscopY
NOHA	N-hydroxy-L-arginine
NOS	Nitric Oxide Synthase
ONOO-	Peroxynitrite
ONOOH	Peroxynitrous acid
PSF	Protein structure file
RNS	Reactive nitrogen species
ROS	Reactive oxygen species
SCN	Suprachiasmatic nucleus
SPR	Surface plasmon resonance
TFP	Trifluoperazine
TOCSY	TOtal Correlation SpectroscopY

Chapter 1
Literature Review

1.1 Calcium Signalling Pathway

Calcium (Ca^{2+}) is an ion used in cellular signalling, exerting allosteric regulation on numerous enzymes and proteins. Intracellular Ca^{2+} regulation is involved in processes such as muscle contraction, neuronal transmission, fertilization, cell motility and growth, neurogenesis and synaptic plasticity.[1,2] Basal concentration ranges from 50-100 nM, and increases by up to 100 fold during certain cellular functions.[3] These processes are facilitated by Ca^{2+}-sensing proteins, which often contain a structural element known as an EF hand. An EF hand is a helix-loop-helix structural motif in which Ca^{2+} is coordinated by ligands in the loop domain (Figure 1.1A). The presence of oxygen is critical to protein binding to Ca^{2+} within these domains, as negatively charged oxygen from glutamate and aspartate sidechains have high affinity for Ca^{2+}.[4] EF hands are typically found in pairs with adjacent loop domains associating through antiparallel β-sheet hydrogen bonds. The amphipathic helices conform with hydrophobic regions being packed inwards into a tight core, consolidated by inter- and intrahelical hydrophobic interactions. Conversely, the outward facing solvent-exposed regions contain charged residues that interact with ions and solvent through favourable electrostatic interactions.[5] One prominent Ca^{2+}-binding protein is Calmodulin (CaM), whose EF hand loop domains are 12 amino acids in length and rich in aspartate residues, which are important in the pentagonal bipyramidal coordination of Ca^{2+} *via* 7 oxygen containing-ligands in residues 1-3-5-7-9-12 (Figure 1.1B). The coil structure is found from residues 1-6, followed by a β-strand from 7-9 and an α-helix from 10-12.[4]

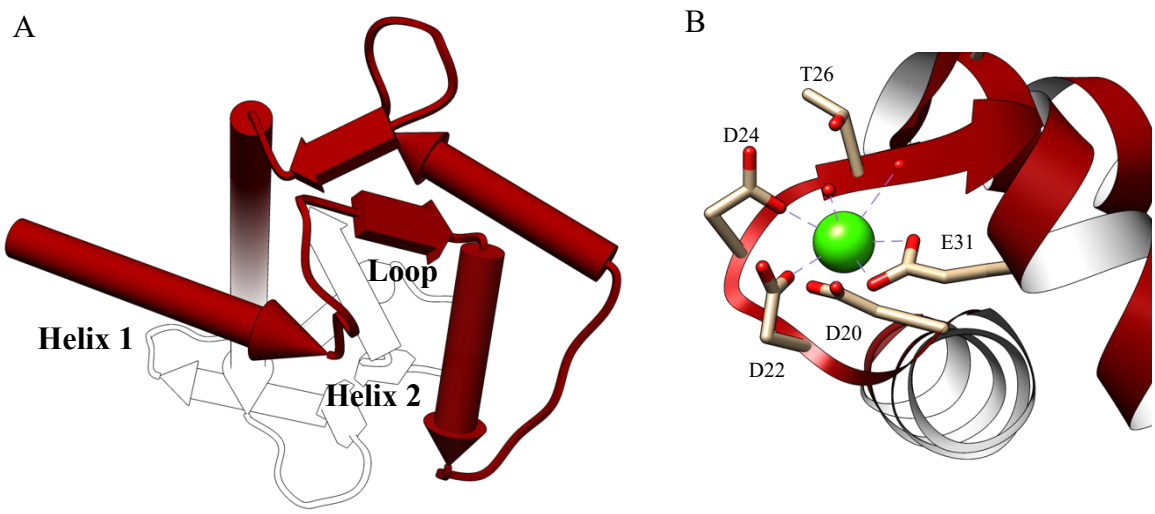

Figure 1.1 EF hand structure and Ca^{2+} coordination.
(A) The helix-loop-helix structural motif of the first EF hand in CaM. (B) The coordination of Ca^{2+} in the first EF hand. Dark red corresponds to CaM, green to Ca^{2+}, beige to amino acid sidechains and bright red to oxygen. Contacts are represented by a purple dashed line. Structures were generated in USCF Chimera v. 1.13.1. from PDB 3CLN.

1.2 Calmodulin Overview

CaM is a homologous, multifunctional messenger protein consisting of 148 amino acids and weighing 16700 Da. It is targeted and successively activated by Ca^{2+}, whereupon CaM coordinates Ca^{2+} signal transduction cascades through interactions with various target proteins and enzymes.[6,7] Many of these target proteins cannot bind to Ca^{2+} independently and thus require CaM for activation. CaM is always expressed intracellularly but is also expressed in a range of cell types and organelles. It has been found in all eukaryotic organisms and is involved in numerous cellular processes including division, fertilization, secretion, contraction and motility and neurotransmission.[8]

The ubiquity of CaM implicates it in mediating many crucial physiological functions including facilitating smooth muscle contraction. This is accomplished by initiating cross-bridge cyclic phosphorylation of the myosin light chain (MLC).[9] The enzyme responsible for

phosphorylation, MLC kinase, is Ca^{2+}-dependent and is activated by the binding of CaM.[10] CaM has also been shown play a role in memory and long-term potentiation (LTP). Ca^{2+}/CaM-dependent protein kinase II (CaMKII) is central to Ca^{2+} and cyclic adenosine monophosphate (cAMP) signalling for long-term memory formation.[11,12] CaM is also involved in metabolism *via* the activation of phosphorylase kinase and through actuating calcitonin. Calcitonin regulates blood Ca^{2+} levels as well as G protein-induced cAMP production and CaM inhibition has been found to decrease these regulatory effects.[13]

1.2.1 CaM Structure

CaM is a small, highly acidic protein possessing N- and C-terminal globular domains that share 75% sequence homology, connected by a central flexible linker region. The N-terminal domain is located from residues 1-75, the linker region from 76-81, and the C-terminal domain from 82-148. Both domains contain two EF hand motifs that each bind to a single Ca^{2+} ion, meaning that CaM has the ability to bind up to four Ca^{2+} ions in total.[14] The Ca^{2+}-binding loop segments of the EF hands are located in amino acid residues 21-31, 57-68, 94-105 and 130-141 in CaM. Constitutive differences between domains confer each with distinct electrostatic potential surfaces, resulting in asymmetric Ca^{2+} affinity. The more rigid C-terminal EF hands have a 10-fold higher affinity ($K_d = 10^{-6}$ M) in comparison to EF hands localized to the more flexible N-terminal ($K_d = 10^{-5}$ M).[14] Ca^{2+} binds sequentially to EF hands III, IV, I and II and dissociates in reverse order.[15] Ca^{2+}-CaM complexes exist primarily in one of two states: Ca^{2+}-deplete apo-CaM (Figure 1.2A) and fully Ca^{2+}-replete holo-CaM (Figure 1.2B).

Ca^{2+} binding to CaM induces several conformational changes in helix packing that promote binding to target proteins. Apo-CaM adopts a shorter, more compact structure with α-

helices of the two proximal EF hands aligning in an antiparallel fashion with interhelical angles of 128°-137°. Conversely, in holo-CaM the EF-hand helices open with interhelical angles in a near perpendicular orientation (86°-101°). This change permits negatively charged sidechains to coordinate the Ca^{2+} ion, exposing hydrophobic cavities in each domain involved in protein recognition that are closed in apo-CaM.[16] These exposed hydrophobic regions are rich in methionine residues, with 4 per domain and 1 in the central linker region. The 9 methionine residues constitute 46% of the hydrophobic surface area within the cavities and are considered to be responsible for target recognition due to the flexible sidechains and polarizable sulphur atoms.[17] In contrast, apo-CaM surfaces are predominantly hydrophilic, lacking the exposed hydrophobic domains necessary to capture the aliphatic and aromatic sidechains of the target binding proteins.[16] Although more compact, apo-CaM is more dynamic, with Ca^{2+}-binding significantly reducing flexibility.

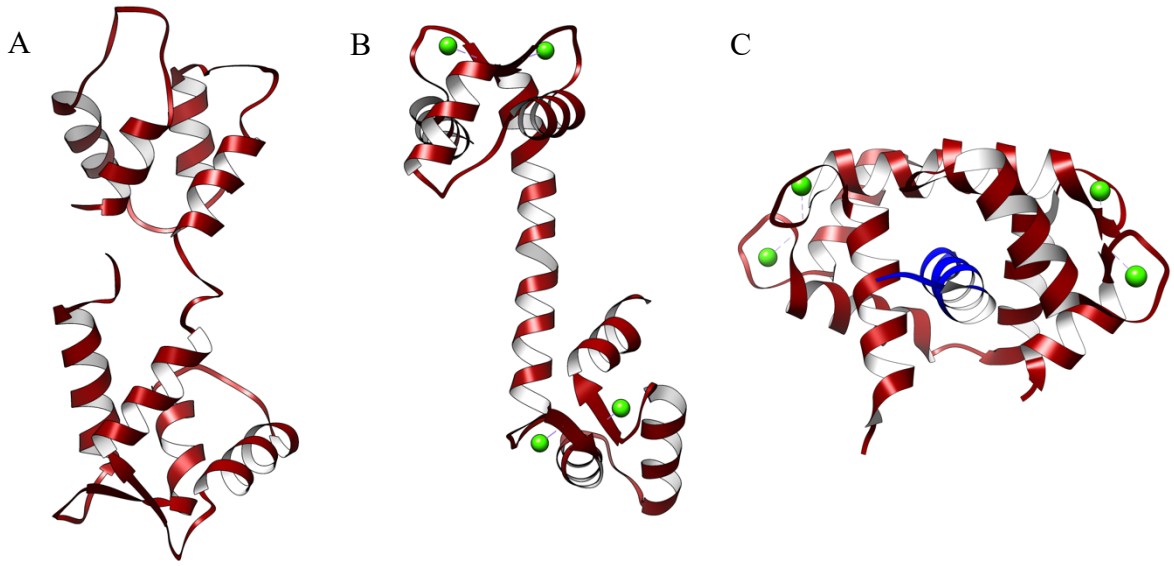

Figure 1.2 Structures of CaM and the eNOS CaM-binding region in complex with holo-CaM.
The crystal structure of (A) apo-CaM, (B) holo-CaM and (C) holo-CaM in complex with the eNOS CaM-binding domain. CaM is shown in red, the CaM binding peptide is shown in blue and Ca^{2+} is depicted as a green sphere. Models were derived from PBD 1CFD, 1CLN, and 2LL7 respectively and visualized using USCF Chimera v. 1.13.1.

1.2.2 CaM Binding to Target Proteins

CaM is able to bind to basic, amphiphilic α-helices within a large number of target proteins. This promiscuity does not translate to non-specific interaction, as the flexible central linker region between the two globular domains allows CaM to adopt a wide variety of conformations and bind with high affinity and selectivity.[18] This process generally involves wrapping the N- and C- terminal domains around the target protein (Figure 1.2C). The alignment of the CaM C-terminal towards the C-terminal of the protein (same with respect to N-terminals) is categorized as a parallel conformation; antiparallel consists of the N- and C-terminals of CaM and the protein aligning.[19]

Table 1.1 Overview of some CaM-target proteins

Group	*Target enzyme of protein*	*Number of Ca^{2+}*
		CaM Binding with Canonical Binding mode
Protein Kinases	CaM-dependent protein kinase I (CAMKI)	4
	CaM-dependent protein kinase II (CAMKII)	4
	Myosin light chain kinase (MLCK)	4
	Death-associated protein kinase (DAPK)	4
Phosphatases	Calcineurin	4
Secondary Messengers	Nitric Oxide Synthase (NOS)	4
	Inducible NOS	0
	Plasma-membrane Ca^{2+}-ATPases (PMCA)	4
	Voltage-dependent Ca^{2+} channels (CaV1.1)	4
	Voltage-dependent Ca^{2+} channels (CaV1.1)	4
	Ryanodine receptor RYR1	4
	Type I adenylate cyclase	4
Cytoskeletal and	Neuromodulin	0
Membrane Proteins	PEP-19	0
		CaM Binding in Elongated Binding Mode
Ion Channels	Bacillus anthracis edema factor (EF)	2
	Small-conductance Ca^{2+}-activated K^{+} channels (SK2)	2
	Voltage-gated sodium channels ($Na_V1.5$)	4
	$Na_V1.5$	0

Target proteins that bind to CaM generally possess a binding domain of approximately 20 amino acids. Some examples of well characterized CaM binding proteins from other studies are shown in Table 1.1.[20–22] Apo-CaM primarily adopts the consensus IQ binding motif with the general form IQXXXRGXXXR, where X represents any amino acid. Holo-CaM binding

domains predominantly follows a 1-5-10 or 1-5-8-14 motif, each named after positions of conserved residues within their respective motifs with the outer numbers denoting anchoring residues. These anchoring residues bind to hydrophobic patches containing methionine sidechains in the terminal domains of CaM, facilitating interactions between the linker region and the basic residues in between the anchors.[23] Binding orientation is mediated by the glutamic acid residues forming rings around these methionine pockets. Specificity is further achieved through the formation of hydrogen bonds and salt bridges between polar sidechains in the central linker and the binding domain, as well as between the N- and C-terminal domains of CaM and basic residues in the target sequence.[18,24] These residues are abundant in nitric oxide synthase (NOS) isozymes; the CaM-binding domain of neuronal NOS (nNOS) is highly basic and has only one acidic residue.[25] Due to this basicity, nNOS is able to interact electrostatically with glutamate residues in both domains of CaM.[24] Interactions between CaM and NOS have been widely studied, as mammalian NOS isoforms are involved in numerous essential biological functions.

1.3 Nitric Oxide Synthase

NOS is a catalytic enzyme responsible for the conversion of L-arginine to L-citrulline and nitric oxide (•NO) *via* a series of mono-oxygenase reactions. NOS uses nicotinamide-adenine-dinucleotide phosphate (NADPH) as a co-substrate, donating hydride ions in the presence of molecular oxygen. Flavin adenine dinucleotide (FAD), flavin mononucleotide (FMN) and tetrahydrobiopterin (H_4B) serve as cofactors.[26,27]

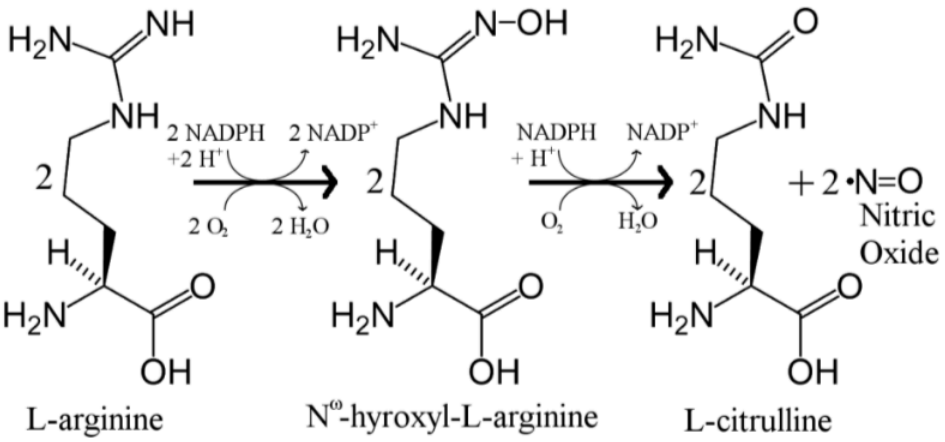

Figure 1.3 Reaction scheme of NOS-catalyzed conversion of L-arginine to L-citrulline and •NO

1.3.1 NOS Isoforms

•NO synthesis has been observed in most organisms, ranging from animal cells to fungi, bacteria and plants. Mammalian NOS is present *in vivo* in three isoforms: neuronal NOS (nNOS, NOS I), inducible NOS (iNOS, NOS II) and endothelial NOS (eNOS, NOS III). iNOS is expressed transiently, whereas eNOS and nNOS are expressed constitutively, and are therefore collectively known as constitutive NOS (cNOS). All isoforms require CaM binding for enzymatic activity; cNOS is Ca^{2+} dependent whereas iNOS is regulated at the transcriptional level and is Ca^{2+} independent. Additionally, cNOS activation is contingent on the binding of both N- and C-lobes of CaM, where iNOS only requires the N-lobe.[28] These isoforms have a 51-57% sequence homology and vary in size with eNOS, nNOS and iNOS having molecular weights of 133, 165 and 130 kDa, respectively [27,29] The expression of nNOS is primarily localized in central and peripheral neuronal tissue. It functions as a retrograde neurotransmitter and regulates synaptic plasticity in the central nervous system (CNS).[30] iNOS synthesizes large quantities of •NO in a variety of cell types as an immune response to cytokines and has a cytostatic effect on invasive parasites, tumours and bacterial growth.[31] eNOS is localized predominantly to

endothelial cells. It is involved in several vascular functions including insulin secretion, angiogenesis and regulation of vascular tone.[32] All NOS isoforms possess a bidomain structure, consisting of an N-terminal oxygenase domain and a C-terminal reductase domain. Within the oxygenase domain are binding sites for H_4B, heme, L-arginine and molecular oxygen.[27] The reductase domain is connected to the oxygenase domain by a central CaM-binding region and contains binding sites for FAD, FMN and NADPH (Figure 1.4).[27]

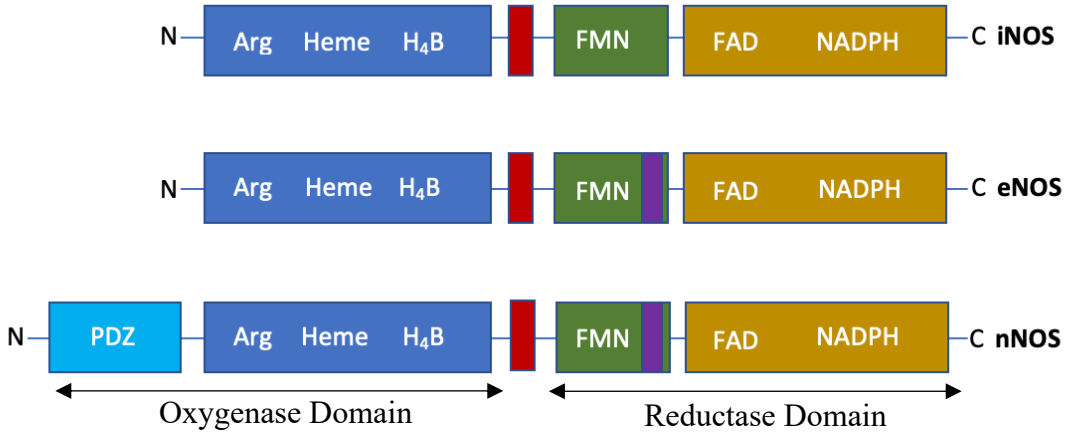

Figure 1.4 Domain structure of NOS isozymes.
The oxygenase domain is shown in blue with the nNOS PDZ domain shown in light blue. The reductase domain is displayed with the FMN and FAD/NADPH subdomains shown in green and yellow respectively. The autoinhibitory regions of eNOS and nNOS are shown in purple. The oxygenase domain and reductase domains are separated by a CaM-binding region shown in red.

The NOS catalytic mechanism is predicated upon the concept of interdomain electron transfer (IET), wherein electrons pass from NADPH to FAD, then FMN and finally to the heme complex. CaM is necessary for this process, acting as a molecular switch to fully activate the enzyme upon binding. The CaM-binding domain sequence of human NOS consists of residues 731-752 for nNOS, 501-531 for iNOS, and 491-512 for eNOS.[33,34] Both nNOS and eNOS follow the characteristic holo-CaM-peptide 1-5-8-14 binding motif, however iNOS does not follow consensus apo-CaM IQ binding. Instead, iNOS also contains the 1-5-8-14 binding motif and

therefore binds in the characteristic antiparallel orientation similar to cNOS isozymes.[35] Although the precise dynamics of CaM-mediated activation are not understood, it is known that CaM binding induces a conformational change that enables the flow of electrons between domains. NADPH, isozyme-specific residue Arg_{1400} and the C-terminal tail collectively repress enzyme activity by locking the FMN domain in place in an electron-accepting position. CaM binding propagates a large-scale swinging motion of the FMN domain in order to deliver electrons to the catalytic module.[36] Following this, electrons flow from the FMN domain to the ferrous heme and reduce the molecular oxygen present, as shown in Figure 1.5.[37] The reduced oxygen then cleaves the bond between guanadino-nitrogens and neighbouring protons and binds to these nitrogen atoms along with a proton on the L-arginine residue, producing the reaction

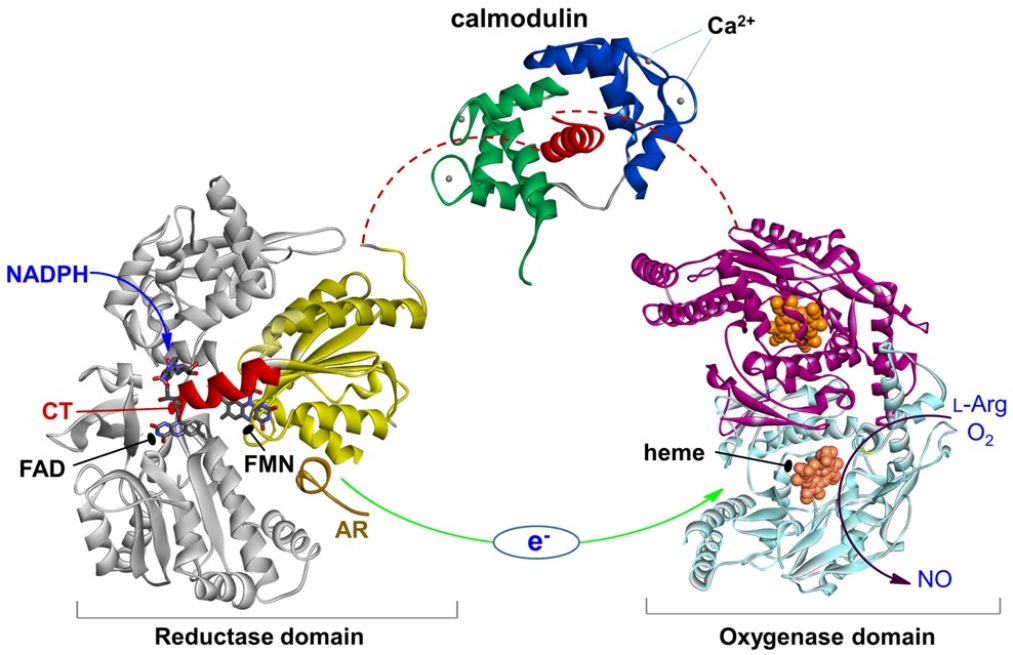

Figure 1.5 Structures of domains NOS aligned by amino acid sequence.
NOS domains with the FMN subdomain shown in yellow and the rest in grey, an α-helical CaM-binding region with bound CaM and a dimeric heme domain. Electron transfer is represented by a green arrow. Reprinted from Li, J.; Zheng, H.; Feng, C. Deciphering Mechanism of Conformationally Controlled Electron Transfer in Nitric Oxide Synthases. *Front. Biosci. - Landmark* **2018**, with permission for educational use from Frontiers in Bioscience.[37]

intermediate N-hydroxy-L-arginine (NOHA).[38] In the second step of the reaction, NOHA is converted to L-citrulline and •NO *via* a similar reaction, where reduced oxygen cleaves the bond between •NO and its neighbouring carbon and proton atoms.[39]

NOS is a homodimeric protein and requires dimerization into an active state, which involves interfacing large sections of the respective oxygenase domains. This interface includes the H_4B and L-arginine binding sites, a β-hairpin hook (N-terminal hook) as well as a structural zinc ion.[27,40] This segment constitutes approximately 50 residues and is thought to stabilize inter- and intradimer H_4B binding. Cysteine residues (two per monomer) are involved in coordinating H_4B affinity, either through forming intermonomer disulphide bridges or ligating the tetrahedral zinc site between monomers.[27] The N-terminal hook swaps recurrently between the two monomers, further stabilizing the formation of the dimer. This general description of active state dimerization of NOS is widely accepted, although the process varies slightly by isoform. Yeast two-hybrid studies have indicated that iNOS involves only oxygenase domain interactions whereas constitutive forms of NOS appear to interact at the reductase domain as well *via* interfacial salt bridges and hydrogen bonds.[27,41,42]

Despite the utility of •NO produced from the various NOS catalytic pathways, excess •NO production has numerous physiological consequences. The study of the overexpression of nNOS is of particular clinical importance as it has been implicated in the pathogenesis of a variety of neurodegenerative conditions.

1.3.2 Validation of nNOS as a Drug Target

Neurodegeneration is a broad term that refers to a loss of neuronal structure and function, characterizing many disorders including Alzheimer's, Parkinson's, epilepsy and

ischemic/traumatic brain injury among others.[43] The loss of neuronal function cannot be attributed to a solitary pathway, and instead is the product of a complex cascade of biomolecular processes. One area of interest under investigation for the development of therapeutic intervention is the regulation of •NO levels in the brain. Acting as a secondary messenger, •NO operates through the cyclic-3', 5'-monophosphate pathway and, in nanomolar concentrations, has been found to have neuroprotective properties. •NO in nerve cells is produced as holo-CaM activates nNOS following stimulation of Ca^{2+}-permeable NMDA receptors.[43,44] At basal levels, •NO related processes are important for long-term potentiation, learning and memory but can become neurotoxic when the delicate equilibrium in the cell is destabilized. These destabilizing factors include infarction, inflammation and excess NMDA receptor activation, which cause concentrations of •NO to surge in the brain by several orders of magnitude.[45]

•NO can produce reactive nitrogen (RNS) and reactive oxygen (ROS) species such as peroxynitrite ($ONOO^-$) and peroxynitrous acid (ONOOH).[46,47] These free radicals can cause DNA damage, lipid peroxidation and protein structure damage through tyrosine nitration, excess S-nitrosylation and oxidation of cysteine residues.[43] These in turn can result in function-impairing protein misfolding and aggregation. Not only are the immediate effects of excess •NO problematic, but the physiological response *via* upregulation of various protective factors can be harmful as well. Subsequent depletion of glutathione stores and release of zinc from intracellular reserves can trigger apoptotic processes.[48] The increase in DNA-repair mechanisms and the corresponding rise in energetic demand can lead to cell death. Excess •NO can also interfere with the mitochondrial electron transport chain which results in the further release of superoxide from mitochondria.[43]

There is a growing body of evidence suggesting that the confluence of effects seen from excess •NO production is linked to a number of neurodegenerative conditions. In the brains of Alzheimer's patients, elevated •NO levels resulted in increased tyrosine nitration associated with protein damage and plaque build-up.[49] In Parkinson's mouse models, a ubiquitin ligase central to the survival of dopaminergic neurons is inactivated by •NO.[50] nNOS also been shown to cause PTZ kindling epilepsy-induced endoplasmic reticulum stress and oxidative damage and is thus a valuable target for the development of treatments for chronic epilepsy patients.[51] nNOS activation has also been shown to play a role in cell death in instances of ischemic brain injury.[52] There has been some research into the targeting and inhibition of nNOS for therapeutic uses. For example, nNOS-knockout mice models showed reduced neurological symptoms following induced ischemia. nNOS inhibitors have shown similar promise in models of Parkinson's. In baboons with induced loss of dopamine and neurological changes, the administration of an somewhat selective nNOS inhibitor blocked dopamine depletion and cognitive impairment.[53] A key criterion in the discovery of novel nNOS inhibitors is selectivity, as to minimize any potentially harmful nonspecific interactions. For example, the unwanted inhibition of eNOS has been correlated with congestive heart failure, cardiovascular dysfunction, myocardial fibrosis and should consequently be avoided.[54,55] Among the most effective approaches in the selective inhibition of nNOS is to attenuate IET in the isozyme through the use of CaM antagonists. One such antagonist that has proven very successful in the selective inhibition of nNOS is the compound trifluoperazine (TFP).

1.4 Trifluoperazine

TFP, shown in Figure 1.7A, is a phenothiazine derivative and is available commercially as a treatment for symptoms of schizophrenia. It has been well documented as a CaM antagonist and has been shown to block nNOS activity *in vitro* and *in vivo.*[56] In one such study, a number of

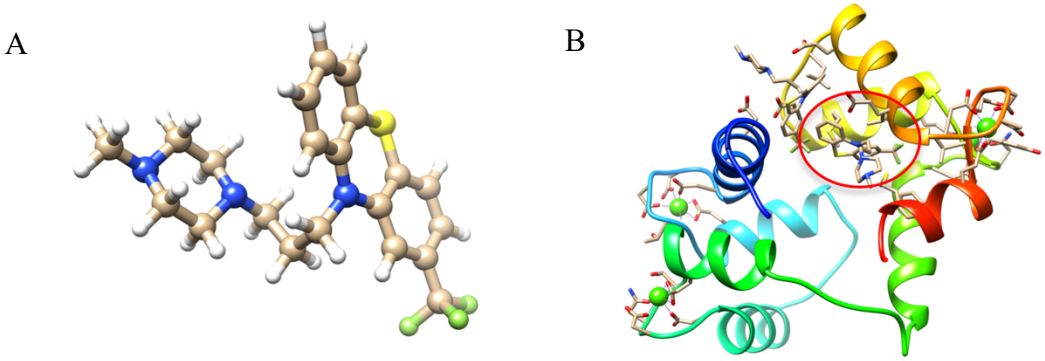

Figure 1.6 Structure of TFP and the Holo-CaM-TFP Complex.
(A) TFP structure (carbon in beige, hydrogen in white, nitrogen in blue, fluorine in green and sulphur in yellow). **(**B) Model of CaM bound to a single TFP molecule in the presence of Ca^{2+} (green spheres) showing interactions primarily with the C-lobe, derived from PBD 1CTR.

enzyme reactions were used to test the alteration of NOS sensitivity to CaM in pre-incubation preparation.[57] The conversion of L-arginine to L-citrulline seen *in vitro* was significantly reduced by the presence of the antagonist. TFP has been shown to enact its therapeutic effect by reducing formation of RNS/ROS species and decreasing 3-nitro tyrosine.[56] Binding conformation has been determined through various studies involving X-ray crystallography; TFP was shown to primarily interact with the C-terminal domain (Figure 1.7B).[58,59] Thirteen residues form 191 contacts between CaM and TFP, with only one of these residues (E11) being found on the N-terminal domain.[58] Stoichiometry of phenothiazine chemical class compounds including TFP ranges from 2-7 molecules per holo-CaM molecule, largely localized in or proximal to the hydrophobic regions of the globular domains.[59]

The potency of TFP makes it an effective inhibitor but bears with it the caveat of being rather cytotoxic. In addition to a long list of acute side effects, TFP has also been shown to inhibit DNA repair and increase instances of cell death of non-small cell lung carcinoma cells.[60]

1.5 Melatonin and its Metabolites

Over the past two decades, there has been increasing evidence indicating that melatonin (aMT, *N*-acetyl-5-methoxytryptamine) and one of its metabolites may have the capacity to inhibit nNOS activity through a similar mechanism to TFP. [61–63] aMT is a melanophore-contracting hormone synthesized by all vertebrates, produced primarily in the pineal gland but is also found in extrapineal locations such as the skin, gut, leukocytes and the Harderian gland. It is involved in numerous processes such as the entrainment of circadian rhythms, immune-stimulation and cytoprotection.[64,65] aMT is also present in fungi, protozoa, bacteria and invertebrates.[66]

aMT (Figure 1.6A) is an indoleamine with functional groups that confer specificity and amphiphilicity and is a derivative of tryptophan, biosynthesized *via* 5-hydroxylation, N-acetylation, decarboxylation and O-methylation. It is highly pleiotropic and targets the mammalian MT1 and MT2 G_i protein-coupled membrane receptors. There are considerable differences in location and density of these melatonin receptor subtypes, but both contribute to circadian feedback in the suprachiasmatic nucleus (SCN), or "circadian pacemaker".[67] MT1 receptors primarily modulate neuronal firing, vasoconstriction, and cancerous cell proliferation in addition to performing various metabolic functions. They are expressed in the pars tuberalis of the pituitary gland, the retina and the SCN. MT2 receptors are expressed in the retina and are

responsible for phase-shift of circadian rhythms, vasodilation and enhancing immune response.[68] Both receptors have been shown to have inhibitory effects on the cAMP pathway.[69]

Circulating hormonal aMT is predominantly catabolized by P_{450} monooxygenases to produce 6-hydroxymelatonin, which is then conjugated to form the 6-sulfatoxymelatonin metabolite. In tissue aMT, and in the central nervous system in particular, oxidative pyrole-ring cleavage results in the formation of alternate metabolites, namely N1-acetyl-N2-formyl-5-methoxykynuramine (AFMK, Figure 1.6B), which is deformylated to form N1-acetyl-5-methoxykynuramine (AMK, Figure 1.6C).[70]

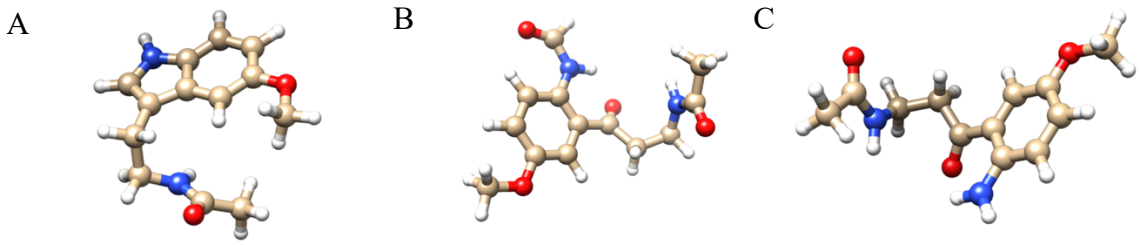

Figure 1.7 Structures of aMT, AFMK and AMK.
Molecular structure of (A) aMT and (B) AFMK and (C) AMK with white corresponding to hydrogen atoms, blue to nitrogen atoms, red to oxygen atoms and beige to carbon atoms. Models were derived from PubChem CID 896, 171161 and 390658 respectively and visualized using UCSF Chimera v. 1.13.1.

There have been many studies interrogating the interaction between CaM and aMT and its impact on nNOS enzyme activity. There appears to be a great amount of uncertainty as to the biological relevance of these interactions, primarily due to the disconnect between the very weak CaM-aMT binding observed experimentally and the significant inhibitory effects of aMT on nNOS seen *in vivo* and *in vitro*.

Interest in aMT as a CaM antagonist was possibly first generated by studies involving biological samples of CaM that reported very high-affinity binding (K_d = 0.2 – 1 nM).[71,72]

Subsequent analyses involving purified CaM samples suggested that binding is much weaker. In one such study, ^{15}N-HSQC nuclear magnetic resonance (NMR) spectroscopy titrations showed only minor perturbation of chemical shifts in CaM, consistent with a K_d value in the millimolar range.[73] Fluorescence and far-UV circular dichroism experiments from the same group showed similarly weak behaviour, with no saturation of CaM achieved even at high concentrations of aMT.[73] A later study used ^{15}N-HSQC NMR titrations in addition to computational methods and arrived at the same conclusion.[74] Non-linear fitting curves from their NMR titrations showed comparable affinities between globular domains, with K_d values ranging from approximately 3-6 mM. Their molecular dynamics simulations revealed highly dynamic binding between CaM and aMT, with the ligand localized primarily within the hydrophobic cavity of the C-terminal domain. Various groups have used gel mobility assays to further analyze association, with changes in the electrophoretic mobility of CaM typically only occurring at high concentrations (1 mM) of aMT.[73,75] The cause of the discrepancy between the apparent affinities of biological and purified CaM samples remains unknown.

The understated nature of the CaM-aMT complex formation contrasts the significant inhibition of nNOS enzyme activity reported *in vivo* and *in vitro*. Pozo *et al*. observed the effect of aMT on nNOS activity by monitoring the conversion of L-arginine to L-citrulline in rat cerebellar homogenates.[75] The presence of 1 mM melatonin lowered Vmax values from 90.9 pmol/mg protein/min to 65.5 pmol/mg protein/min. Antagonism of holo-CaM was suggested by a reversal of inhibition by the presence of the Ca^{2+} chelator EGTA or the addition of exogenous CaM to the incubation medium. Leon *et al.* similarly used homogenates from rat striatum to analyze kinetics of enzyme-substrate reactions in the presence of aMT.[61] The ligand was shown to inhibit nNOS activity *via* non-competitive antagonism of CaM. Homogenates of rat striatum

were used to similar effect to analyze the effect of AMK on enzymatic activity.[62] It was found that AMK acts non-competitively as previously described in the case of aMT, but no inhibition was caused by AFMK.

Camacho *et al.* extended their research beyond naturally occurring metabolites and evaluated synthetic analogues of aMT based on the excitatory response of striatal neurons to sensorimotor cortex (SMCx) stimulation.[63] These analogues consisted of kynurenine, kynuramine and phenyl-pyrazole structures with a variety of substituted R-groups and comparative analyses between these compounds revealed trends in structure-dependent inhibitory response. Compounds, specifically kynurenines and kynuramines, in which the 2'-NH_2 group was eliminated or blocked with either benzyl or dimethyl groups were significantly less effective in attenuating nNOS, as the amide potentially acts as a stabilizing intramolecular hydrogen donor. Similarly, compounds lacking 5'-Ome or Cl groups showed diminished levels of inhibition, although the nature of the interaction (hydrophobic or electrostatic) is not known. This structure-related inhibition of nNOS shows promise for developing additional analogues possessing diverse structural elements to achieve greater degrees of specificity and can be compared for their potency relative to other known antagonists.

Developing a detailed structural understanding of how these prospective antagonists, and particularly AMK due to its higher purported capacity for inhibition, interact with CaM and nNOS is of significant value. This is especially true in the case of AMK, as there is little in the way of any structural information of how it interacts with CaM. To this end, there are many powerful techniques that may be useful such as NMR spectroscopy.

1.5 NMR Spectroscopy

NMR spectroscopy has been used to determine high-resolution 3D structures and monitor internal dynamics of a protein.[76,77] NMR produces structures comparable to X-ray crystallography, however it can determine structures of proteins and molecules that would be unable to crystallize due to intrinsic flexibility and mobility. NMR is not without its caveats, as protein samples for NMR require isotopic labelling, such as ^{15}N and ^{13}C, which are rather costly to synthesize. Furthermore, analysis of large protein structures by NMR is difficult due to chemical shift overlap and lower sensitivity.

In an NMR experiment, the protein sample is placed in a static magnetic field and irradiated using radiofrequency (RF) pulses, perturbing the nuclei of the sample, which in turn produces an electromagnetic signal with a frequency specific to the magnetic field of the nucleus. This signal is produced by a net voltage in a detection coil by precession of nuclear spins around the constant magnetic field, typically at the nuclei's intrinsic Larmour frequency. The first step in structure determination is the complete assignment of the ^{1}H spectrum of the given protein, followed by the assignment of nuclear Overhauser enhancement (NOE) interactions. The more NOE constraints, the higher the resolution of the 3D structure (James and Oppenheimer, 1994). This is due to dipolar coupling through space between nuclei, rather than spin-spin coupling through chemical bonds.

Despite the utility of NMR, limitations arise with larger proteins due to severe crowding and chemical shift degeneracy. This makes both sequential and long-range NOE assignment nearly impossible. Furthermore, there is a pronounced increase in rotational correlation time, which corresponds to longer relaxation times and an increase in line widths. All scalar correlation experiments are contingent on the line widths not being significantly greater than the

size of J-couplings, which makes the labelling of proton spin systems extremely difficult.[78] 3D NMR experiments have been able to assist in overcoming these issues, expanding 2D spectra into a 3rd dimension which can then resolve overlap through separation into distinct layers.

The 2D ^{15}N-heteronuclear single quantum coherence (^{15}N-HSQC) experiment is one of the most frequently employed protein NMR experiments. Each residue of a protein except proline has an amide proton attached to a nitrogen in the peptide bond (Figure 1.5B). HSQC correlates the nitrogen atom and the amide proton to yield a peak in the HSQC spectrum. The ^{15}N-HSQC cannot be used to assign specific residues on its own and therefore is used in conjunction with various 3D experiments. These experiments can collectively be used to assign ^{1}H, ^{13}C, and ^{15}N chemical shifts for the protein. The following step involves the spatial couplings between nuclei, determined using nuclear Overhauser effect spectroscopy (NOESY), which infers distance constraints. NOESY spectra show NOE cross peaks of proximal nuclei, usually within 5 Å in a folded protein structure.[76]

There is significant interest in understanding the structural basis for interactions between potential antagonists, CaM and NOS. Despite numerous studies suggesting isoform-dependent properties of AMK, there are no 3D structures of CaM-AMK or CaM-AMK-NOS complexes. It is possible that they attenuate NOS activity through unfavourable modifications of this complex by affecting key residues in the N- and C-terminal lobes of CaM. Although aMT and AMK possess the intrinsic hydrophobicity characteristics of known CaM antagonists such as TFP, it is unclear which structural elements form contacts with CaM and with which residues. Elucidating the specific nature of this interaction using NMR may, however, may prove difficult given the putative millimolar range dissociation constant (K_d) of aMT binding with CaM.[73,74] As such it is unclear whether NOE-based methods of structure determination are sensitive enough

for such a potentially weak system. Computational methods may be used to compliment NMR data in order to overcome this obstacle.

1.6 Molecular Docking and Dynamics Simulations

Protein-ligand interactions have been at the forefront of drug discovery and design as they are a prerequisite for biological regulation.[79,80] Molecular docking experiments have proven to be a simple and economic way of characterizing these interactions, predicting experimental binding modes and affinities of small molecules within the bounds of a particular receptor target.[79] The quality of the output relies on the optimization search method and the scoring functions by which generated poses are evaluated. These functions are diverse, including knowledge-based, empirical and force field-based algorithms.[81] Docking software frequently use a rigid docking model in addition to semi-flexible model with mobile sidechains. There are also docking models in which the receptor is assumed to be entirely flexible, although these are less well developed.[79,82] Molecular docking can operate independently as a less refined approach to exploring protein-ligand interactions, or serve as a necessary precursor for more advanced and comprehensive molecular dynamics (MD) simulations.

$$V = V_{bonded} + V_{nonbonded}$$

$$V_{bonded} = \sum_{bonds} K_b(b - b_0)^2 + \sum_{angles} K_\theta(\theta - \theta_0)^2 + \sum_{dihedrals} K\chi(1+\cos(n\chi - \delta))$$

$$V_{nonbonded} = \sum_{nonbonded\ pairs\ ij} (q_i q_j/\varepsilon r_{ij}) + \sum_{nonbonded\ pairs\ ij} \varepsilon_{ij}[(R_{min,\ ij}/r_{ij})^{12} - 2(R_{min,\ ij}/\ r_{ij})^6\ ]$$

Figure 1.8 Molecular mechanics of the CHARMM [78] forcefield.

Basic components of the CHARMM [78] forcefield where K_b, K_θ and K_χ are the bond, angle and torsional force constants. B, θ and χ are bond length, bond angle and dihedral angle. *n* is multiplicity and δ the phase of the torsional periodic function; r_{ij} is the distance between atoms *i* and *j*; q_i and q_j are the partial charges of atoms *i* and *j*; ε is the effective dielectric constant; ε_{ij} is the Lennard-Jones well depth and $R_{min,\ ij}$ is the distance between atoms at Lennard-Jones minimum.

Molecular dynamics is a computational method that simulates the motion of a molecular system over a function of time.[83] All atoms within the simulation box are computed by the integration of Newtonian equations of motion as described in the equation $d^2r_i(t)/dt^2 = F_i(t)/m_i$.[81] $F_i(t)$ is the force exerted on atom i at time t, $r_i(t)$ the vector position of the atom i at time t and m_i is the mass of the atom. There are many integration algorithms that derive classical mechanical equations by discrete-time numerical approximation. The most commonly applied force fields in MD simulations are CHARMM, GROMOS, OPLS and AMBER.[84–87] An example of the basic components of the CHARMM force field is seen in Figure 1.8.[81] The trajectories over a specified timescale can then be visualized and analyzed according to various user-specified parameters. The ensemble of molecular docking and dynamics simulations paired with experimental methods are capable of generating a comprehensive analysis of complex biomolecular systems.

1.7 Research Objectives

The purpose of this thesis was to elucidate the structural means by which AMK might antagonize CaM in the isoform specific inhibition of nNOS. This was accomplished by:

1. Using biophysical analyses to characterize the strength of interaction between CaM and AMK and test for AMK-mediated reduction in CaM's affinity to NOS isoforms.
2. Interpreting AMK-induced chemical shift perturbations of isotopically labelled CaM to reveal the structural trends involved in complexation and to quantitatively measure affinity.
3. Determining solution structures of CaM when bound to AMK to reveal conformational changes that may be responsible for inhibitory function.

4. Using computational methods to visualize the dynamic interplay between CaM and AMK and replicate complex CaM-AMK-NOS systems to observe competition on a nanosecond timescale.

Chapter 2
Biophysical Characterization of AMK interactions with CaM and NOS Peptides

2.1 Introduction

Several studies have suggested that aMT and one of its metabolites, AMK, act as CaM antagonists and selectively inhibit nNOS.[61–63] This would prove significant as these naturally occurring compounds would offer far less cytotoxic alternatives to compounds such as TFP. Despite the purported ability of AMK to inhibit nNOS *in vitro* and *in vivo*, there is minimal data available that provides a detailed characterization of its binding with CaM as to better understand its mechanism of action. There are, however, studies available that interrogate the interaction between CaM and aMT that can provide insight into how structurally similar compounds may behave. Interest in aMT as a CaM antagonist was perhaps initiated by a study that reported a site-specific K_d value to be approximately 188 pM, however these findings appear to be an anomaly.[71] In a 1998 study, aMT showed minimal perturbation of CaM's methionine crosspeaks in NMR studies.[73] Furthermore, circular dichroism results from the same paper showed no significant impact on secondary structure. Electrophoretic mobility of CaM in gel mobility assays was only altered by aMT at extremely high concentrations of the ligand. In a later study, fluorescence assays showed no saturable association, even at elevated concentrations of aMT.[74] This was reflected in ^{15}N-HSQC NMR titration data in which changes in chemical shifts occurred in fast exchange on the NMR timescale, consistent with rapid association and dissociation. Fitting curves from this titration produced using non-linear regression revealed a millimolar range affinity.

In the present study, the goal is to build upon previous research into aMT and AMK and develop a holistic array of biophysical analyses to further investigate their potential as therapeutic agents. A particular focus was given to AMK, which was determined experimentally to be more potent that aMT and other structurally similar kynurenines. [61–63] The strength of binding was qualitatively and quantitatively defined using gel mobility assays, isothermal titration calorimetry (ITC), surface plasmon resonance (SPR) and circular dichroism (CD). The latter also used to observe any aMT- or AMK-mediated changes in secondary or tertiary structure in CaM. Effects on nNOS enzymatic activity were measured *in vitro* using the oxyhemoglobin capture assay.

2.2 Methods and Experiments

2.2.1 Wildtype CaM Protein Expression

The pET9d vector was used to express wildtype rat CaM with restriction enzymes NcoI and BaMHI used to clone in the CaM sequence. pET9d was then transformed into competent BL21 de3 *E. coli* cells.

A starter culture containing a colony of transformed *E. coli*, 50 µL of kanamycin and 50 mL of lysogeny broth (LB) was incubated overnight. 10 mL of this solution was then added to 4 L flasks each containing 1 L LB. Following a period of incubation where a differential absorbance of 0.6-0.8 at 600 nm was achieved, the culture was induced with 1 mL of 0.5 M IPTG and incubated for 4 hours. The solution was then centrifuged at 5000 rpm at 4 °C for 5 minutes. The supernatant was removed, and the pellets were collected and stored at -80 °C.

2.2.2 Purification of Wildtype CaM

Cells were suspended in 4 volumes of 50 mM MOPS, 1 mM EDTA, 1 mM dithiothreitol (DTT), 100 mM KCl, pH 7.5 and then lysed with an Avestin EmulsiFlex-C5 homogenizer (Ottawa, ON). The resulting lysate was centrifuged at 48000 x g for 30 minutes at 4 °C and 5 mM $CaCl_2$ was then added. The supernatant was loaded onto a phenyl sepharose fast flow resin (GE Healthcare Bio-Sciences, Baie d'Urfe, PQ) and connected to the Äkta design system in a 1 cm x 10 cm column (GE Healthcare Bio-Sciences, Baie d'Urfe, PQ). This column was equilibrated with 50 mM Tris-HCl, 1 mM $CaCl_2$, pH 7.5. 5 volumes of this same buffer were then used to wash the resin, followed by 3 volumes of 50 mM Tris-HCL, 1 mM $CaCl_2$, 500 mM NaCl, pH 7.5. The final wash consisted of 3 volumes of 50 mM Tris-HCL, 1 mM $CaCl_2$, pH 7.5. CaM was eluted from the resin with 10 mM Tris-HCL, 10 mM EDTA, pH 7.5 and collected in 2 mL fractions, which were then scanned from 320 to 250 nm by a Varian Cary UV–visible Spectrophotometer (Varian, Mississauga, ON). The fractions of CaM ($\varepsilon = 3229\ M^{-1}\ L^{-1}$) that displayed the characteristic peaks at 277 nm (tyrosine residues) and 269, 265, 259 and 253 nm (phenylalanine residues) were collected into aliquots of 500 µL. Purity was verified using sodium dodecyl sulfate–polyacrylamide gel electrophoresis (SDS PAGE).

2.2.3 NOS CaM-Binding Domain Peptides

All experiments were conducted using the CaM-binding domain peptides of NOS (Figure 2.1). Bovine eNOS (RKKT FKEVA NAVKIS ASLM, residues 491- 510), rat nNOS (KRRAI GFKKL AEAVK FSAKL MGQAK RVC, residues 730–757) and human iNOS (RPKRR EIPLK VLVKA VLFAC MLMRK, residues 508–531) peptides were synthesized by SynPeP (SynPeP Corporation, Dublin, CA USA).

eNOS (human)	RKKTFKEVANAVKISASLM	491-510
nNOS) (human)	KRRAIGFKKLAEAVKFSAKLMGQAKRVC	730-757
iNOS (human)	RPKRREIPLKVLVKAVLFACMLMRK	508-531

Figure 2.1 Sequence of CaM-binding domains of NOS isoforms.
The CaM-binding domain sequences for bovine eNOS, rat nNOS and human iNOS are shown. Acidic and basic residues are shown in red and blue respectively.

2.2.4 Circular Dichroism Spectroscopy

All circular dichroism (CD) experiments were performed using a Jasco J-715 CD spectropolarimeter and analyzed using J-715 software (Jasco Inc., Easton, MD, USA) as previously described with some modifications.[88] Samples were measured in a 1 mm quartz cuvette (Hellma, Concord, ON) and kept at 25°C using a Peltier type constant-temperature cell holder (model PFD 3505, Jasco, Easton, MD). All samples were in a 20 mM TrisHCl 100 mM KCl buffer with 1 mM $CaCl_2$ and incubated for 20 minutes at room temperature before loading. Far-UV spectra were recorded over a 260-200 nm range with a CaM concentration of 12 µM. Near-UV spectra were recorded over a range of 300-250 nm range with a CaM concentration of 70 µM. All spectra were recorded with a 1.0 nm band width, 0.2 nm resolution, 100 mdeg sensitivity at a 0.125 s response and a rate of 100 nm/min with a total of 25 accumulations.

2.2.5 Isothermal Titration Calorimetry

All isothermal titration (ITC) recordings were performed on a Microcal ITC200 from Microcal (Northampton, MA) at 25°C, 750 rpm stir speed, and reference power set between 1 and 2 µcal/s. Experiments were conducted in 50 mM HEPES buffer pH 6.95, 150 mM KCl and 2 mM $CaCl_2$, in both the cell and syringe. Buffer into buffer, antagonist into buffer, peptide into

buffer and buffer into CaM controls showed relatively low, consistent heats of injection and no significant baseline decay or drift indicating adequately matched cell and syringe buffer conditions. For CaM-NOS peptide control experiments, 39 μL of each peptide was titrated into 202 μL of CaM at varying concentrations, generally ranging from 100 μM peptide into 10 μM CaM to 500 μM peptide into 50 μM CaM. For CaM-AMK ITC experiments, AMK in the syringe at concentrations up to 2 mM was titrated into the cell containing 10 μM CaM. Ideal starting conditions were determined empirically depending on anticipated strength of binding and signal intensity. Between 50-100 injections at 3-minute intervals were carried out for a typical experiment. For competition assays, CaM was incubated with a 100-fold excess of AMK for 20 minutes at room temperature prior to loading into the cell and NOS peptide was titrated as previously described. Differences between the isotherms with and without AMK present were used to indirectly measure K_d values of AMK-CaM complexation according to $K_B = ([K_A/K_{Aapp}]-1)(1/B_t)$. K_A and K_B represent the binding constants for the NOS peptide and AMK respectively, K_{Aapp} is the experimentally measured binding constant for NOS in the presence of a given AMK concentration, and B_t corresponds to AMK concentration. Data analysis was performed using Origin ITC200 Origin70 module with pre-loaded fitting equations for one- and two-site models. The one-set-of-sites model was found to be applicable to all experiments.

2.2.6 Gel Mobility Assays

The binding between CaM, NOS and antagonists were assayed by observing relative mobility shifts of CaM by urea polyacrylamide gel electrophoresis (urea PAGE) and native gels. Gels contained 15% acrylamide, 0.375 M Tris-HCl, 1 mM $CaCl_2$ and varying urea concentrations ranging from 0-8M. Gels were run under a constant voltage of 100V in an

electrophoresis buffer containing 25 mM Tris-HCl, 1 mM $CaCl_2$ and 192 mM glycine. Samples contained urea (with the concentration matching that of the gel), 100 mM Tris-HCl (pH 7.5), 1 mM $CaCl_2$ and 20 μM CaM in a 15 μL sample volume and were incubated for 1 hour following centrifugation followed by a half volume addition of 50% glycerol with bromophenol blue. 10 μL of each sample was added to each well of the gel. In CaM binding experiments, between 1-1000 equivalents of AMK, aMT and TFP were added to individual samples. In competition experiments, AMK, aMT and TFP were added to samples in addition to 20 μM of NOS peptide.

2.2.7 Surface Plasmon Resonance

All surface plasmon resonance (SPR) experiments were conducted by Victoria Robertson as part of her 4th year thesis project under the supervision of Dr. J.G. Guillemette.

2.2.7.1 Sample Preparation for SPR

1X phosphate buffered saline pH 7.4 with 0.05% tween (PBS-T) was acquired from Nicoyalife (Kitchener, ON). Cysteamine (Cys) was prepared for immobilization at a concentration of 100 mM in PBS-T. This was then used to make 5:1 Cys:NOS peptide for injection.

A working stock of 33.3 μM CaM was stored in PBS-T and 100 μM $CaCl_2$ (PBS-T-$CaCl_2$). CaM experiments without AMK were conducted using 1 mL of 333 nM CaM, prepared with 10 μL of 33.3 μM CaM and 990 μL PBS-T-$CaCl_2$. This solution was then diluted as needed with PBS-T-$CaCl_2$ to obtain 300 μL of each 25, 50, 100, 150, 200, 250, 333 nM CaM solutions. AMK was dissolved into PBS-T-$CaCl_2$ to make 200 μL of 20 mM solution. CaM with excess AMK solution was prepared with 10 μL of 33.3 μM CaM, varying volumes of 20 mM AMK

depending on desired antagonist concentration, and the solution was brought up to a final volume of 1 mL with PBS-T-$CaCl_2$. CaM was incubated with AMK at room temperature for a minimum of 20 minutes, then diluted as needed with PBS-T-$CaCl_2$ to obtain 300 µL of each 25, 50, 100, 150, 200, 250, 333 nM CaM solutions with excess AMK.

2.2.7.2 SPR Protocol

SPR experiments were conducted using and openSPR instrument (Nicoylife, Kitchener, ON) at 25 °C at a constant 50µL/min flow rate in a 100 µL injection loop. The NOS peptides capped with an N-terminal cysteine were bound to a gold nanoparticle sensor chip functionalized with an immobilized coating of Cys. Binding of CaM in the presence and absence of AMK was analyzed in a Ca^{2+}-saturating PBS-T-$CaCl_2$ buffer. CaM was injected over the Cys:NOS peptide at concentrations ranging from 25-333 nM for 2 minutes to allow association to occur. Following each CaM injection at a given concentration, PBS-T buffer with 100 mM EDTA was injected to completely dissociate CaM and regenerate the unbound NOS peptide. Analysis of the data was done with TraceDrawer software (Ridgeview Instruments). Kinetics parameters

250-300 µL of injection solution was prepared for an OpenSPR 100 µL injection loop. The SPR system was primed with PBS-T buffer, referenced and inserted onto a clean gold nanoparticle sensor chip. Experiments were conducted with PBS-T buffer at a flow rate of 150 µL/min for 10 minutes prior to injection with 80% IPA for 5 minutes. Two PBS-T buffer blanks were injected at 150 µL/min, followed by a change in flow rate to 50 µL/min for up to 3 injection until no signal (<0.01 nm) was observed. Cys (1 mM) was injected and the buffer was changed to PBS-T-$CaCl_2$ after a 5-minute period for equilibration. Buffer was injected 2-4 times

until no signal was observed. Analyte was then injected in decreasing concentrations separated by rinses consisting of PBS-T-$CaCl_2$, PBS-T-EDTA and then PBS-T-$CaCl_2$ again.

2.2.8 Enzyme Kinetics Assays

All enzyme kinetics experiments were conducted by Joe Bui as part of his 4th year thesis project under the supervision of Dr. J.G. Guillemette.

2.2.8.1 Oxyhemoglobin Preparation

A 15 mL falcon tube was filled with approximately 5mL of bovine hemoglobin (Hb) was dissolved in the minimal amount (~2.5 mL) of 50 mM TRIS-HCl, pH 7.5 at room temperature. 40 mg of sodium hydrosulphite (purged with N2 and desiccated) was added to the solution and inverted to mix the sample. This was followed by a colour change of dark brown to ruby red. PD-10 (GE Healthcare Bio-Sciences, Baie d'Urfe, PQ) columns were washed with 25 mL of Milli-Q water and then equilibrated with 25 mL 50 mM TRIS-HCl, pH 7.5 at room temperature. 1 mL of Hb solution was loaded onto each PD-10 column to remove the sodium hydrosulphite from solution. The ruby red oxyhemoglobin (oxyHb) was eluted last, with the last few drops visible in the column not being collected to avoid contamination with residual sodium hydrosulfite. Solutions containing 25 μL of concentration Hb solution and 975 μL of 50 mM TRIS-HCl, pH 7.5 at room temperature in 0.2 cm quartz cuvettes were scanned from 220 to 700 nm on a UV-Vis spectrometer, using 1 mL 50 mM TRIS-HCl, pH 7.5 as a blank. Finally, the Hb solutions were aliquoted in 200 μL portions into Eppendorf tubes, flash frozen using dry ice, and stored at -80 °C. The concentration of oxyHb was determined using the following equation: [HbO4] μM = (1.013 x A576 – 0.3269 x A630 – 0.7353 x A560) x 100 x dil. factor x 5, where

A_{560}, A_{576} and A_{630} correspond to absorbance values and 560, 576 and 630 nm respectively. The 5 is present on account of a 0.2 cm pathlength and the 100 is from a previously published equation based on known extinction coefficients of oxyHb.[89,90]

2.2.8.2 Oxyhemoglobin Calibration

The molar extinction coefficient for the conversion of oxyHb to metHb for the oxyHb capture assay was calculated according to a previously published method.[91] Potassium ferricyanide ($K_3[Fe(CN)_6]$) was used to oxidize oxyHb to metHb. 40 mg of $K_3[Fe(CN)_6]$ was dissolved in 10 mL of 50 mM Tris-HCL pH 7.5 at room temperature to produce a 12 mM stock, which was then diluted 10-fold with 50 mM Tris-HCl to produce a final stock concentration of 1.2 mM $K_3[Fe(CN)_6]$. The oxyHb solution was diluted to 40 μM in 50 mM Tris-HCl pH 7.5 at room temperature to produce the working oxyHb solution. The metHb working solution was prepared by diluting oxyHb to 40 μM in the presence of 0.12 mM $K_3[Fe(CN)_6]$. 200 μL of each working solution was then added to a 96 well microlitre plate, with oxyHb loaded into wells A1-3 and metHb into wells A4-6. 100 μL of 50 mM Tris-HCl pH 7.5 was added to columns 1-3 of rows B-H, and 100 μL of 50 mM Tris-HCl pH 7.5, 0.12 mM $K_3[Fe(CN)_6]$ was added to columns 4-6 of rows B-H. Triplicate serial dilutions where then performed using a multi-channel pipettor by transferring 100 μL of row A to row B, row B to row C and so on until row G, with the final 100 μL taken being discarded and Row H being used as a blank. The plate was read using a SpectraMax 384 Plus 96 well UV-vis spectrophotometer and SoftMax Pro software (Molecular Devices, Sunnyvale, CA) at 401 nm. The slopes of OD_{401} versus nM of Hb was calculated for metHb and oxyHb and used to determine the extinction coefficient

$\Delta\varepsilon_{nm\ (met\text{- to }0xyHb)}$ needed for the oxyHb capture assay. The value of the extinction coefficient ranged from 0.10 to 0.13 OD_{401} per nM.

2.2.8.3 Oxyhemoglobin Capture Assay

Initial rates of •NO production were measured using the spectrophotometric oxyhemoglobin capture assay following a similar method as one previously developed by Dr. Basil Perdicakis (PhD. 2003, University of Waterloo) and Dr. Heather Montgomery (PhD. 2003, University of Waterloo) based on previous methods.[91] The experiment was conducted through the analysis of a 96 well microlitre plate containing mixtures of two solutions: the enzyme and substrate solutions. The nNOS enzyme was previously made by Dr. Valentina Taiakina, a previous graduate student, *via* recombinant protein expression. The substrate solution contained glycerol, Tris-HCl pH 7.5, $CaCl_2$, superoxide dismutase (SOD), catalase, bovine serum albumin (BSA), NADPH, L-arginine, and oxyHb. The enzyme solutions contained the nNOS enzyme, FAD, FMN, H_4B, DTT, BSA, catalase, SOD, Tris-HCl pH 7.5, and glycerol**.** NADPH, H_4B and DTT were prepared fresh on the day of the assay, with H_4B being dissolved in 20 mM DTT to ensure it was properly reduced upon solvation. NADPH serves the purpose of reacting with residual L-arginine in the enzyme solution from the NOS dialysis buffer. Catalase and SOD are present to react with reactive oxygen species resulting from uncoupled electron transfer in NOS.[90] Glycerol and BSA maintain stability of the NOS enzyme during the assay.

Enzyme-initiated assays involved the transfer of a CaM-AMK mix into enzyme solution, which was then pipetted into the substrate solution. In a 96 well microlitre plate, 100 µL of the enzyme solution was incubated for 5 minutes at room temperature in columns 5-6 with 40 µL of solution containing either CaM alone or CaM pre-incubated with antagonist. When no CaM is

needed, the CaM was replaced by Tris-HCl pH 7.5. During these 5 minutes, 40 µL of substrate was added to columns 1-4. Following incubation, 60 µL of the enzyme-CaM mixture was transferred to the substrate solution, with column 5 being transferred to column 1-2 and column 6 to 3-4. In a typical experiment, each row of the plate corresponds to a different CaM concentration increasing from 0 to 30 nM at a given concentration of antagonist, with row H being reserved for a control in which enzyme activity is blocked partially or completely by EDTA or a potent inhibitor. The final reaction mixture contained 1 µM FAD, 1 µM FMN, 5 µM H_4B, 1 µM DTT, 450 µM NADPH, 0.2 mg/mL BSA, 50 U/mL catalase, 100 U/mL SOD, 30 nM nNOS, 5 µM oxyHb, 25 µM, L-arginine, 200 µM $CaCl_2$, 50 mM Tris-HCl pH 7.5 and 1% glycerol in addition to the CaM-antagonist mix.

Table 2.1 Substrate solution of enzyme-initiated assays

	Stock Concentration	*Mix Concentration*	*Volume of Stock for 1 Well (µL)*	*Final Concentration in Reaction Well*
*HbO_4^*	1314 µM	12.5 µM	0.381	5 µM
*L-Arginine^*	30000 µM	62.5 µM	0.0833	25 µM
*NADPH**	10000 µM	450 µM	1.8	450 µM
*BSA**	100 mg/mL	0.2 mg/mL	0.08	0.2 mg/mL
*Catalase**	89700 U/mL	50 U/mL	0.022	50 U/mL
*SOD**	3100 U/mL	100 U/mL	1.29	100 U/mL
*$CaCl_2$^*	20000 µM	500 µM	1	200 µM
Tris-HCl pH 7.5	50 mM	50 mM	33.3	50 mM
*Glycerol**	20%	1%	2	1%

^Dilution factor of 0.429 to account for dilution upon mixing with CaM solution and substrate solution.
*Dilution factor of 0.714, constituents are also found in the substrate solution thus dilution only occurs from adding the CaM-inhibitor mixture.

Table 2.2 Enzyme solution of enzyme-initiated assays

	Stock Concentration	*Mix Concentration*	*Volume of Stock for 1 Well (µL)*	*Final Concentration in Reaction Well*
*nNOS^*	1314 µM	0.070 µM	0.070	0.030 µM
*FAD^*	1507 µM	2.33 µM	0.155	1 µM
*FMN^*	1307 µM	2.33 µM	0.178	1 µM
*H_4B^*	6400 µM	11.66 µM	0.182	5 µM
*DTT^*	20000 µM	2.33 µM	0.0117	1 µM
*NADPH**	10000 µM	630.25 µM	6.30	450 µM
*BSA**	100 mg/mL	0.28 mg/mL	0.28	0.2 mg/mL
*Catalase**	89700 U/mL	70.03 U/mL	0.0781	50 µM
*SOD**	3100 U/mL	140.06 U/mL	4.52	100 U/mL
Tris-HCl pH 7.5	50 mM	50 mM	81.3	50 mM
Glycerol	20%	1.4%	7	1%

^Dilution factor of 0.429 to account for dilution upon mixing with CaM solution and substrate solution
*Dilution factor of 0.714, constituents are also found in the substrate solution thus dilution only occurs from adding the CaM-inhibitor mixture.

Substrate-initiated assays involved the transfer an nNOS-AMK mix into the enzyme solution, which was then transferred to the substrate solution containing CaM. In a 96 well plate, 40 µL of enzyme solution was incubated at room temperature in column 7 with an nNOS-AMK mixture for 10 minutes. For reactions with no AMK present, Tris-HCl pH 7.5 was used in place of the antagonist. During this incubation period, 210 µL from each substrate solutions containing varying CaM concentrations were aliquoted into column 5-6. Each row corresponded to a given CaM concentration, typically ranging from 0 to 30 nM. 20 µL of the enzyme solution was then pipetted into columns 1-4 and the reaction was initiated by transferring 80 µL of substrate from column 5 into columns 1-2, and 80 µL form column 6 to columns 3-4. The final reaction mixture contained 1 µM FAD, 1 µM FMN, 5 µM H_4B, 1 µM DTT, 450 µM NADPH, 0.2 mg/mL BSA, 50 U/mL catalase, 100 U/mL SOD, 30 nM nNOS, 5 µM oxyHb, 25 µM, L-arginine, 200 µM $CaCl_2$, 50 mM Tris-HCl pH 7.5 and 1% glycerol in addition to CaM and AMK at varying concentrations.

Table 2.1 Substrate solution of substrate-initiated assays

	Stock Concentration	*Mix Concentration*	*Volume of Stock for 1 Well (µL)*	*Final Concentration in Reaction Well*
*HbO_4^*	1314 µM	6.25 µM	1.00	5 µM
*L-Arginine^*	30000 µM	31.25 µM	0.219	25 µM
*NADPH**	10000 µM	450 µM	9.45	450 µM
*BSA**	100 mg/mL	0.2 mg/mL	0.42	0.2 mg/mL
*Catalase**	89700 U/mL	50 U/mL	0.117	50 U/mL
*SOD**	3100 U/mL	100 U/mL	6.77	100 U/mL
*$CaCl_2$^*	20000 µM	250 µM	2.625	200 µM
CaM	20000 µM	Variable	Variable	Variable
Tris-HCl pH 7.5	50 mM	50 mM	Fill to 210 µL total volume	50 mM
*Glycerol**	20%	1%	10.5	1%

^Dilution factor of 0.8 to account for dilution when added with the enzyme solution.
*No dilution as the same constituents are found in the enzyme solution.

Table 2.4 Enzyme solution of substrate-initiated assays.

	Stock Concentration	*Mix Concentration*	*Volume of Stock for 1 Well (μL)*	*Final Concentration in Reaction Well*
*nNOS^*	1314 μM	0.025 μM	0.00761	0.030 μM
*FAD^*	1507 μM	8.33 μM	0.222	1 μM
*FMN^*	1307 μM	8.33 μM	0.254	1 μM
*H_4B^*	6400 μM	41.66 μM	0.260	5 μM
*DTT^*	20000 μM	8.33 μM	0.0166	1 μM
*NADPH**	10000 μM	750 μM	3.00	450 μM
*BSA**	100 mg/mL	0.33 mg/mL	0.132	0.2 mg/mL
*Catalase**	89700 U/mL	83.33 U/mL	0.0372	50 μM
*SOD**	3100 U/mL	166.67 U/mL	2.16	100 U/mL
Tris-HCl pH 7.5	50 mM	50 mM	Fill to 40 μL total volume	50 mM
Glycerol	20%	1.67%	3.34	1%

^Dilution factor of 0.12 to account for dilution upon mixing with and substrate solution and nNOS-inhibitor mixture.
*Dilution factor of 0.6 to account for the dilution form the nNOS-inhibitor mixture.

After initiation, the plate was read at 25 °C in a SpectraMax 384 Plus 96 well UV-vis spectrophotometer using SoftMax Pro software (Molecular Devices, Sunnyvale, CA). The reactions were read at 401 nm at 7 second intervals for 5 minutes. Soft Max pro was used to convert absorbance rates to catalytic activity according to the equation Activity = v x 60 s • min^{-1} / $\Delta\varepsilon_{401\ nm\ (met\text{- to oxyHb})}$ / (well volume x [nNOS] in nM x nNOS molecular weight in g/mol x 1000 mg/g) where v represents of slope of the change in absorbance over time in seconds. Activity is expressed in nanomoles of •NO produced per minute per milligram of enzyme (nmol •NO min^{-1} mg^{-1}).

2.3 Results and Discussion

2.3.1 Circular Dichroism Spectroscopy

Circular Dichroism (CD) was used to observe changes in alpha-helical content (far-UV) and local environments surrounding aromatic residues (near-UV) in CaM when interacting with antagonists both in the presence and absence of NOS peptides. Spectra were fitted using BestSel CD analysis.[92,93] Secondary structural elements were derived from the DSSP algorithm.

Available reference sets are based on x-ray structures, resulting in reduced accuracy in the analysis of disordered or P_{II} structure as these reference sets are not available.[94] CaM is highly structured with no P_{II} structure and the estimation of α-helical content is considered to be reliable.

CaM-antagonist binding was first analyzed using far-UV CD, with antagonists being titrated up to 20 equivalents in relation to CaM in the presence of Ca^{2+} (1 mM). The raw spectra can be seen in Figure 2.2. Above 20 equivalents and high tension (HT) values approach the limit at which point the detector becomes saturated. The baseline spectrum with only CaM present displayed the characteristic double minima at 208 nm and 222nm associated with canonical alpha-helical secondary structure. Ellipticity at 222 nm is considered as a reasonable metric for percent helicity of protein structures.[95,96] The ratio of bands at 208 nm an 222 nm is often used an additional metric of α-helicity however the effect of protein sequence on this ratio remain ill-defined.[97] TFP, a known potent CaM antagonist, was used as a positive control against which to compare structural rearrangements of CaM induced by aMT and AMK. The titration of TFP resulted in reduced molar ellipticity at both minima. The magnitude of this change is linear in relation to equivalents of TFP added until approximately 7 equivalents, at which point it begins to plateau until no further change in molar ellipticity is observed after approximately 10 equivalents added (Figure 2.3A). BestSel secondary structure analysis estimated a drop in α-helical content from 62.9% to 44% (Figure 2.4A). Similarly, AMK notably reduced intensity CD signal with the magnitude of change gradually reducing after approximately 10 equivalents (Figure 2.3B). This reduction corresponded to a drop in α-helicity from 64.7% to 44.9% (Figure 2.4B). The titration of aMT resulted in minimal changes in signal at lower concentrations, with larger changes produced at higher concentrations (Figure 2.3C) although the signal appears

highly distorted at elevated amounts of the ligand (Figure 2.2C). 20-fold excess corresponded to an absurdly low 14.3% α-helical content (Figure 2.4C), thus the significance of these findings is moot. Indeed, previous CD studies involving CaM and aMT showed a similar loss in CD signal but suggested it may be the result of optical activity of aMT in the UV range.[73] This was postulated as this behaviour was also seen in a titration where CaM was replaced by BSA.

Although little can be drawn from the results of the aMT titrations, the titration data for AMK and TFP portray the characteristic shape of a saturable binding (Figure 2.3). The overarching trajectory of the curves can provide empirical information regarding the strength of interaction. TFP appears to saturate CaM as total concentrations of the ligand approach 10 molar equivalents, indicating a relatively strong interaction. AMK, conversely, does not saturate CaM but the magnitude of change tapers off gradually as ligand concentration increases, suggesting a weak interaction.

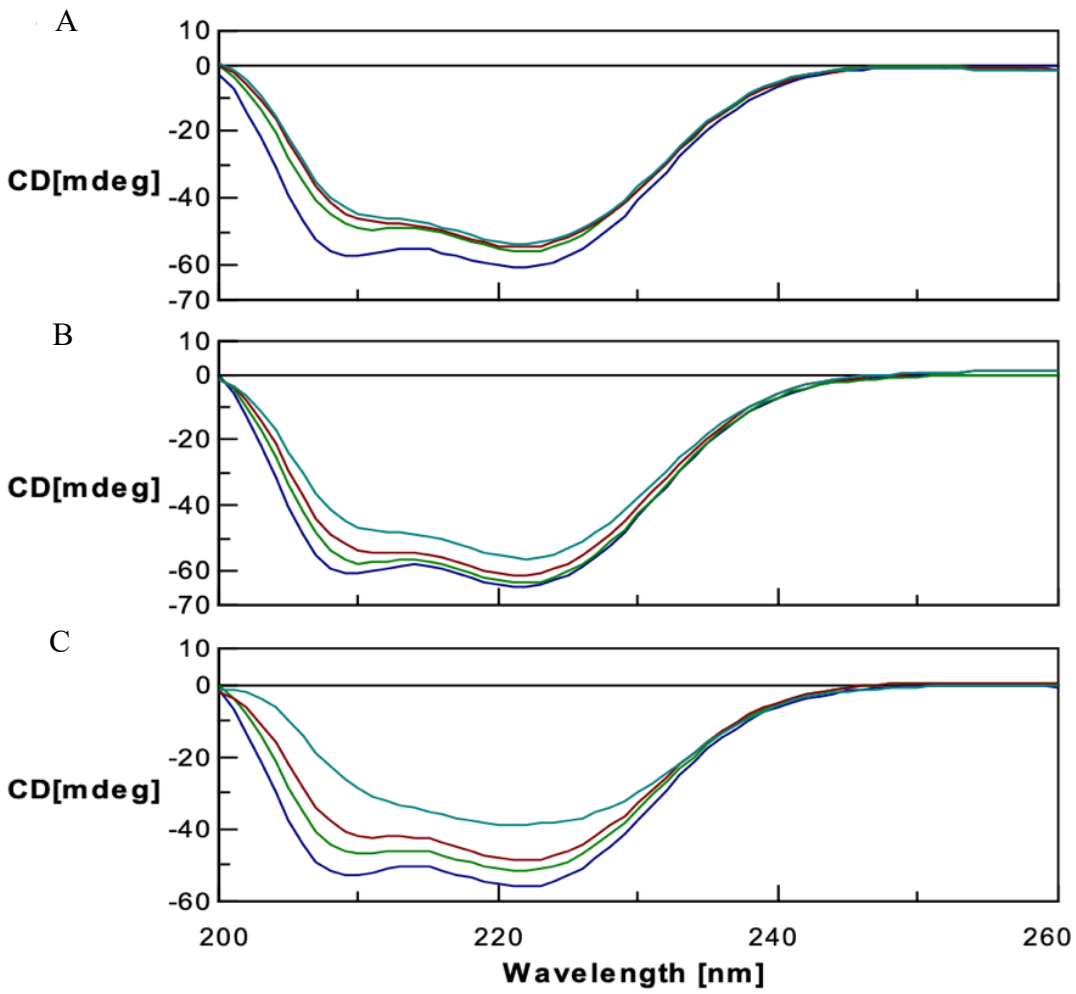

Figure 2.2 Far-UV CD CaM-antagonist titration.
CD Titrations acquired from 260-200 nm for CaM and increasing concentrations of (A) TFP, (B) AMK and (C) aMT (dark blue = 12 μM CaM, green = 12 μM CaM + 5x antagonist, red 12 μM CaM + 10x antagonist, light blue = 12 μM CaM + 20x antagonist). Spectra were processed using the JASCO Spectra Manager Suite.

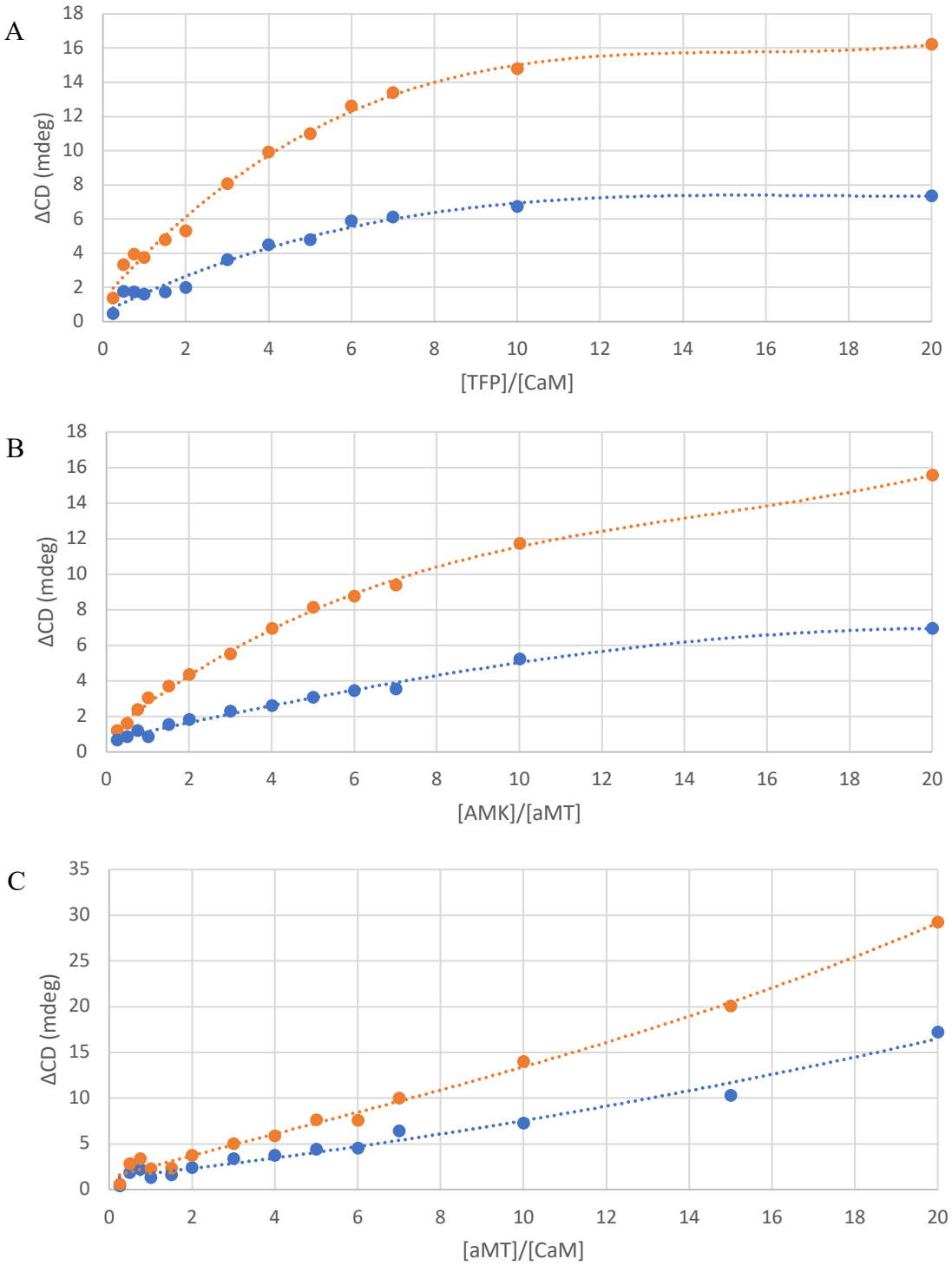

Figure 2.3 Far-UV CD CaM-antagonist titration curves.
Changes in CD signal at 208 nm (orange) and 222 nm (blue) from titrations acquired from 260-200 nm involving increasing concentrations of (A) TFP, (B) aMT and (C) AMK.

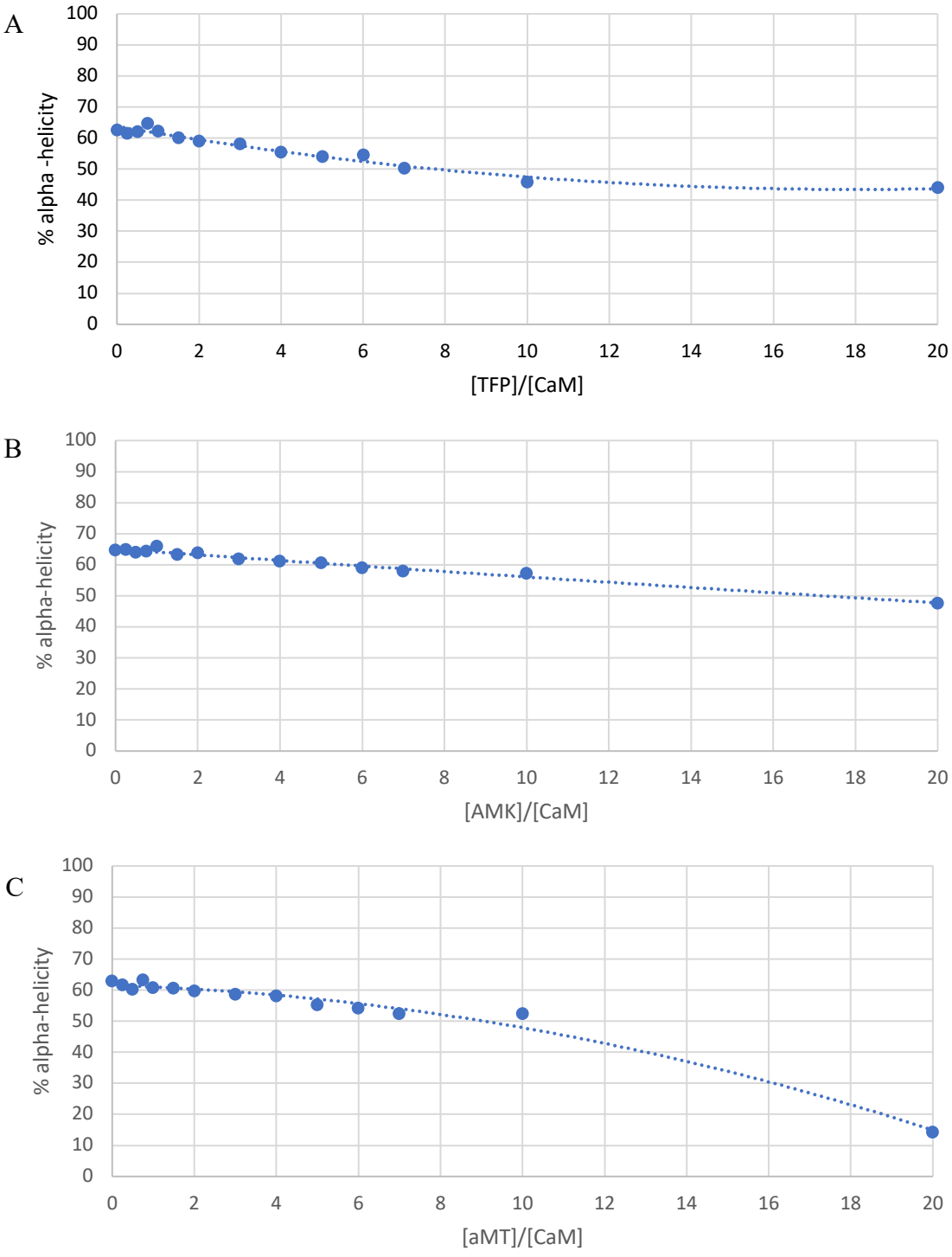

Figure 2.4 Changes in α-helical content predicted by BestSel.
Changes in secondary structure according to BestSel predictions are shown over the course of far-UV CD titrations acquired form 260-200 nm for (A) TFP (A), (B) AMK and (C) aMT.

Far-UV circular dichroism was also used to characterize interactions between CaM and the CaM-binding domain peptides of NOS isoforms, known to bind with 1:1 stoichiometry, at saturated levels of Ca^{2+} both in the presence and absence of the antagonists. The NOS peptides are unstructured in solution, however upon binding to CaM they adopt an α-helical conformation resulting in increased CD signal.[98] CaM was incubated for 20 minutes at room temperature with the antagonists at a 7-fold excess before the NOS peptide was added. The magnitude of change in molar ellipticity was compared to the control with no antagonist present. The addition of TFP yielded significantly smaller increases in signal when the nNOS peptide was added, however the increases were approximately equal to the control in the cases of eNOS and iNOS (Figure 2.5A). This suggests a TFP-mediated disruption of CaM-nNOS complex formation, which is in accordance with TFP's documented capacity for isoform-specific reduction in nNOS activity.[58,59,56,99] AMK generated a spectral profile similar to TFP, appearing only to impact CaM-nNOS formation and no significant changes observed with other isoforms (Figure 2.5B). This is in agreement with the purported specificity from studies involving AMK and is suggestive of previously posited mechanisms involving AMK-mediated structural change impacting the CaM-nNOS complex.[61–63] The presence of aMT produced non-specific reduction in molar ellipticity change, however the magnitude of these differences was significantly smaller than in the case of TFP (Figure 2.5C).

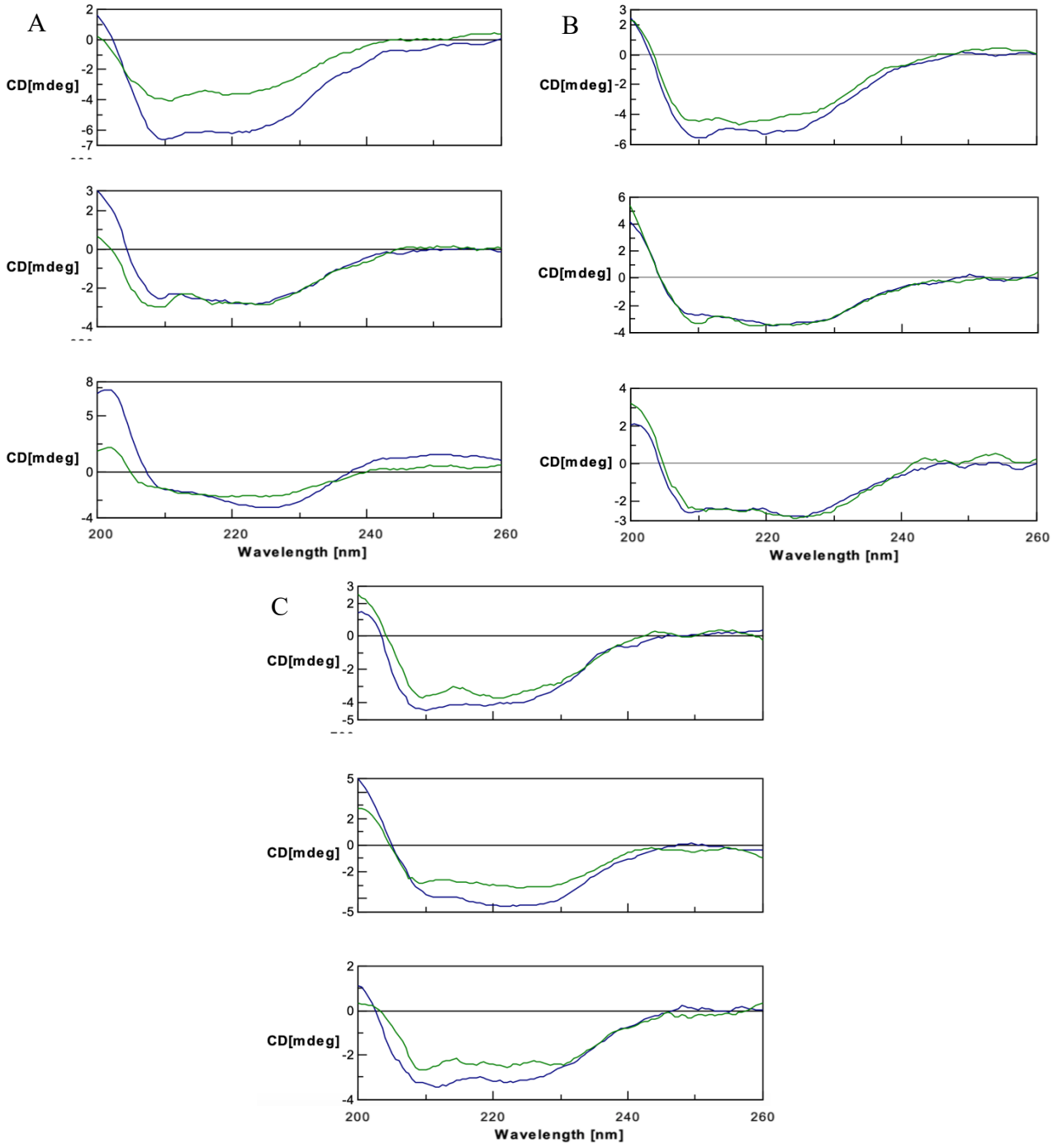

Figure 2.5 Antagonist-induced changes in subtractive Far-UV CD analyses of CaM and peptide-bound CaM.
CD spectra of peptide-bound CaM subtracted by CaM alone with (green) and without (blue) (A) TFP, (B) AMK and (C) aMT. For each antagonist, the top panel corresponds to nNOS, the second to eNOS and the third to iNOS. Spectra were processed using the JASCO Spectra Manager Suite.

Key to understanding the mechanism responsible for AMK's specificity is its interaction with each NOS isoform. The effect of AMK on the secondary structure of the NOS peptides was investigated using trifluoroethanol (TFE), which mimics hydrophobic environments and is known to induce α-helical conformation in peptides with a propensity to adopt this conformation. No structure for the peptide of any isoform was seen in buffer solution with 0% TFE. The α-helical content of the peptide was compared by recording spectra with increasing concentrations of TFE, which yielded increasingly negative minima at 208 nm and 222 nm. Negative ellipticity plateaued at 40% after which point any further change was negligible. AMK showed no significant impact on the induced helicity the NOS peptides, regardless of isoform. This would indicate that specificity is not the result of isoform-dependant rearrangement of secondary structure of the peptide prior to CaM binding.

2.3.2 Isothermal Titration Calorimetry

Isothermal Titration Calorimetry (ITC) was used to analyze the thermodynamic profiles of the interactions between AMK, CaM and NOS peptides. Since the values obtained for binding constants show slight variations when performed using different methods and conditions, all of our experiments were performed by ITC using exactly the same conditions.[100,101] HEPES buffer was used to reduce background associated with (de)protonation heat effects.

Initial experiments attempted to characterize molecular recognition of AMK by CaM, with the peptide excluded from the system (Figure 2.6). In the presence of Ca^{2+} (1 mM), AMK binds to CaM by an exothermic interaction, and proceeds with a negative enthalpy (ΔH) and a positive entropy (ΔS). This demonstrates the reaction occurs with favourable enthalpy and entropy, corresponding to hydrophobicity and Van der Waals components of association.

Smaller endothermic peaks trail the exothermic ones following each injection, suggesting association followed by rapid dissociation. Binding proceeded with extremely low affinity indicated by the failure to produce a viable isotherm to generate binding parameters even at high concentrations of AMK (2 mM). This indicates the strength of the interaction is too weak and beyond the experimental limit of detection. Given the probability of CaM-AMK complexation occurring with a K_d > 1mM, it is unlikely conventional ITC experiments are capable of directly quantifying the interaction. This data is in agreement with the weakly associating behaviour suggested by the CD titration curve for AMK in section 2.3.1.

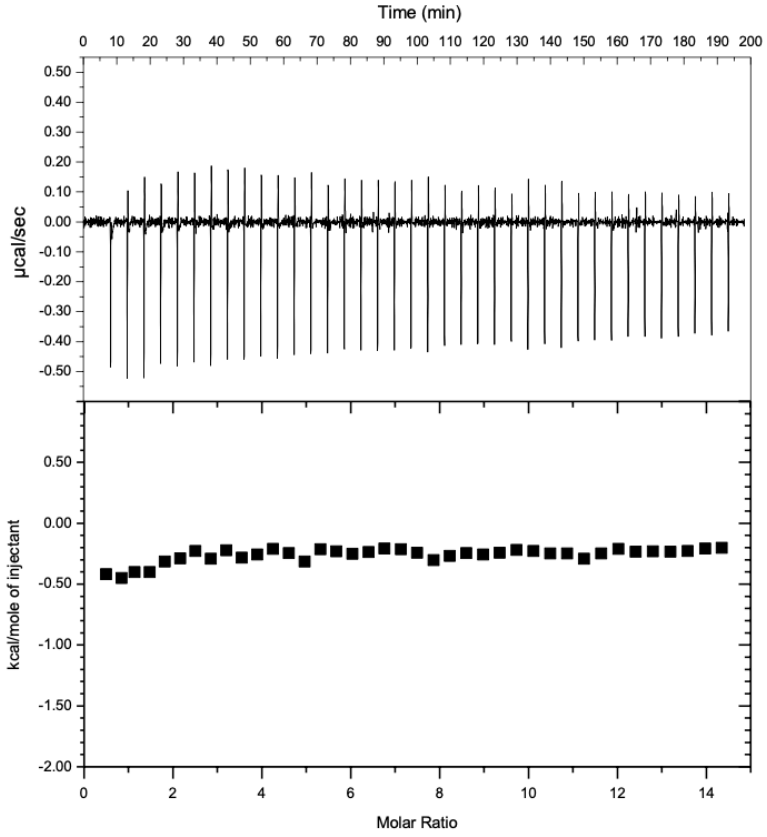

Figure 2.6 Results from CaM-AMK ITC experiments.
Raw data (top panel) and processed heats of injection (bottom panel) from 2 mM AMK into 10 µM CaM. A viable isotherm was not produced.

ITC was used to analyze the putative low affinity binding between CaM and AMK, making use of a method introduced by Zhang and Zhang for deriving low-affinity binding parameters based on curve fitting using a one-site model.[102,103]. The binding constant for the low affinity ligand is determined using the equation $K_b = ([K_a / K_{app}] - 1) \times (1 / [B]_t)$ where K_A and K_B are the binding constants for the high affinity and low affinity ligand (NOS and AMK respectively). K_{app} is the experimentally measured binding constant, and $[B]_t$ is the ligand concentration.

Complexation of CaM and NOS peptides was first conducted with no AMK present, and affinities were determined to be very similar to previously reported values.[41] Particular emphasis was given to CaM-eNOS and CaM-nNOS, as the Ca^{2+}-independent binding of iNOS likely circumvents purported the Ca^{2+}-dependant inhibition from AMK. Both eNOS and nNOS bound to CaM in an exothermic manner in the presence of Ca^{2+} (1 mM), with negative ΔH and positive ΔS. Both peptides showed a 1:1 binding stoichiometry as expected. The presence of 100-fold excess AMK resulted in a modified CaM-nNOS isotherm (Figure 2.7A,B). This isotherm possessed initial endothermic peaks, representing a ~3.9 kcal/mol increase in ΔH relative to the AMK-free titration. As the peptide and CaM neared 1:1 stoichiometry these peaks disappeared, and the second half of isotherm reverted to one resembling baseline CaM-nNOS association as AMK is displaced by the peptide. Peptide into AMK control experiments produced consistent endothermic heats of injection with a ΔH value of ~3.4 kcal/mol, although no saturation was achieved (Figure 2.8). This would indicate the possible existence of a weak interaction between nNOS and AMK and rationalize the previously discussed change in isotherm. Initial endothermic peaks are potentially the result of two events: nNOS peptide interacting with excess AMK, and AMK being ejected from CaM as CaM binds to nNOS. At the inflection point where 1:1

stoichiometry is observed, AMK is completely ejected. eNOS into AMK control experiments produced endothermic peaks, albeit of a much smaller magnitude ($\Delta H \cong 0.9$ kcal/mol) relative to its neuronal counterpart. Due to the apparent complexity of the systems, the competition model is not applicable as it assumes no interaction between high and low affinity targets.

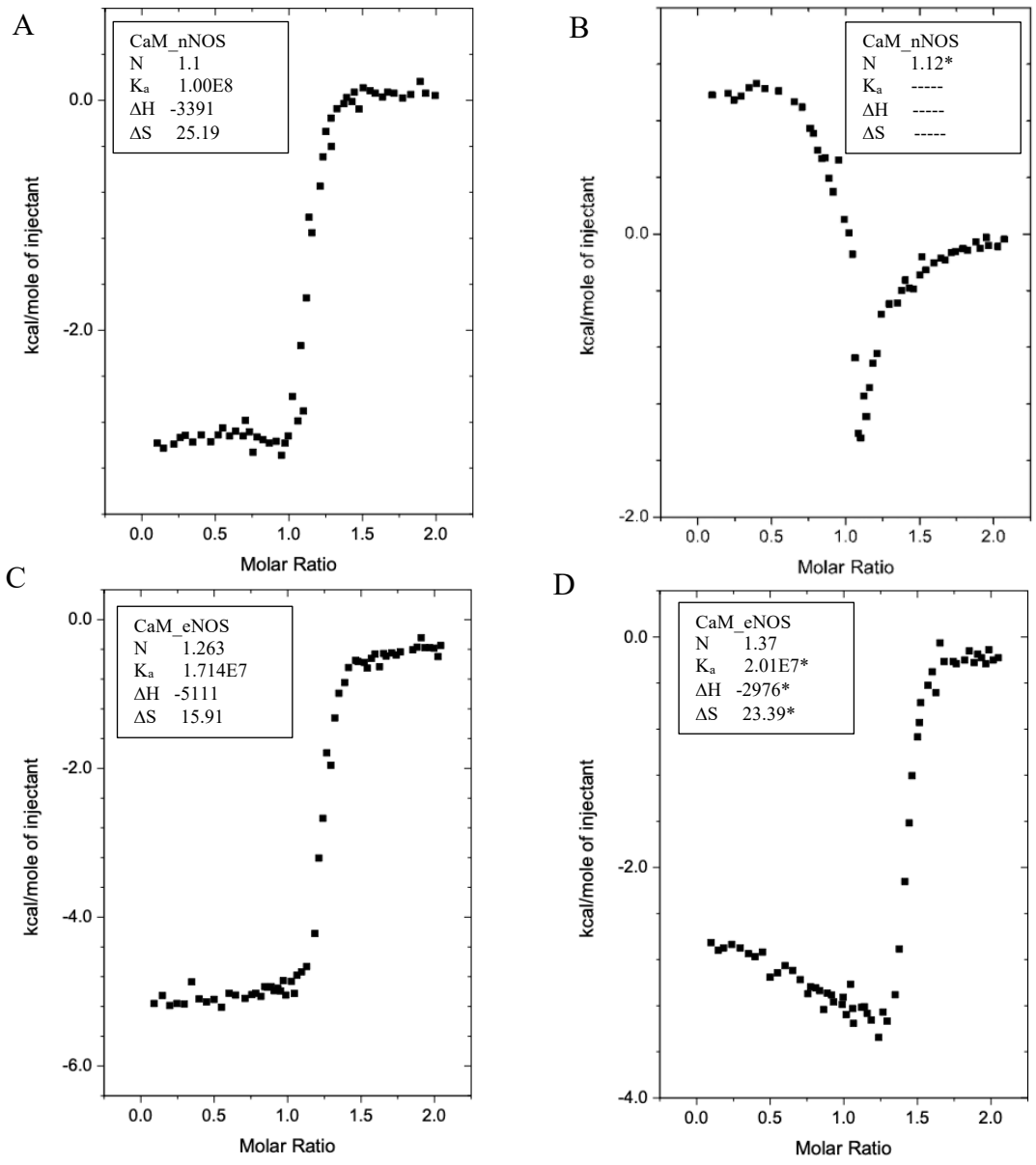

Figure 2.7 Representative curves of CaM, nNOS and eNOS peptides with and without AMK. (A) 250 μM nNOS peptide into 25 μM CaM, (B) 250 μM nNOS peptide into 25 μM CaM pre-incubated with 100-fold excess AMK, (C) 250 μM eNOS peptide into 25 μM CaM and (D) 250 μM eNOS peptide into 25 μM CaM pre-incubated with 100-fold excess AMK.

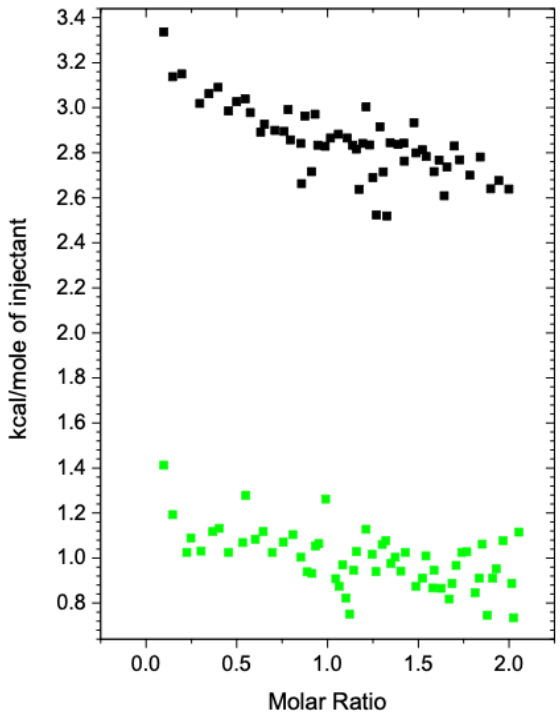

Figure 2.8 Results from AMK-nNOS and AMK-eNOS ITC experiments.
250 μM nNOS peptide into 2.5 mM AMK (black) and 250 μM eNOS peptide into 2.5 mM AMK (green). Molar ratio corresponds to the ratio between injected peptide and the CaM concentration from the competition assays.

Not only were competition assays unable to show a direct AMK-mediated impact on CaM-NOS complexation, they were also unable to indirectly quantify the strength of CaM binding to AMK. In an attempt to successfully accomplish the latter, a lower affinity peptide with no observed heats of association with AMK was used in hopes that any impact had from the antagonist would become apparent. Rat NSCaTE (rNSCaTE) peptide, a lower-affinity and Ca^{2+}-sensitive binding site for CaM in L-type Ca^{2+} channels, was selected and titrations were conducted as previously described for the NOS peptides.[104] rNSCaTE into AMK control produced little to no signal, as did all CaM, AMK, and peptide to buffer experiments. Interestingly, competition assays showed increased affinity between CaM and rNSCaTE with AMK present

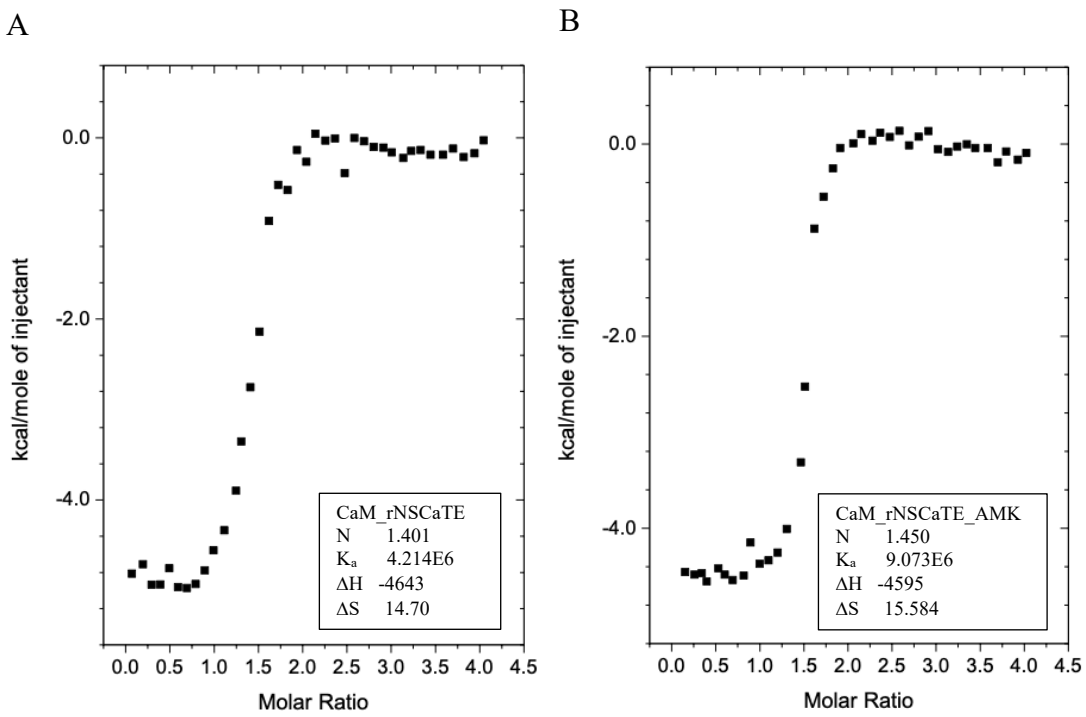

Figure 2.9 Representative ITC results from CaM and rNSCaTE peptides with and without AMK.
(A) 500 μM rNSCaTE peptide into 25 μM CaM and (B) 500 μM rNSCaTE peptide into 25 μM CaM pre-incubated with 100-fold excess AMK.

($K_d \cong$ 4.2E6 M) than experiments absent AMK ($K_d \cong$ 9.1E6 M) (Figure 2.9). ΔS was determined to be slightly lower without AMK and ΔH was unchanged. It is possible that the antagonist induces a conformational change in rNSCaTE that renders it more suitable for CaM binding. ITC competition assays are typically conducted with a model assuming a reduction in affinity will be observed, as such it remains unclear as to whether binding parameters can be indirectly determined in instances where the opposite in reported.

2.3.3 Gel Mobility Assays

Band shift assays on non-denaturing urea gels were used to further analyze CaM-nNOS peptide complex formation in the presence of the antagonists. The extremely consistent results, despite change in experimental design, are epitomized in Figure 2.10. High affinity between

CaM and the peptide is easily detectable using this method, manifesting in large changes in band mobility relative to unbound CaM. In the presence of Ca^{2+}, the electrophoretic mobility of CaM was significantly reduced by the 1:1 addition of the nNOS peptide. Pre-incubation of CaM with a stoichiometric amount of TFP prior to loading with nNOS produced two bands: one with similar mobility to the CaM:nNOS complex and a weaker band with similar mobility to unbound CaM. This indicates that TFP binds to CaM in such a manner that it reduces the concentration of CaM available for complex formation with the peptide. Similar bands do not appear when CaM is pre-incubated with aMT or AMK, indicating that any competition is considerably weaker. In assays conducted with no peptide present, the relative mobility of unbound holo-CaM was not altered appreciably by any of the antagonists regardless of urea concentration, suggesting their minimal impact on overall shape or charge. Gels with lower urea concentrations and native-state gels produced identical results. 4M urea and native gel mobility assays were also conducted with significantly higher concentrations of antagonists in an attempt to find the threshold concentration for observable competition.

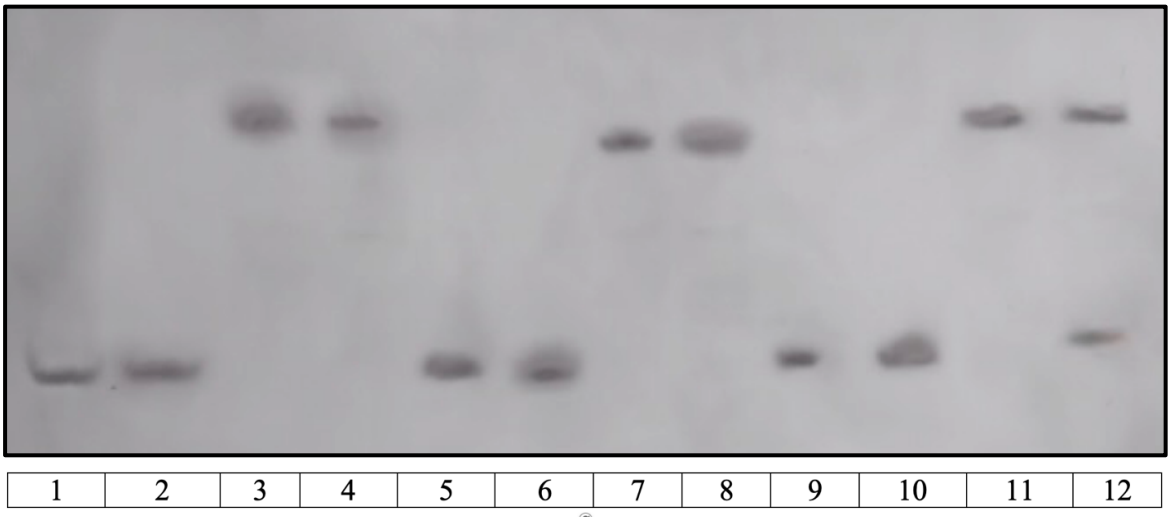

Figure 2.10 4 M Urea-PAGE gel at with 1000-fold excess antagonist concentrations. CaM (lane 1), CaM + aMT (lane 2), CaM + nNOS peptide (lane 3), CaM + aMT + nNOS peptide (lane 4), CaM (lane 5), CaM + AMK (lane 6), CaM + nNOS peptide (lane 7), CaM + AMK + nNOS peptide (lane 8), CaM (lane 9), CaM + TFP (lane 10), CaM + nNOS peptide (lane 11), and CaM + TFP + nNOS peptide (lane 12).

CaM samples loaded with up to 1000-fold excess aMT and AMK (Figure 2.10) showed no changes in electrophoretic mobility and no residual unbound CaM bands were seen when the peptide was present. This stands in contrast to previous gel mobility studies with aMT and CaM in which residual CaM bands were observed at as low as 10-fold excess aMT, however myosin light-chain kinase (MLCK) was used as opposed to nNOS.[73] Additionally, Camacho *et al*. showed significant changes in the electrophoretic mobility of unbound holo-CaM in the presence of 1 mM aMT and synthetic analogues similar to AMK, but the CaM concentration was not defined.[63] Our negative results do not explicitly eliminate the possibility of binding competition, particularly due to the highly qualitative nature of gel data analysis but do support the likelihood of low CaM-AMK affinity.

2.3.4 Enzyme Kinetics and SPR Studies

The reduction of metHb yielded 5.90 % deoxyHb, 23.94 % and 70.16 % oxyHb, which is in agreement with expected values from previous studies.[91] Calibration curves of metHb and oxyHb displayed the predicted linear relationship between absorbance and concentration. The difference in slopes was used to calculate OD_{401}, which was determined to be 0.111 OD_{401} / nM.

Enzyme-initiated OxyHb capture assays were conducted first, where CaM was incubated with AMK prior to initiating the reaction. AMK ranging from 33- to 1000-fold excess of nNOS did not appear to significantly influence enzyme activity, with small differences in activity falling within the margins of standard error (Figure 2.11A). These small changes are also not proportional with respect to concentration of AMK, further reducing the likelihood that the antagonist is the cause of the variances. In contrast, TFP in 1000-fold excess of nNOS greatly reduced V_{max} values, particularly at lower concentrations of CaM. Substrate-initiated assays

where nNOS was incubated with AMK were carried out to further assess if direct AMK-nNOS complexation is involved in isoform-selective inhibition. L-NG-nitroarginine (LNNA) was used as a positive control for inhibition in this instance as it directly binds to nNOS as opposed to antagonizing CaM (Figure 2.11B). Despite the change in preparation, AMK did not produce observable differences in nNOS activity. V_{max} values at each CaM concentration were extremely similar regardless of the AMK concentration.

A

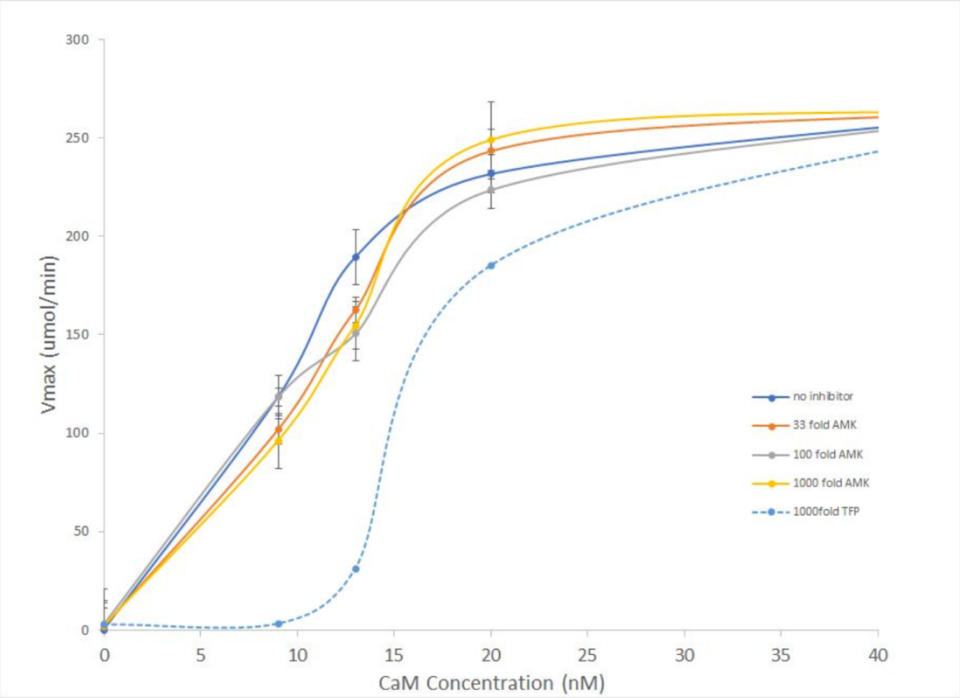

B

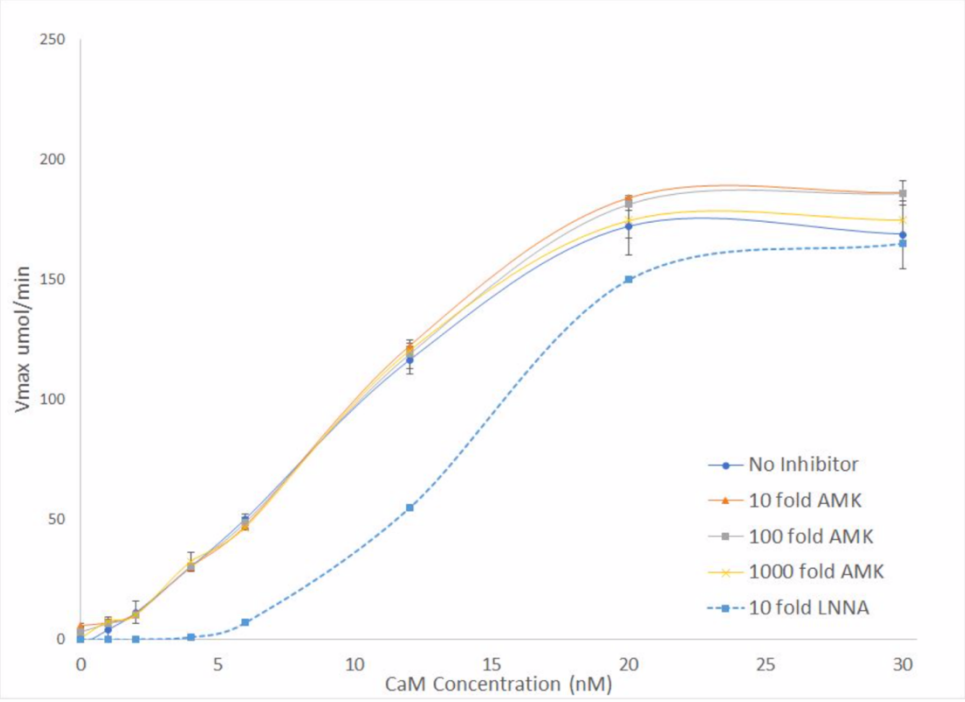

Figure 2.11 Oxyhemoglobin capture assays.
(A) Enzyme-initiated assays using TFP as a positive control and (B) substrate-initiated assays using LNNA as a positive control carried out at increasing concentrations of CaM ranging from 0-40 nM. AMK did not notably impact enzymatic activity regardless of CaM concentration.

The lack of apparent AMK-induced enzyme activity inhibition contrasts a previous *in vitro* enzyme kinetics study using homogenates of rat striatum.[62] Their findings suggested unambiguous, Ca^{2+}- and dose-dependent inhibition of nNOS by AMK. These differences are likely the result of variances in sample sources and experimental protocols. Most kinetics studies that have successfully shown AMK- or aMT-mediated inhibition use biological nNOS samples and follow a previously described method which monitors the conversion of L-arginine to L-citrulline using a biological source of nNOS as opposed to a purified source.[105] This biological source is typically a striatal rat brain homogenate. Again we see differences in behaviour between biological and purified samples, as has been reported in the case of CaM-aMT binding.[106] The few assays that show inhibition of a purified enzyme are carried out under lower Ca^{2+} concentrations, typically around 17.5 μM.[105] Our results, therefore, do not discard the possibility of AMK-mediated inhibition but instead point to the potential importance of other factors not accounted for within the simplified system of the oxyHb capture assay.

Additional analyzation of binding kinetics under more physiologically relevant conditions could be of significant value. In addition to using biological samples as previously described, perhaps the most impactful modification would be to reduce Ca^{2+} to concentrations similar to elevated free Ca^{2+} values in the body, or approximately 225 nM.[107] In studies where CaM exists in a partially Ca^{2+}-replete state, overall affinity for the CaM-binding domain peptide of NOS is reduced. The C-terminal domain, which has a 10-fold higher affinity for Ca^{2+} compared to the N-terminal domain, saturates first and binds to NOS. The Ca^{2+}-deplete N-terminal domain largely retains its apo-CaM conformation and thus hydrophobic cavities within are not exposed, resulting in a much weaker association with the NOS peptide.[107,108] This

deteriorated binding strength could potentially facilitate CaM antagonism from compounds such as AMK and help elucidate the significant effects seen in previous studies.[61–63]

SPR displacement assays revealed a subtle effect of AMK on CaM-NOS complexation. Spectra were first obtained with no antagonist present to evaluate binding kinetics of CaM with the NOS peptides. The experimentally determined k_a values for eNOS and nNOS were highly analogous to literature values (Table 2.5). k_d and K_d constant were also reasonably comparable although both were higher than expected values.

Table 2.5 Comparison of experimentally determined binding parameters from SPR.

	k_a (M^{-1} s^{-1}) x 10^5	k_d (s^{-1}) x 10^{-4}	K_d (M) x 10^{-9}
nNOS[109]	1.58	7.9	5.0
eNOS[107]	1.31 ± 0.48	3.5 ± 1.0	2.7 ± 0.2
nNOS	1.90 ± 0.13	30.1 ± 0.15	18.8 ± 0.32
eNOS	2.17 ± 0.001	26.2 ± 0.02	11.7 ± 0.02

Displacement assays were carried out by pre-incubating CaM with AMK at varying concentrations prior to injection and comparing binding parameter to baseline experiments (Figure 2.13). In nNOS peptide displacement assays, 1000-fold excess AMK produced minimal effects on the equilibrium dissociation constant ($K_d \cong 49.6$ nM), whereas 10000-fold excess appeared to produce a notable increase ($K_d \cong$ 206.3 nM). In comparison, eNOS displacement assays at 10000-fold excess AMK had no impact on binding to CaM ($K_d \cong$ 15.3 nM). These results, although subtle, may suggest a structural basis for the purported isoform-dependent inhibitory characteristics of AMK, however further investigation is required.

A

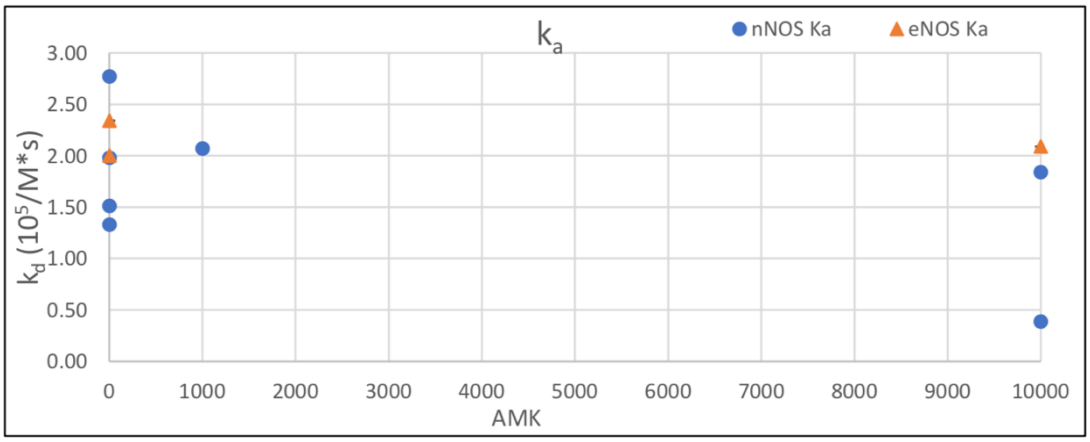

B

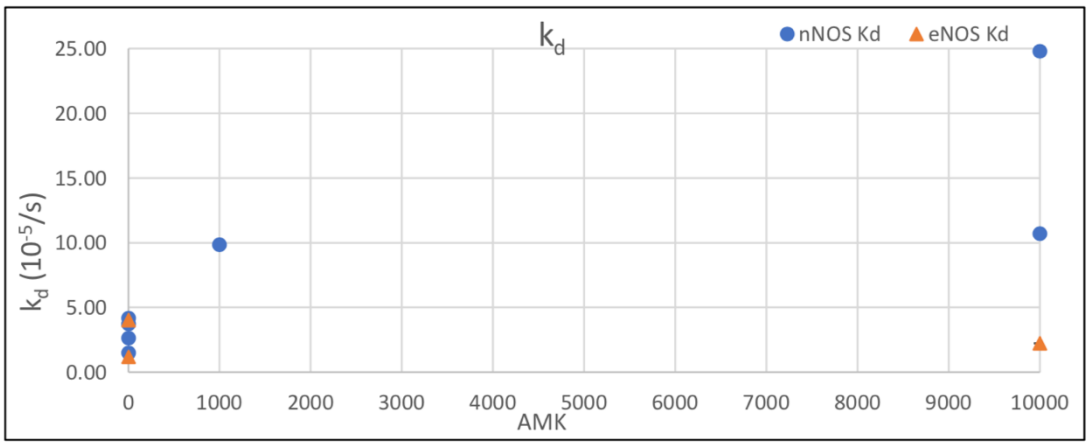

C

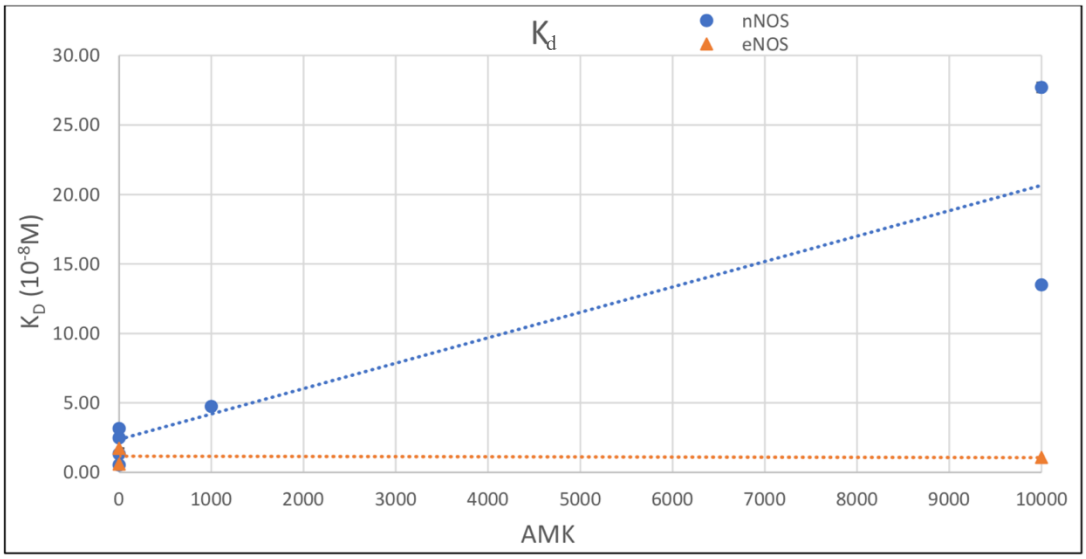

Figure 2.12 ITC competition assays with nNOS and eNOS peptides.
Comparison of (A) k_a, (B) k_d and (C) K_d values for CaM binding to nNOS and eNOS peptides with increasing AMK concentrations. nNOS data is shown in blue and eNOS in orange. Trends in K_d values relative to AMK concentrations are represented by dashed lines.

2.4 Conclusions

We set out to understand the effects of aMT and AMK, with particular focus on the latter, on complexation between CaM and NOS isoforms. Previous studies reported both compounds were able to inhibit NOS activity *in vivo* and *in vitro*, with experimental evidence suggesting this is accomplished through antagonizing CaM.[110,111,63,61] Various other biophysical analyses have been carried out involving CaM and aMT and indicate a weak interaction between the two compounds.[73,74] The present study build upon previous work and provides hitherto unknown information regarding the interaction between CaM and AMK. Although the titration of AMK in far-UV CD experiments produced changes in the CD signal for CaM, saturation was not achieved. Similarly, gel mobility assays involving AMK far in excess of CaM did not produce any observable deviation in electrophoretic mobility. Direct assessment of CaM-AMK binding using ITC was unsuccessful, as saturation was not possible within the reasonable bounds of experimental design. These results strongly suggest a similarly weak interaction (likely $K_d > 1$ mM) between CaM and AMK as previously reported in the case of aMT.[73,74]

The impact of AMK on CaM complexation with the CaM-binding domain peptides of NOS and nNOS enzyme activity were similarly subtle. Although affinities between CaM and NOS peptides appeared unaltered by AMK, respective isotherms for eNOS and nNOS peptides were modified by the presence of the antagonist but the nature of the interaction remains unclear. SPR competition assays did show a potential loss in binding affinity in the case of nNOS, but only at extremely high concentrations of AMK. SPR assays also showed a potential isoform-dependant impact, with eNOS binding remaining unaffected at the same high antagonist concentrations. Although the capacity for potent competition is doubtable, the purported isoform-specific effects are promising. This specificity was further reflected far-UV CD

experiments in which the increase in secondary structure seen when the nNOS peptide binds to CaM was reduced when AMK was present, but not in the case of other isoforms. Although nNOS enzyme activity was unaffected in oxyHb capture assays, this does not necessarily negate the capacity of AMK to act as a CaM antagonist. Instead, it is perhaps reflective of a need for more biologically relevant conditions, such as physiological Ca^{2+} concentrations or the use of a biologically derived source of the nNOS enzyme.

Chapter 3

Chemical Shift Perturbation and Solution Structures of the CaM-AMK Complex

3.1 Introduction

The use of structure-based analysis of protein-ligand interactions has proved highly invaluable, particularly in field of drug design.[112] Nuclear magnetic resonance spectroscopy (NMR) is amongst the most useful tools in this respect, allowing precise detailing of many biomolecular complexes and is well-suited to ascertain an understanding of the interaction between CaM and AMK.

Although several studies have documented the capability of AMK inhibit nNOS *via* antagonizing CaM, there is little in the way of a structural explanation of how this manifests on a molecular scale.[61–63] In characterizing the binding between AMK and CaM, it becomes possible to discern the means by which this antagonism is accomplished. To this end, NOE-based techniques using 2D and 3D NMR experiments can be highly effective and can produce high resolution structures of protein-ligand complexes. The caveat is that intermolecular NOEs are not always visible, particularly for weak interactions and thus alternate NMR techniques such as chemical shift monitoring can be used in parallel. Indeed, a previous study investigating the complexation of aMT and CaM found that no such NOEs were observed due to the millimolar range residue-specific K_d values.[74] Here we present a comprehensive structural analysis of the CaM-AMK complex using NMR, combining 2D NMR ^{15}N-HSQC titrations with 3D structure determination of CaM from NOE distance constraints. In this way, changes in the conformation of CaM when bound to AMK and the probable location of binding surfaces were elucidated.

3.2 Methods and Experiments

3.2.1 Expression and Purification of Isotopically labelled CaM

An overnight culture of transformed E. coli BL21 (DE3) with pET9dCaM was used to inoculate 1 L of M9 media (11.03 g/L $Na_2HPO_4 \cdot 7H2O$, 3.0 g/L KH_2PO_4, 0.5 g/L NaCl, 2 mM $MgSO_4$, 0.1 mM $CaCl_2$, 3 μM $(NH_4)_6(MO_7)_{24}$, 400 μM H_3BO_3, 30 μM $CoCl_2$, 10 μM $CuSO_4$, 80 μM $MnCl_2 \cdot 4H_2O$, 10 μM $ZnCl_2$, 10 mM $FeSO_4$, 100 μg/mL kanamycin) containing 2 g/L 13C-glucose and 1 g/L 15NH4Cl. ^{15}N-^{13}C-CaM was purified as previously described in Chapter 2. The samples were prepared for NMR experiments via a buffer exchange into NMR solution (100 mM KCl, 10 mM CaCl2, 0.2 mM NaN_3, 90% H2O/10% $2H_2O$) at pH 6.0 using a YM10 centrifugal filter device (Millipore Corp., Billerica, USA). All NMR samples contained at least 350 μM CaM in a total volume of 500 μL. The samples were transferred into 5 mm NMR sample tubes and stored at 4°C until required for NMR experiments.

3.2.2 NMR Spectroscopy Data Acquisition and Analysis

NMR spectra were recorded at 25°C on a Bruker 600 MHz DRX spectrometer equipped with XYZ gradients triple-resonance HCN probe (Bruker, Billerica, MA, USA). Spectra were analyzed using the Computer Aided Resonance Assignment (CARA) program.[113]

Specific assignments of the CaM backbone resonances were achieved using a combination of 2D HSQC and 3D triple resonance experiments including HNCA, CBCA(CO)NH, HN(CO)CA, and HNCO.[114,115] Side-chain resonances were assigned using various TOCSY type experiments; HC(C)H-TOCSY, (H)CCH-TOCSY and H(CCO)NH.[116]

3.2.3 ^{15}N-HSQC NMR Titration

^{15}N-HSQC spectra were acquired with AMK being titrated into samples containing 350 μM CaM at pH 7.3. Spectra were recorded at 1-2 equivalent intervals until an AMK:CaM ratio of 7:1 was achieved. Changes in pH caused by the addition of AMK were accounted for by the titration of 0.1 M NaOH.

The changes in chemical shifts of individual nuclei resonances were fitted using the standard non-linear least-squares method. K_d values were determined using the equation $\Delta\delta_{obs} = \Delta\delta_{max}\ \{([P]_t + [L]_t + K_d) - [([P]_t + [L]_t + K_d)^2 - 4[P]_t[L]_t^{1/2}\}/2[P]_t$ where $[P]_t$, $[L]_t$, $\Delta\delta_{obs}$ and $\Delta\delta_{max}$ are total protein concentration, total ligand concentration observed change from the free state and the maximum shift change upon saturation respectively.

3.2.4 Structure Calculations of the CaM-AMK Complex

The ^{1}H, ^{13}C and ^{15}N resonance assignments were used to identify constraints for structure calculations. Distance constraints for the solution structure of CaM-AMK were obtained from 3D ^{15}N-NOESY-HSQC and ^{13}C- NOESY-HSQC spectra. Intramolecular NOEs of the ligand and intermolecular NOEs were analyzed with ^{15}N-double-filtered NOESY and ^{15}N/^{13}C-edited double-filtered NOESY spectra acquired on samples containing labeled CaM and unlabeled AMK.[117–119] In addition, dihedral angle restraints were derived from chemical shift analysis with TALOS+.[120]. CNSsolve version 1.2 was used for structure determination and refinement.[121] Calculations were initiated with an extended conformation file and run through several iterations of a standard simulated annealing protocol in order to minimize the energies. The 20 lowest-energy structures were generated and averaged.

3.3 Results and Discussion

3.3.1 3D CaM-AMK Complex Structure Calculations.

The NMR analysis of CaM complexation with 7 molar equivalents of AMK in the sample was conducted according to routine procedures with backbone resonance assignment (Figure 3.1A) based on 3D triple resonance techniques. Although spectral changes in fast exchange on the NMR timescale brought on by AMK were observed, these changes were small enough that previously assigned chemical shifts of wildtype holo-CaM could be used as a starting point. The HNCA experiment (Figure 3.1B) was used in conjunction with CBCA(CO)NH and HN(CO)CA experiments. Collectively, these techniques allowed for the complete backbone assignments for the CaM-AMK complex, with the exception of prolines. Sidechain resonances for CaM were determined using HC(C)H-TOCSY, (H)CCH-TOCSY and H(CCO)NH experiments. ^{15}N-double-filtered NOESY and ^{15}N/^{13}C-edited double-filtered NOESY in an attempt to assign AMK.

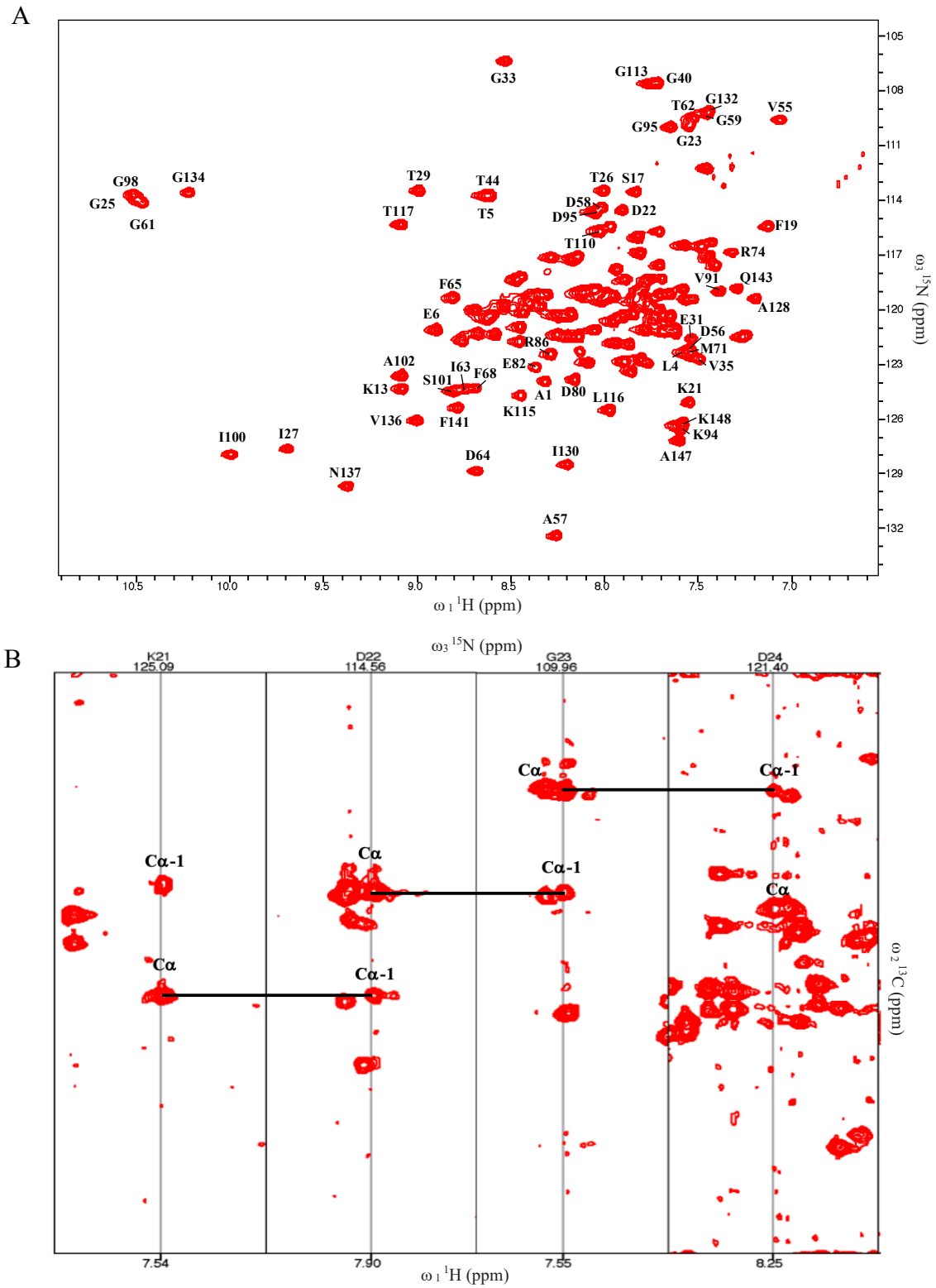

Figure 3.1 Composite figure of NMR structural data.
(A) ^{15}N-HSQC spectrum of the CaM structure when bound to AMK. (B) 3D HNCA strips of sequential amino acids K21 to D24. The connection between alpha carbons are shown.

No intermolecular NOE effects were observed between AMK and CaM, similar to results seen in NMR experiments involving CaM and aMT.[74] The absence of these NOEs is likely the result of the very weak interaction, and as a result determining the precise contact formation involved in binding becomes infeasible. 3D structure determination is still valuable in this instance, however, as it can elucidate the conformational changes in CaM upon forming a complex with AMK. CNSsolve was used in accordance with experimentally determined NOE constraints and dihedral angle constraints from TALOS+.

Solution structures of CaM when bound to AMK are extremely similar to the unbound form of holo-CaM, suggesting that AMK has a minimal impact on structure. No long-range NOEs were observed between helices of opposing globular domains, which characterize a typical bound conformation. Superposition of the lowest energy structures (Figure 3.2A) also shows the mobile nature of the linker region, which is typical of holo-CaM in solution. The N- and C-terminal domains retain their conformational independence, remaining largely separated by the central helix and linker region (Figure 2.2B). This contrasts X-ray crystallography studies involving CaM and TFP, in which the antagonist was shown to cause significant conformational change in CaM.[58,59] In this instance, TFP appears to induce significant bending of the flexible central linker region in addition to small changes in the N- and C-terminal domains. The difference seen between these two compounds is perhaps reflective of the stark contrast in their respective affinities (K_d = 10 μM vs. K_d > 1 mM for TFP and AMK respectively), however a similarly unchanged overall conformation is seen with antagonists such as W-7, which binds to CaM with the same affinity as TFP.[122,123] The 2:1 W-7-CaM solution structures display relative mobility of the globular domains, with one ligand per domain buried in the hydrophobic cavities. As structures involving TFP have broadly been carried out using X-ray diffraction, complexation

with W-7 using solution-state NMR is perhaps a more translatable comparison. Our findings are also congruous with those from measurements of interdomain NMR pseudocontact shifts and residual dipolar couplings induced my magnetic alignment in CaM bound to aMT where Ca^{2+} was partially replaced by paramagnetic Terbium (Tb^{3+}).[74] It was shown that the CaM-aMT complex also behaves as uncomplexed CaM, with the globular domain possessing orientational freedom from one another.[74]

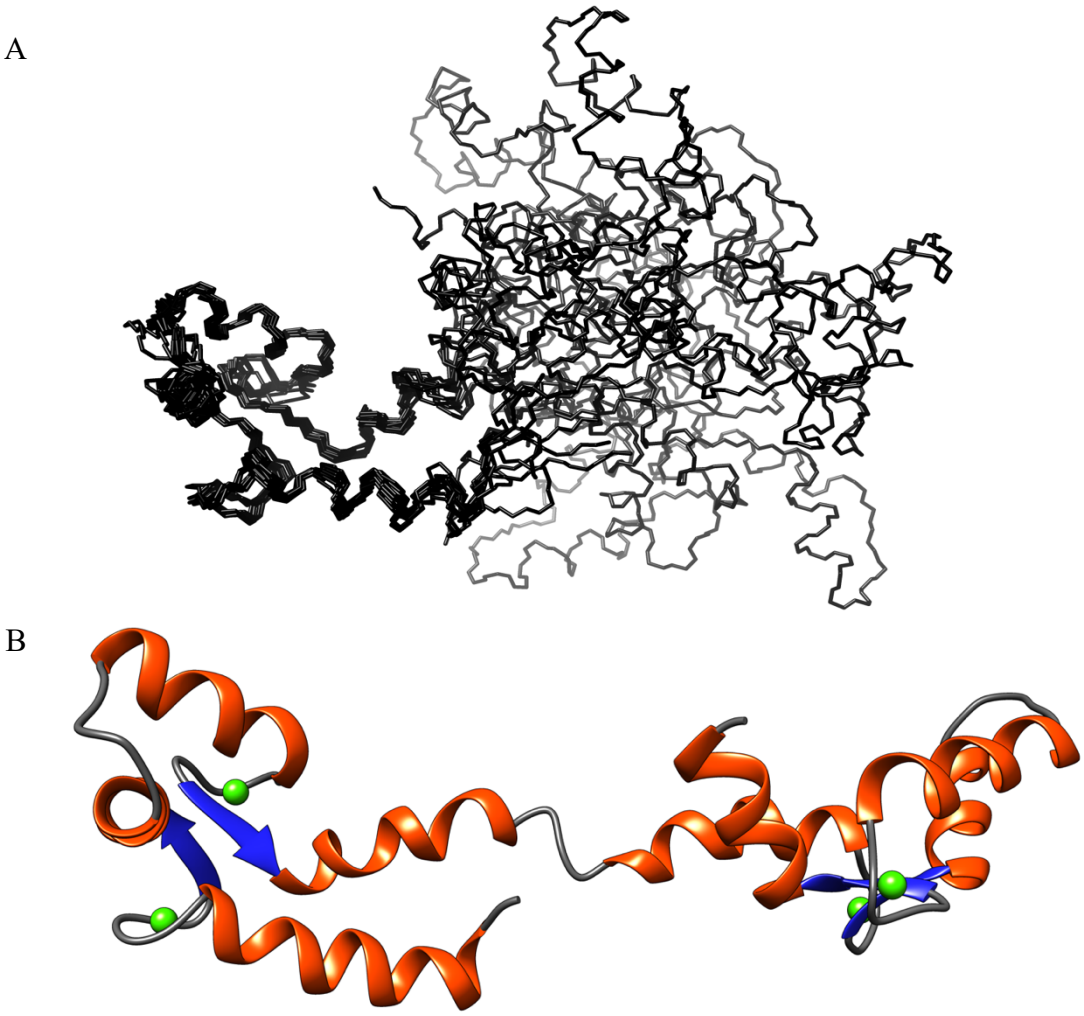

Figure 3.2 Structures of CaM when in complex with AMK.
(A) Backbone view of the superposition of the 10 lowest energy structures of CaM when bound to AMK. (B) Ribbon view of a the most likely structure of CaM when in complex with AMK coloured according to secondary structure. α-helices are shown in red, β-sheets in blue and random coil in grey. Ca^{2+} is represented by green spheres.

3.3.2 ^{15}N-HSQC NMR Titration

NMR spectroscopy was used to assess residue-specific changes in CaM structure upon binding to AMK. Increasing concentrations of AMK up to a 7-fold excess were titrated into 350 μM CaM and ^{15}N-HSQC spectra were acquired after each titration. Changes in structure were determined by monitoring changes in chemical shifts specific to each residue in CaM. NMR spectral changes for ^{15}N- ^{13}C-labelled CaM occurred in fast exchange on the NMR timescale, which produced signals with averaged chemical shifts for a given nucleus, rapidly exchanging between bound and unbound states. This indicates a weak interaction, in which k_{off} values are larger than the chemical shift difference between the free and bound form of the protein. As a result, the CaM-AMK complex is only stable for a short period of time. The superposition of ^{15}N-HSQC spectra at various molar ratios of CaM and AMK are shown in Figure 3.3A, which displays the gradual shift of NH peaks over the course of the titration.

Perturbation of ^{1}H and ^{15}N chemical shifts were normalized using the function $\Delta\delta_{norm}=\sqrt{((\Delta\delta_H)^2+(\Delta\delta_N \times 0.2)^2)}$, and the magnitude of these normalized values for each residue can be seen in Figure 3.3B. A threshold of 0.03 ppm was used in determining residues displaying significant changes in chemical shifts brought on by the titration of AMK. Approximately 28% of residues in CaM surpassed threshold values, similar to the 22% of residues showing significant change in another study with a 15N-HSQC titration involving aMT and CaM, although their criteria for a significant change is not clearly stated.[74] A comparison of the two titrations reveals similarities in the impact on structure of AMK and aMT, with the majority of significant changes being localized to the hydrophobic pockets in globular domains of CaM. Many of the most affected residues are also those shown to interact most strongly with the antagonist W-7, which inhibits target binding by reducing available hydrophobic surface area.[122]

A

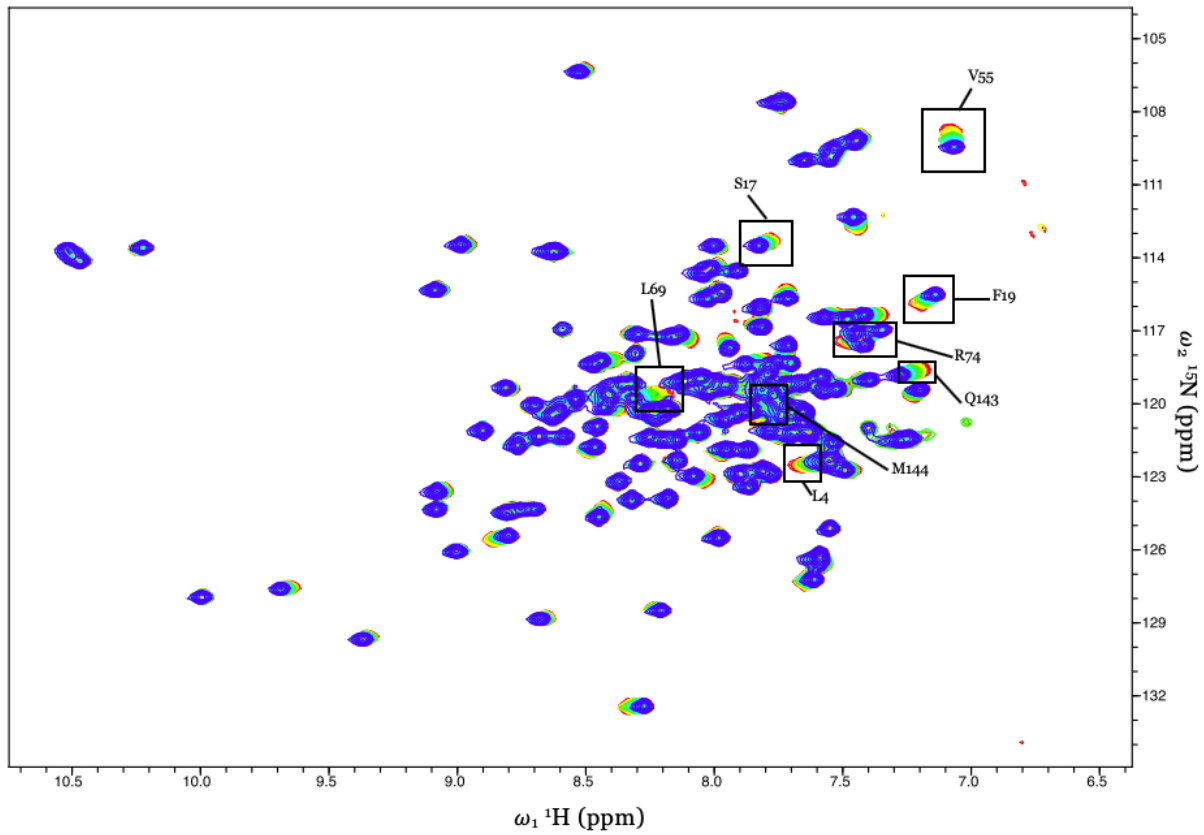

B

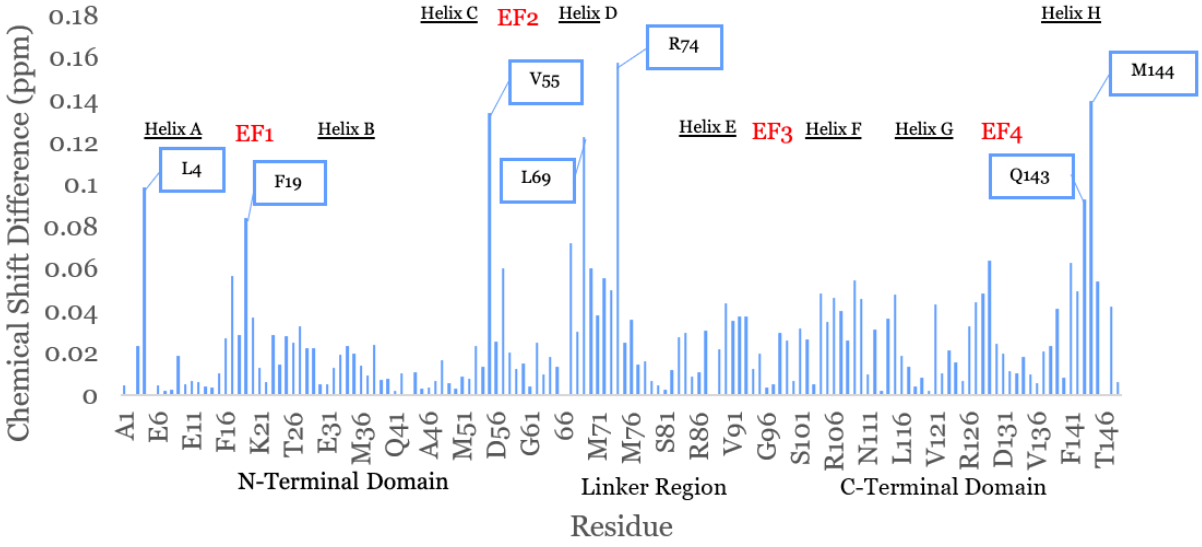

Figure 3.3 ^{15}N-HSQC titration spectral overlay and chemical shift changes.
(A) ^{15}N-HSQC spectra over the course of titration ranging from 0 equivalents (red) to 7 equivalents (blue) of AMK. (B) Normalized magnitudes of chemical shift perturbations. The largest changes were localized to the hydrophobic cavities of CaM.

61 % of large shift changes were observed in the C-terminal domain, although N-terminal shifts changes were notably larger in magnitude. The collective perturbations are widespread throughout the entirety of the sequence, suggesting that AMK likely scavenges the surface of the protein at multiple sites while forming fleeting contacts in the process.

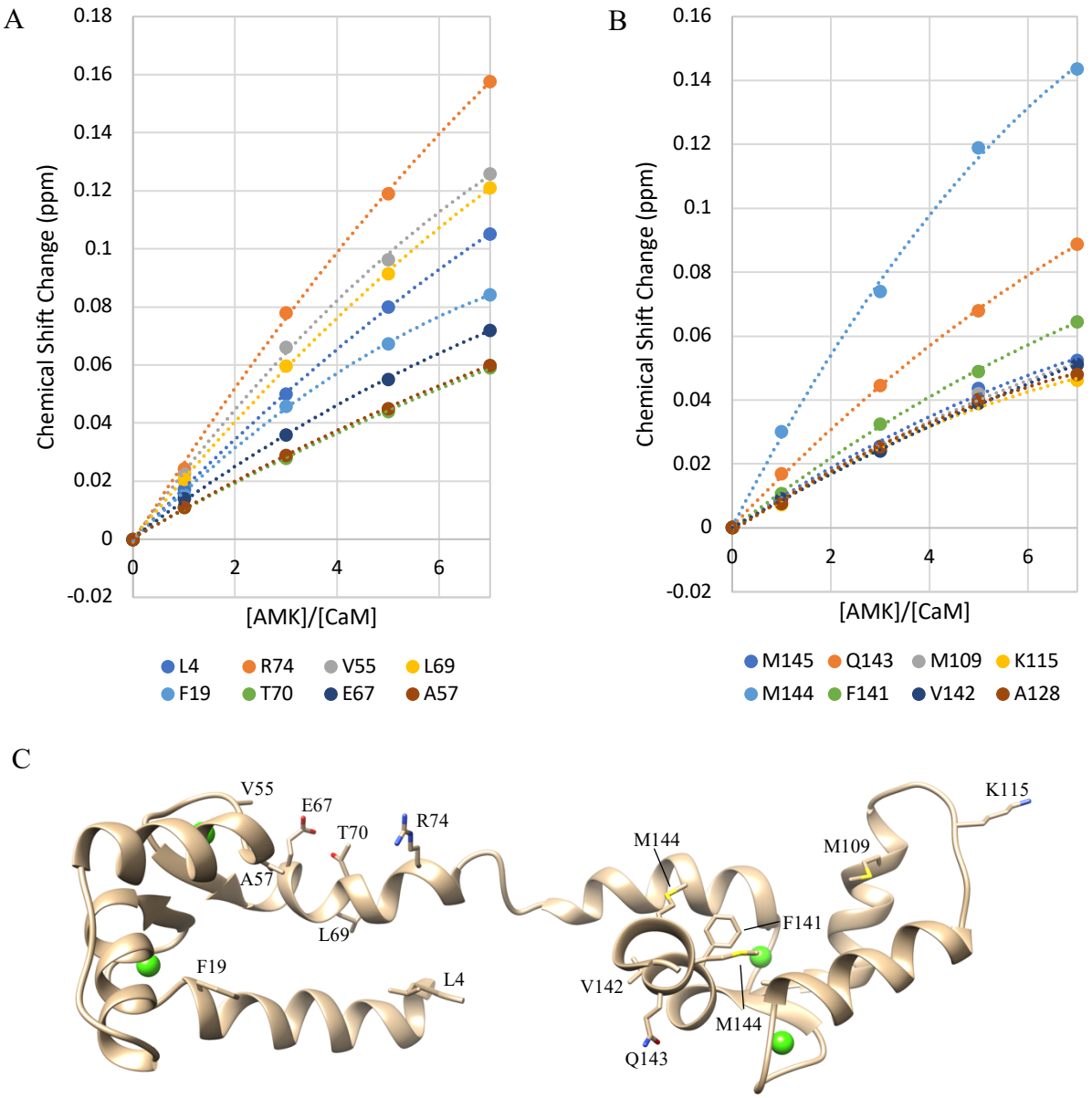

Figure 3.4 ^{15}N-HSQC titration curves of residues with largest chemical shift changes. ^{15}N-HSQC titration curves for the residues exhibiting the largest changes in the (A) N- and (B) C-terminal domains. (C) Location of the representative residues within the solution structure of CaM when bound to AMK. CaM backbone and sidechains are shown in beige, sulfur in yellow, nitrogen in blue and oxygen in red. Ca^{2+} is depicted as green spheres.

Analysis of binding curves generated from the normalized changes in chemical shifts relative to the initial spectrum show no saturation is achieved (Figure 3.4), similar to what was seen in various biophysical analyses described in Chapter 2. A total of 8 residues exhibiting the largest unambiguous chemical shift perturbation from each globular domain were selected for non-linear least-squares fitting using a saturation/growth model to predict K_d values. Every representative residue displayed K_d values in the millimolar range, similar to other NMR titrations involving aMT.[73,74] Independent fitting suggests that the N-terminal binds with similar, albeit marginally higher affinity than the C-terminal domain (K_d = 2.94 mM vs. 3.35 mM respectively) (Table 3.1, Table 3.2). These values denote a 2-4 mM decrease from those determined by Turjanksi *et al*, although this difference is potentially within the margins of error or the result of variation in fitting protocol.[74]

Table 3.1 Estimation of N-terminal domain K_d from ^{1}H and ^{15}N chemical shifts

N-Terminal Residues	K_d (mM)	Error (mM)	Initial ^{1}H Chemical Shift (ppm)	Initial ^{15}N Chemical Shift (ppm)	Final ^{1}H Chemical Shift (ppm)	Final ^{15}N Chemical Shift (ppm)
L4	2.78	±0.5	7.66	122.534	7.561	122.358
F19	3.24	±0.7	7.193	115.834	7.139	115.511
V55	3.00	±0.2	7.08	108.822	7.067	109.448
A57	2.91	±0.4	8.333	132.451	8.273	132.451
E67	3.07	±0.7	7.807	118.327	7.879	118.327
L69	2.86	±0.2	8.202	119.596	8.317	119.786
T70	2.81	±0.3	7.358	116.333	7.417	116.333
R74	2.82	±0.5	7.472	117.459	7.348	116.972
Average	2.94	±0.4				

*error values were determined by the fitting program for a given fit and do not necessarily reflect precise margins of error in K_d itself.

Table 3.2 Estimation of C-terminal domain K_d from ^{1}H and ^{15}N chemical shifts

C-terminal Residues	K_d (mM)	Error (mM)	Initial ^{1}H Chemical Shift (ppm)	Initial ^{15}N Chemical Shift (ppm)	Final ^{1}H Chemical Shift (ppm)	Final ^{15}N Chemical Shift (ppm)
M109	2.94	±0.6	8.095	117.33	8.136	117.179
K115	4.82	±0.4	8.435	124.418	8.449	124.638
A128	4.69	±0.3	7.222	119.633	7.199	119.426
F141	2.90	±0.5	8.859	125.586	8.801	125.445
V142	2.86	±0.5	8.38	120.131	8.431	120.131
Q143	2.98	±0.2	7.197	118.612	7.274	118.833
M144	2.87	±0.5	7.844	120.505	7.729	120.075
M145	2.76	±0.7	7.718	115.398	7.561	115.658
Average	3.35	±0.5				

*error values were determined by the fitting program for a given fit and do not necessarily reflect precise margins of error in K_d itself.

^{15}N-HSQC NMR experiments were also conducted to see whether AMK had an observable impact on the chemical shifts of CaM when bound to the CaM-binding domain peptide of nNOS. AMK was titrated into sample containing CaM until a 7:1 AMK:CaM ratio was achieved, and the spectrum was recorded. nNOS peptide was then titrated into the sample and spectra were recorded until no further changes in chemical shifts occurred. This was compared to a ^{15}N-HSQC spectrum with no AMK present. Slow exchange on the NMR timescale was observed, consistent with the nanomolar range affinity between CaM and the peptide. The overlay of CaM-nNOS peptide ^{15}N-HSQC spectra can be seen in Figure 3.5. Empirical analysis shows no change in backbone chemical shifts when CaM is first bound to AMK, indicating that the ligand is likely ejected from CaM when nNOS is present in stoichiometric quantities.

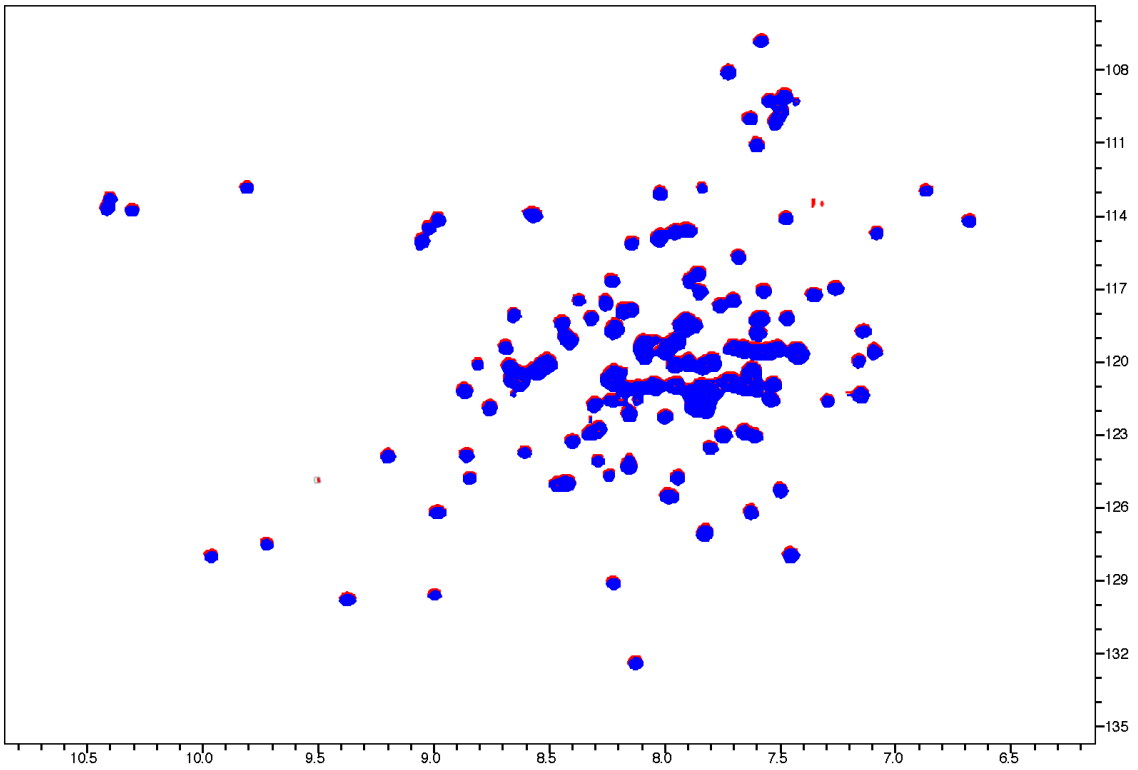

Figure 3.5 Impact of AMK on the CaM-nNOS ^{15}N-HSQC spectrum.
^{15}N-HSQC spectral overlay for CaM bound to nNOS in the absence (red) and presence (blue) of 7 molar equivalents of AMK. No changes in chemical shifts were observed.

3.4 Conclusions

This is the first study to use multidimensional NMR to provide structural details of the interaction between CaM and AMK. No major changes in the overall architecture of CaM and the absence of intermolecular NOEs yet again points to a weak interaction. ^{15}N-HSQC NMR titrations proved to be effective in providing the qualitative and quantitative analytical framework necessary for such a system. An approximate affinity was determined to be in the low millimolar range, as suggested by studies involving aMT, and the chemical shift perturbations show similar likely binding surfaces between the two compounds. The prevalence of these perturbations throughout the sequence of CaM suggests that AMK associates *via* transient

contacts formed at several locations, although primarily within the exposed hydrophobic cavities of the protein. The overall conformation of CaM when bound to AMK and the likely binding surfaces indicate that AMK occupies similar sites as W-7. This information not only provides new insight into the potential mechanism of antagonism but validates certain NMR techniques as means to appraise low affinity protein-ligand systems.

Chapter 4
Molecular Dynamics Simulations of AMK-CaM-nNOS Peptide Interactions

4.1 Introduction

While crystallographic and NMR studies are highly valuable in the study of protein-ligand interactions, they face numerous restrictions that reduce their effectiveness. Aside from the detraction of being labour intensive, they are limited in their capacity for acquisition of structural information for weakly interacting systems.[124] Such systems often do not crystallize or if so, not in a biologically relevant conformation. NMR methods using NOE constraints for assignment are equally often equally ineffective, with the widely accepted threshold for such a technique to work being approximately K_d = 10 μM.[74] Computational techniques to predict protein binding offer an appealing alternative. Molecular dynamics (MD) simulations represent one such alternative, using simple Newtonian physics to approximate quantum mechanical motions and the biochemical reactions of large systems.[125]

Biophysical analyses and NMR work from the present study strongly suggests a very weak interaction between CaM and AMK (K_d > 1 mM) and thus computational techniques were used for a more considered examination of binding. Similar MD simulations with aMT, AMK's structurally similar parent compound, and CaM have been conducted to good effect although the scope of the study was limited to only the C-terminal domain.[74] Our study builds upon this work, using MD simulations to provide hitherto unknown information regarding interactions between CaM, AMK and the CaM-binding domain peptide of nNOS.

4.2 Methods and Experiments

4.2.1 Molecular Docking Simulations

Predicted docking sites and orientations for AMK when in stable complex with CaM were determined using AutoDock Vina in parallel with AutoDock Tools.[126] CaM and AMK structures (PDB 3CLN and PubChem CID 390658 respectively) were prepared in USCF Chimera with solvent removed to ensure accurate calculations.[127] All hydrogens were added in AutoDock Tools and the entire protein was selected for docking analysis. AutoDockVina generated 20 of the most favourable poses according to a scoring function based on free energies of binding. The most favourable structures were selected for future use in MD simulations. The same protocol was used for docking simulations involving the nNOS peptide and AMK. Docking simulations involving AMK and the CaM-nNOS peptide complex were carried out using PDB 2O60 for the complex.

4.2.2 Molecular Dynamics Simulations

Visual Molecular Dynamics (VMD) was used to generate the protein structure files (PSF) with the Automatic PSF Builder plugin.[128] The PSF files contain all of the molecule-specific information necessary for the application of the CHARMM force field to the molecular systems.[84] All complexes were solvated in a cubic water box with an edge length of 80 Å using the Solvate plugin and ionized with 0.15 M $CaCl_2$ with the Autoionize plugin. VMD was further used in the visualization of coordinate trajectories following simulations. Topology and parameter files for AMK in each pose were created using SwissParam.[129] Biomolecular MD simulations were conducted using the Nanoscale Molecular Dynamics (NAMD) software package via the Graham computing cluster in association with Compute Canada.[130]

The lowest energy poses of AMK bound to CaM from AutoDock Vina were used as initial coordinates for a 10 ns minimization and equilibration at 310 K. The extent to which the system had equilibrated was verified with RMSD before carrying out a 20 ns production run. Coordinates were recorded every picosecond and a 1 Å grid spacing was used. The same protocol was used for AMK-nNOS peptide and AMK-CaM-nNOS studies.

4.3 Results and Discussion

4.3.1 Molecular Docking Simulations

4.3.1.1 CaM-AMK Docking Simulations

AutoDock Vina generated the 20 most favourable CaM-AMK poses according to docking scores based on free energy of binding (Table 4.1). Docking simulations were repeated three times to ensure consistent solutions. The scores for each respective pose ranged from -4.4 kcal/mol to -3.5 kcal/mol. The seven most favourable poses were largely consistent, varying only by 0.2 kcal/mol. The spatial coordinates, however, varied greatly across all 20 models with best mode RMSD (upper bound) differing by as much as 47.472 Å from model 1. The 20 poses could be sorted into one of six different approximate docking sites (Figure 4.1). The distribution of models among the 6 sites are seen in Table 4.2. Four of the sites are located in the N-terminal domain and two in the C-terminal domain. At sites one and six, AMK is nestled in the hydrophobic cavity of the N- and C-terminal domains, proximal to the methionine residues that constitute nearly half of CaM's hydrophobic surface area (Figure 4.2A,B).[16] Sites two, three and five are characterized by hydrophobic contacts near the edge of the cavity and polar interactions with the hydrophilic, negatively charged glutamate and aspartate clusters

within in the globular domains (Figure 4.2C). These polar interactions are predominant at site four (Figure 4.2D).

Table 4.1 Scoring for 20 highest affinity AutoDock Vina-generated CaM-AMK models.

MODEL	AFFINITY (KCAL/MOL)	DISTANCE FROM RMSD L.B	BEST MODE RMSD U.B
1	-4.4	0.000	0.000
2	-4.3	12.862	14.620
3	-4.3	36.213	37.771
4	-4.3	35.359	37.191
5	-4.2	15.025	16.369
6	-4.2	37.438	39.151
7	-4.2	3.442	4.942
8	-4.1	37.361	38.952
9	-4.1	46.284	47.961
10	-4.0	35.963	37.701
11	-4.0	38.271	39.771
12	-4.0	45.778	47.472
13	-3.9	19.211	21.271
14	-3.9	15.398	16.729
15	-3.7	13.680	15.011
16	-3.7	16.037	17.742
17	-3.7	19.565	21.611
18	-3.6	15.062	16.376
19	-3.6	19.345	21.225
20	-3.5	18.681	20.562

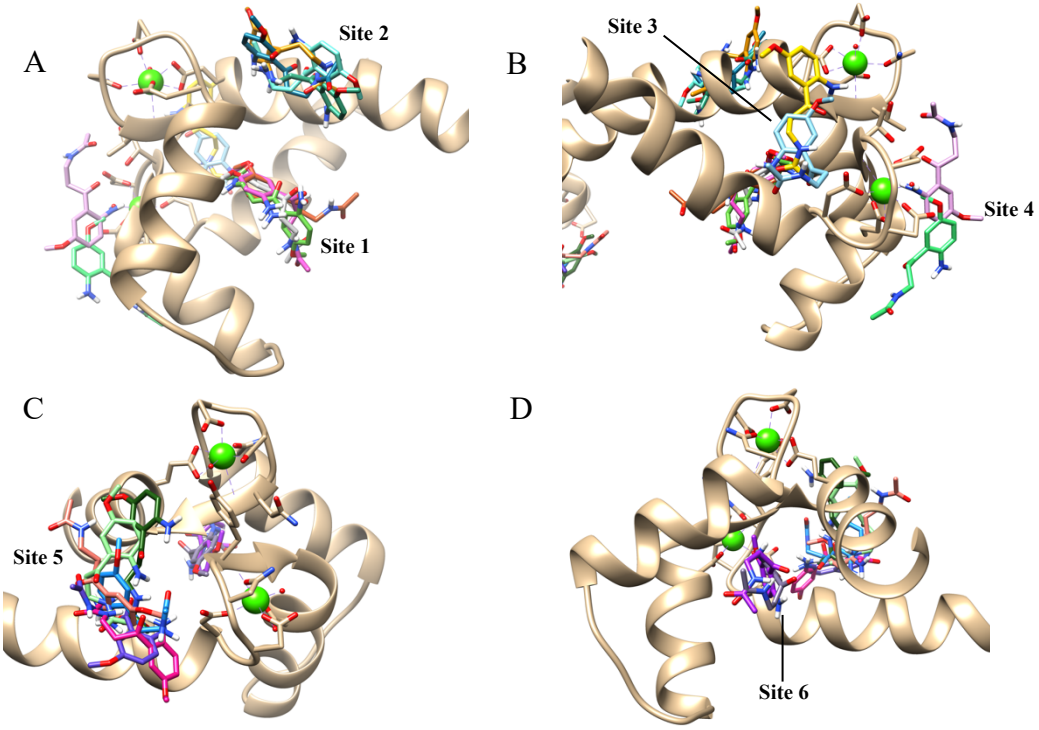

Figure 4.1 20 highest affinity docking poses of AMK bound to CaM generated by AutoDock Vina.
(A) Proximal view of the N-terminal domain displaying docking sites 1 and 2. (B) Distal view on the N-terminal domain showing docking sites 3 and 4. (C) Proximal view of the C-terminal domain showing docking site 5. (D) The distal view of the C-terminal domain displaying docking site 6. CaM is shown in beige, Ca^{2+} ions as green spheres and polychromatic AMK molecules are shown with each colour corresponding to a unique pose. Figures were prepared using UCSF Chimera v. 1.13.1.

Table 4.2 Distribution of 20 highest affinity models from AutoDock Vina across 6 identified docking sites.

Docking site 1	Docking Site 2	Docking Site 3	Docking Site 4	Docking site 5	Docking Site 6
Model 5 Model 14 Model 16 Model 18	Model 13 Model 17 Model 19 Model 20	Model 1 Model 7	Model 2 Model 15	Model 3 Model 4 Model 6 Model 8 Model 10 Model 11	Model 9 Model 12

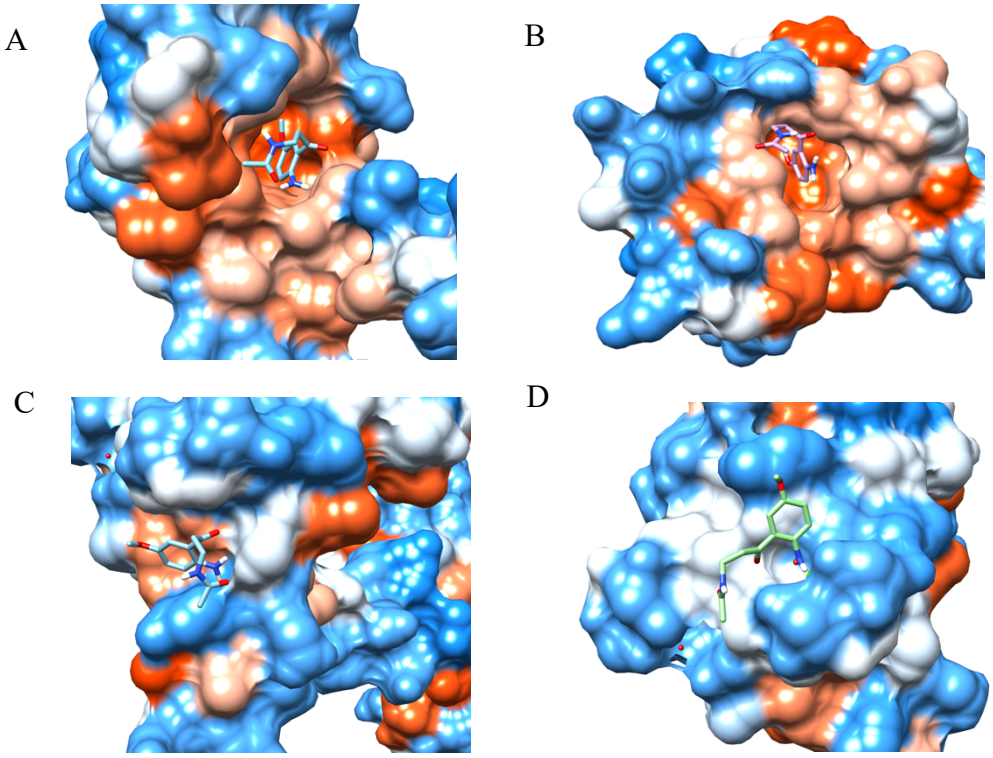

Figure 4.2 Hydrophobicity surface mapping of CaM near predicted AMK binding sites. Kyte-Doolittle hydrophobicity surface mapping of CaM near (A) model 5, (B) model 9, (C) model 1 and (D) model 2 poses. These correspond to binding sites 1, 6, 3 and 4 respectively. Blue corresponds to most hydrophobic and red to most hydrophilic. Figures were prepared using UCSF Chimera v. 1.13.1.

4.3.1.2 AMK-nNOS Docking Simulations

A similar docking procedure as described in the case of CaM-AMK complexation was carried out in order to further analyze any interactions that may occur between AMK and the CaM-binding domain peptide of nNOS. The highest affinity poses for each isoform are shown in

Figure 4.3. The affinities ranged from -5.1 kcal/mol to -3.7 kcal/mol (Table 4.3), and spatial coordinates of the poses were highly consistent. Two docking locations were identified for nNOS, with almost all of the more likely poses occurring with the phenyl moiety close to the hydrophobic residue F16 and polar contacts forming between AMK and E12. Model 1 (the most energetically favourable pose) was selected for future MD simulation studies.

Table 4.3 Scoring for 20 highest affinity AutoDock Vina-generated nNOS-AMK models.

MODEL	AFFINITY (KCAL/MOL)	DITANCE FROM RMSD L.B	BEST MODE RMSD U.B
1	-5.1	0.000	0.000
2	-4.9	1.848	12.479
3	-4.8	2.602	12.681
4	-4.5	2.244	5.756
5	-4.5	2.818	11.681
6	-4.4	2.282	12.787
7	-4.4	2.684	11.448
8	-4.4	2.739	3.964
9	-4.3	2.416	6.464
10	-4.3	9.629	14.024
11	-4.2	3.332	13.885
12	-4.1	1.774	14.860
13	-4.1	2.546	12.501
14	-4.0	1.853	3.562
15	-4.0	9.945	11.410
16	-3.9	9.943	6.324
17	-3.9	9.481	12.733
18	-3.8	9.610	11.602
19	-3.8	2.734	11.815
20	-3.7	3.654	12.717

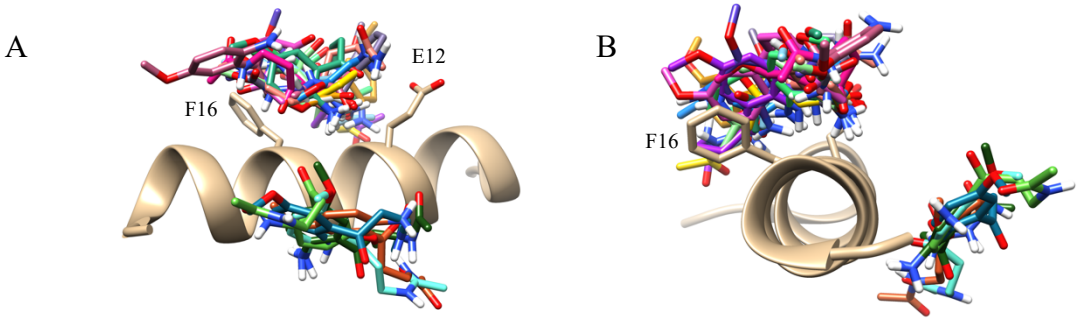

Figure 4.3 20 highest affinity docking poses of AMK bound to the nNOS peptide generated by AutoDock Vina.
(A) side view and (B) frontal view of the the 20 most favourable AMK poses with nNOS peptide. The peptide is shown in beige, oxygens in red, hydrogens in white, nitrogens in blue and polychromatic AMK molecules are shown with each colour corresponding to a unique pose. Figures were prepared using UCSF Chimera v. 1.13.1.

4.3.1.3 AMK-CaM-nNOS Docking Simulations

A final set of docking simulations were carried out to identify the likely docking sites of AMK on a CaM-nNOS peptide complex. Most of the 20 poses generated were localized at the point where the N- and C-terminals meet, having wrapped around the peptide (Figure 4.4). In this conformation, AMK is coordinated by hydrogen bonds with a cluster of lysine residues and a glutamate in the nNOS peptide. Proximal methionine residues (M72, M76, M145) in CaM contribute to hydrophobic coordination of AMK in this pose.

Table 4.4 Scoring for 20 highest affinity AutoDock Vina-generated AMK-CaM-nNOS models.

MODEL	AFFINITY (KCAL/MOL)	DITANCE FROM RMSD L.B	BEST MODE RMSD U.B
1	-5.1	0.000	0.000
2	-5.1	18.386	19.649
3	-5.0	2.291	6.056
4	-5.0	3.695	7.674
5	-4.9	2.562	3.450
6	-4.9	17.814	20.018
7	-4.9	1.696	1.952
8	-4.8	2.675	4.190
9	-4.8	2.723	4.285
10	-4.8	3.372	4.767
11	-4.7	3.447	5.286
12	-4.6	2.461	3.336
13	-4.5	2.204	5.486
14	-4.5	17.321	18.942
15	-4.5	21.729	23.367
16	-4.5	16.144	17.809
17	-4,4	11.123	12.067
18	-4.4	18.637	19.562
19	-4.3	18.252	20.836
20	-4.3	17.246	18.723

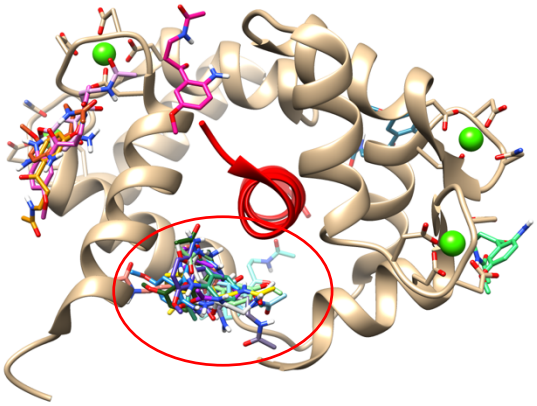

Figure 4.4 20 highest affinity docking poses of AMK bound to the CaM-nNOS peptide complex generated by AutoDock Vina.
The 20 most favourable AMK poses with the CaM-nNOS peptide complex. The peptide is shown in red and CaM in beige with oxygens in red, hydrogens in white, nitrogens in blue and polychromatic AMK molecules are shown with each colour corresponding to a unique pose. The most favourable poses are typically found in the region circled in red. Figures were prepared using UCSF Chimera v. 1.13.1.

4.3.2 Molecular Dynamics Simulations

4.3.2.1 Molecular Dynamics Simulations of CaM-AMK Complexation

Poses of AMK bound to CaM from AutoDock Vina were selected for NAMD simulations according to affinity scores and concurrence with ^{15}N-HSQC NMR titration data described in Chapter 3. A 10 ns minimization and equilibration of the highest affinity CaM-AMK pose (model 1) was conducted first and the RMSD of the backbone α-carbon atoms showed a reasonably equilibrated system (Figure 4.5A). The distance from the methoxy oxygen (O1) and the amine nitrogen (N2) from the phenyl moiety in AMK to the α-carbons of I63 and F19 of CaM was used as a geometrical parameter to structurally characterize the MD simulation (Figure 4.5B). These two residues were chosen as they straddle the approximate center point of the N-terminal hydrophobic cavity and their position changes very little over the course of the simulation.

A

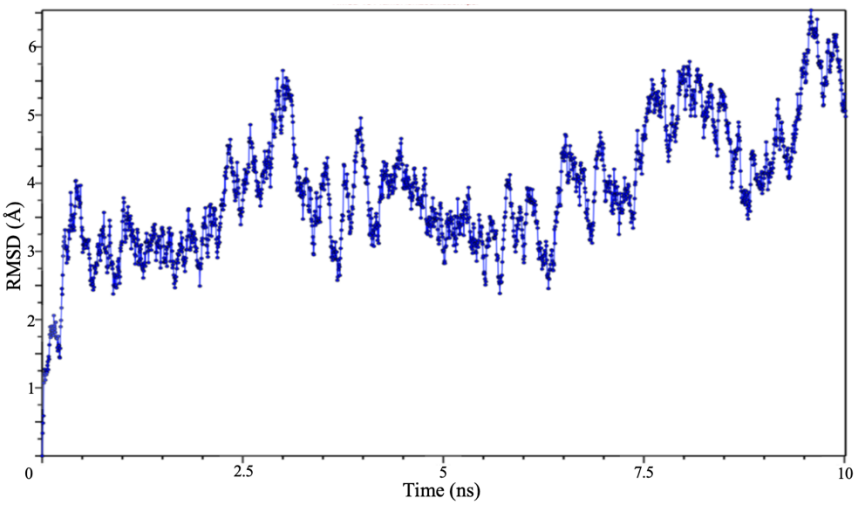

B

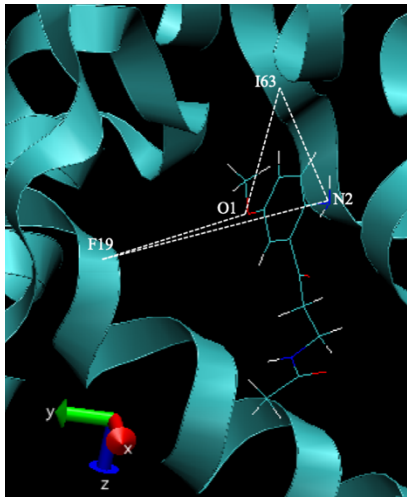

Figure 4.5 RMSD of CaM-AMK MD simulations and geometrical parameterization of trajectories.
(A) RMSD of a 10 ns minimization and equilibration with model 1 used to generate starting coordinates. (B) The distances from O1 and N2 to F19 and I63 used to characterize simulations are shown in VMD.

During the first 3.2 ns of equilibration, AMK begins migrating from its starting position near the loop segment of EF hand 1 on the outside of the hydrophobic cavity down towards L4. During this period, the antagonist shifts away from the bottom of the cavity by as much as 20 Å (Figure 4.6A). Following this, AMK appears to wedge between the helical segment of EF hand 1 and the helical region preceding the flexible linker region (Figure 4.6B). AMK then gradually settles into the hydrophobic cavity where it stays for the remainder of the equilibration.

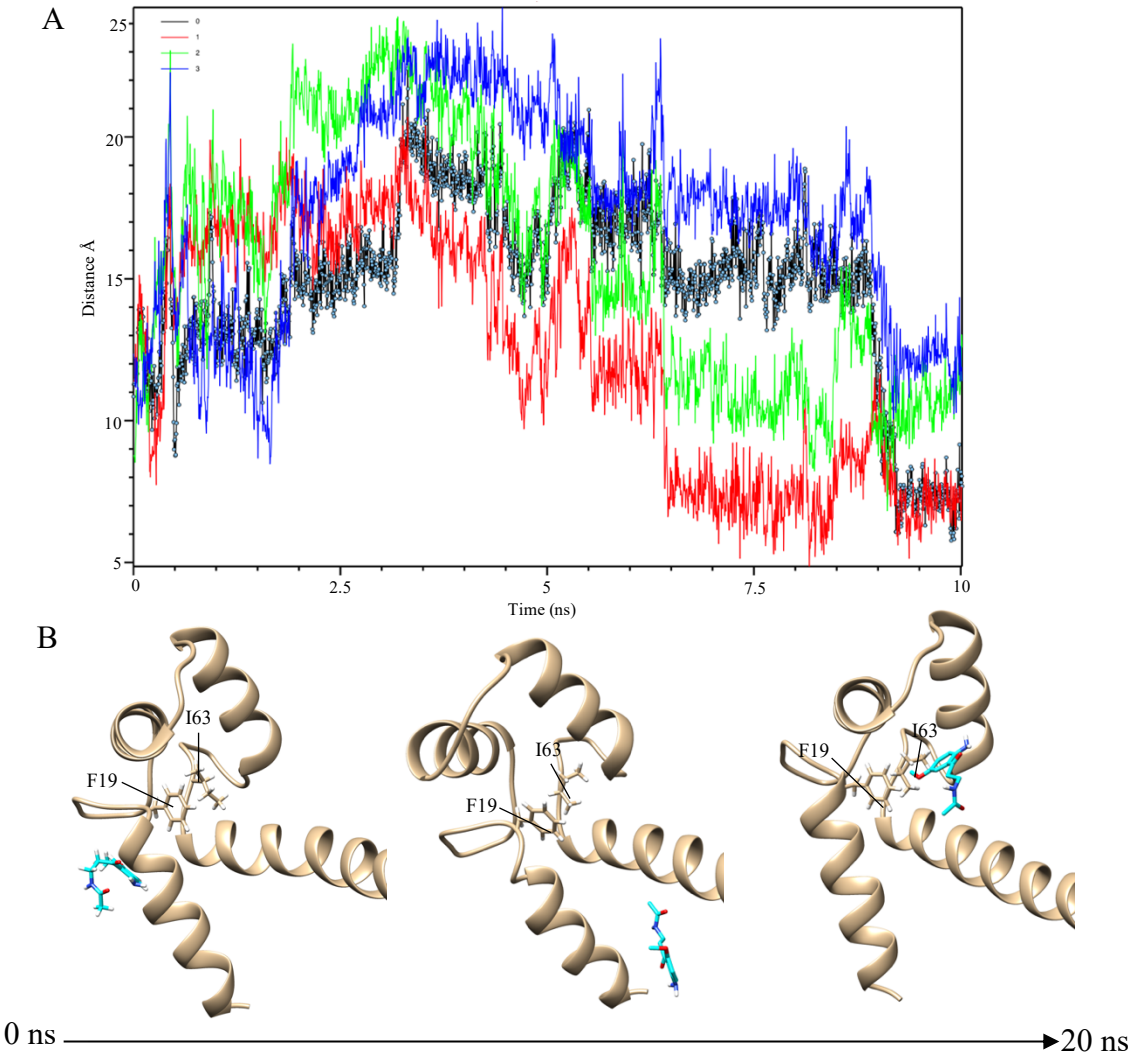

Figure 4.6 Model 1 minimization and equilibrium MD trajectory.
(A) The change in distance between Cα of I63 and O1 of AMK (black), Cα of F19 and O1 of AMK (red), Cα of F19 and N2 of AMK (green) and Cα of I63 and N2 of AMK (blue). (B) Progression of the 10 ns equilibration with the starting pose seen in the first panel, midpoint in the second panel and the final conformation in the third. CaM is shown in beige and AMK in cyan. Oxygens are shown in red, hydrogens in white and nitrogens in blue. Structures were prepared using UCSF Chimera v. 1.13.1.

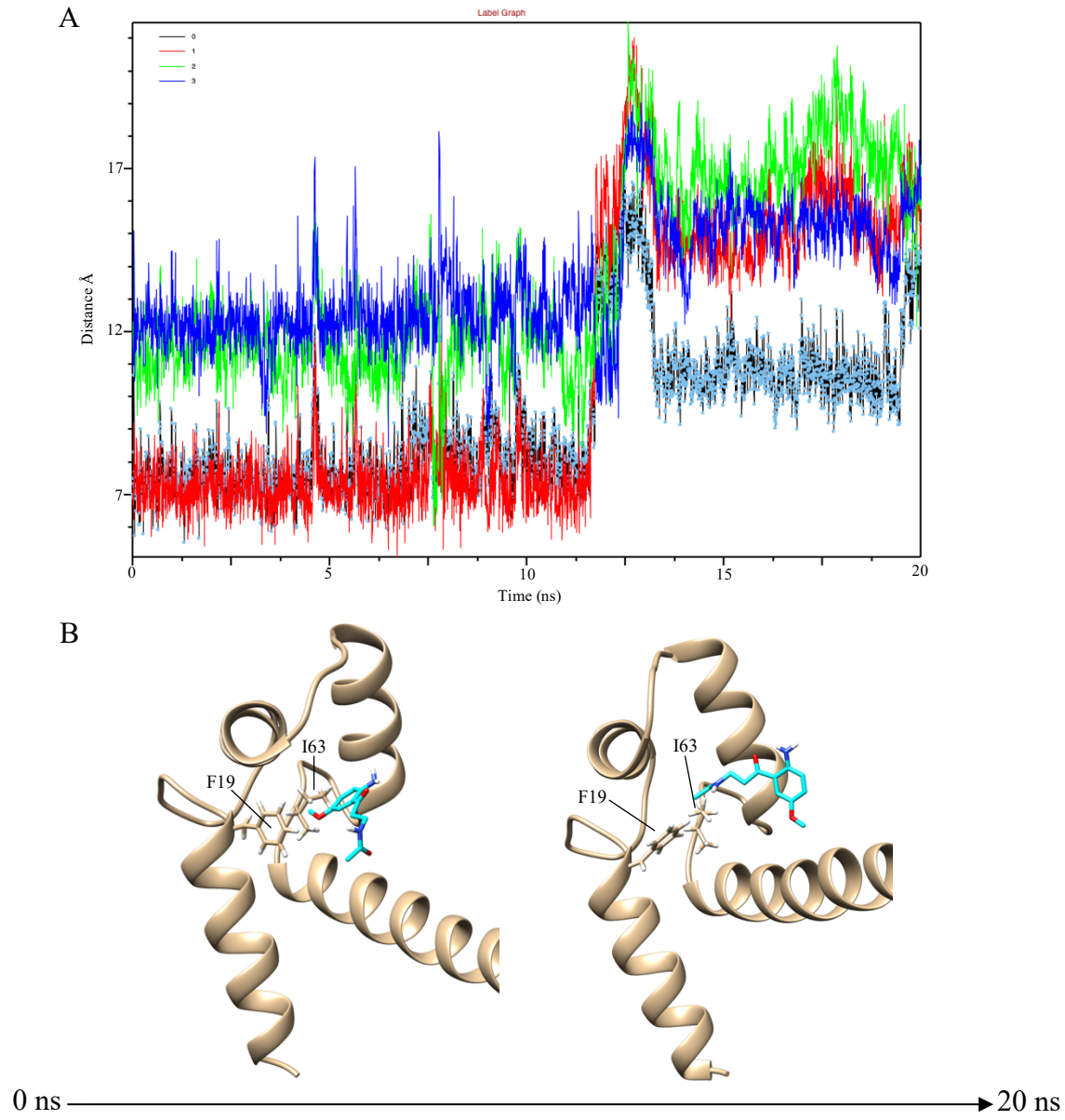

Figure 4.7 Model 1 production MD trajectory.
(A) The change in distance between Cα of I63 and O1 of AMK (black), Cα of F19 and O1 of AMK (red), Cα of F19 and N2 of AMK (green) and Cα of I63 and N2 of AMK (blue). (B) Progression of the 20 ns production simulation with the predominant conformation of the first part of the trajectory seen in the first panel, and the predominant conformation adopted in the latter portion of the simulation shown in the second panel. Structures were prepared using UCSF Chimera v. 1.13.1.

During the 20 ns production simulation with periodic boundary conditions, AMK remained entirely within the N-terminal cavity throughout. The initial orientation of AMK was maintained for the first 12.6 ns, after which it was rotated such that the phenyl moiety was angled more towards the central helical region (Figure 4.7B) The mobile nature of the interaction makes it difficult to provide a definitive model for association, but residue-specific trends are indeed observed (Figure 4.8). The first conformation during the simulation is characterized by loose, non-specific hydrophobic interactions between AMK and residues such as L32, V55, M36, M51 and M71. A consistent aromatic-aromatic contact is also seen between the phenyl moiety and F19. It also appears that as AMK moves closer to the central helix, the acetyl moiety of AMK interacts with K75 *via* a hydrogen bond. The second part of the simulation is characterized by the proximity of the hydrophobic cavity to the extended chain of AMK. A π-cation interaction is fleetingly seen between K75 and the phenyl moiety. The nature of all of these contacts is highly transient.

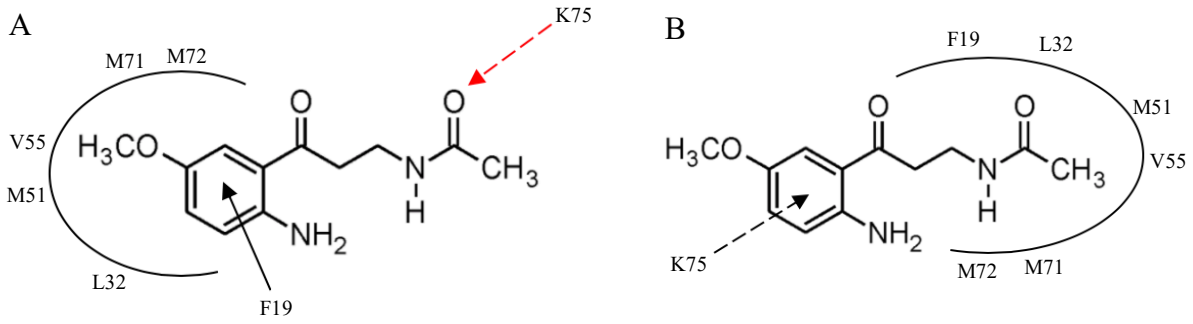

Figure 4.8 Model 1 protein-ligand contact analysis for CaM and AMK during the production MD simulation.
The expected formation of hydrophobic (———), electrostatic (-------) and hydrogen bond (-------) contacts between CaM and AMK during the initial (A) and concluding (B) frames of the production MD trajectory produced with model 1 used to generate starting coordinates.

AMK's location over the course of the MD simulations are highly consistent with data from our previous 2D NMR titrations (Figure 4.9). Of the 8 residues that exhibited the largest AMK-mediated chemical shift perturbations in the N-terminal domain, residues F19 and particularly L4 were extremely close to AMK for large portions to the minimization simulation. Furthermore, Residues such as V55, A57 and E67, whose chemical shifts were greatly altered in NMR experiments, were proximal to AMK for almost the entirety of the production simulation. These findings strongly suggest that AMK interacts with the N-terminal domain through transient contacts within the N-terminal hydrophobic pocket in addition to locations towards the edge of this pocket between the N-terminal tail and the central helical region.

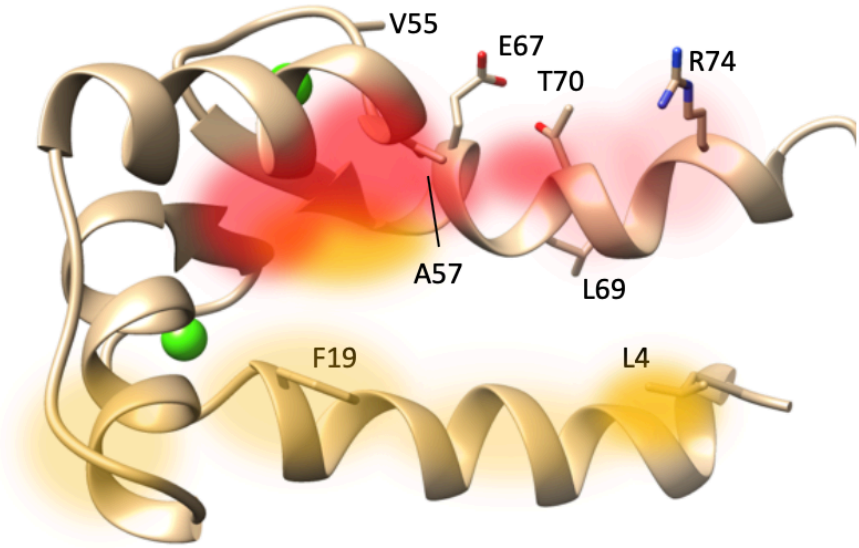

Figure 4.9 Heat map of AMK localization in the N-terminal domain over the course of minimization and production MD simulations.
The location of AMK in the N-terminal domain over the course of the MD minimization and production simulations are shown in orange and red respectively. The darker the colouring, the longer AMK has spent in a given location. The sidechains of 8 residues that displayed the greatest chemical shift perturbation the 2D NMR titrations are shown. CaM and sidechains are depicted in beige, oxygen in red, nitrogen in blue and calcium ions in green. The structure was prepared using UCSF Chimera v. 1.13.1.

Models 5 and 9 were similarly analyzed using MD simulations as they were within the hydrophobic cavities of the N- and C-terminal domains respectively and agreed with experimentally determined NMR data. During simulations beginning with the model 5 pose, AMK migrates towards to outer edges of the hydrophobic cavity where it remains throughout the production run, remaining relatively close to the reference residue F19 (Figure 4.9A). The ligand alternates from being wedged between the first helical segment of EF hand 1 and either the second helical region of the same EF hand, or the helical region preceding the central linker region. Although AMK did not dissociate, the interaction was far more dynamic than its N-terminal contemporary in model 1 and thus a static representation of binding is not feasible. Model 9-initiated simulations did not produce a stable binding mode. During equilibration, AMK exits the hydrophobic cavity and explores the protein surface. This is represented by the extreme fluctuations in O1 and N2 distances, with local maxima as high as 85 Å (Figure 4.9B). For C-terminal poses, the α-carbons I100 and V136 were selected as reference points. No other pose selected for MD analysis produced a plausible binding mode, with AMK completely dissociating from CaM altogether.

Regardless of the localization of the ligand during the simulations, no significant changes were seen in the overall architecture of CaM. N- and C-terminal domains maintain their orientational freedom, remaining completely separate throughout as seen in NMR structures of CaM when bound to AMK in Chapter 3 in addition to other studies involving aMT and W-7.[74,122]

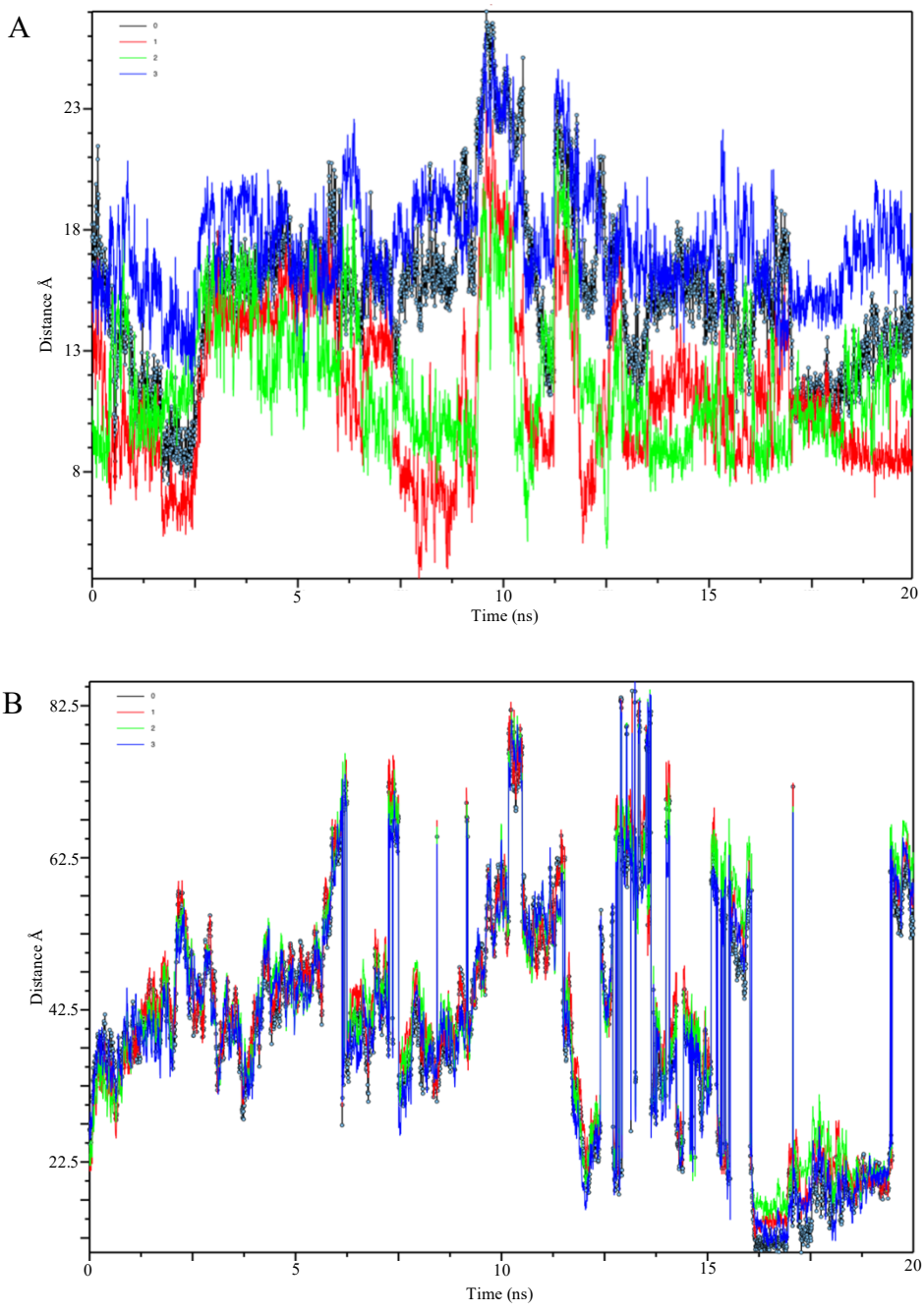

Figure 4.10 Model 5 and model 9 MD production trajectories.
(A) The change in distance between Cα of I63 and O1 of AMK (black), Cα of F19 and O1 of AMK (red), Cα of F19 and N2 of AMK (green) and Cα of I63 and N2 of AMK (blue) during the model 5 production simulation. (B) The change in distance between Cα of V136 and O1 of AMK (black), Cα of I100 and O1 of AMK (red), Cα of I100 and N2 of AMK (green) and Cα of V136 and N2 of AMK (blue) during the model 9 production simulation.

Weak association is further substantiated by the limited number of stable or near-stable binding modes. Only sites inside or in the immediate vicinity of the N-terminal hydrophobic cavity remained relatively close to their starting positions. This is in agreement with ^{15}N-HSQC titration data from the previous chapter which described a marginally higher affinity for the N-terminal domain, yet contrasts behaviour seen with antagonists such as TFP whose contacts with CaM are extensively biased towards the C-terminal domain.[59]

4.3.2.2 Molecular Dynamics Simulations of AMK-nNOS Peptide Complexation

20 ns simulations involving AMK and nNOS peptide did not show the formation of a stable complex. The ligand appears to scavenge the surface of the peptide until approximately 4.9 ns, at which point it no longer associates with nNOS and moves freely around the unit cell (Figure 4.10).

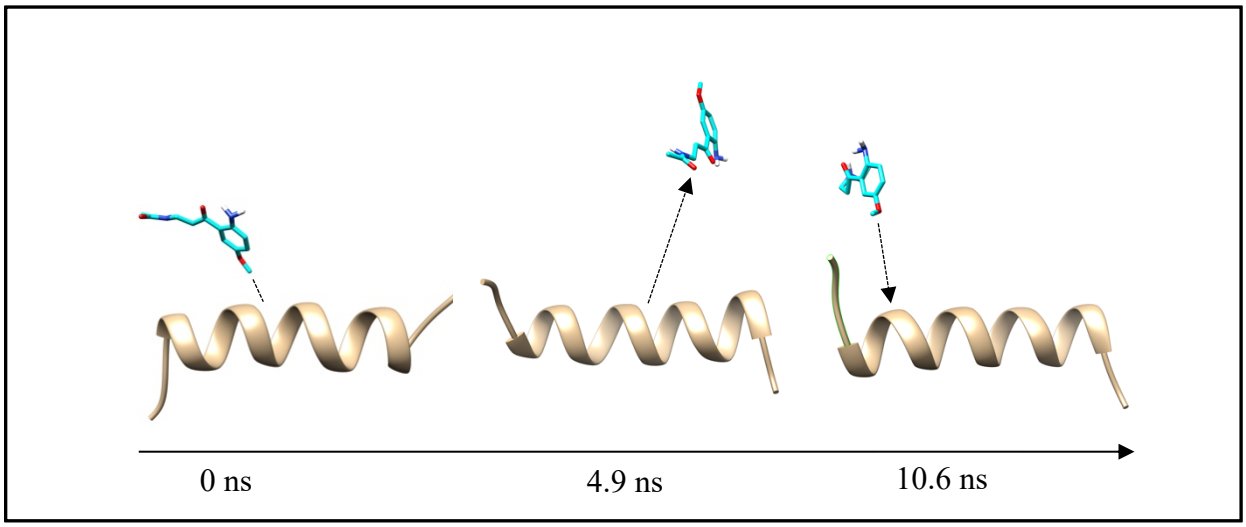

Figure 4.11 Visual CaM-nNOS MD trajectory.
The production MD trajectory of AMK and nNOS from the highest affinity docking pose. The initial position is seen in panel one, dissociation occurring at 4.9 ns is seen in panel two and AMK returns in close proximity to the peptide from 10.6 ns onward as seen in panel three. The peptide is shown in beige and AMK in cyan. Oxygens are shown in red, hydrogens in white and nitrogens in blue. The structures were prepared using USCF Chimera v 1.13.1.

After 10.6 ns, AMK again moves along the surface of the peptide, forming fleeting contacts along the way. Little can be inferred in terms of biological relevance from these results.

4.3.3.3 Molecular Dynamics Simulations of AMK-CaM-nNOS Peptide Complexation

MD simulations were carried out to approximate what allosteric binding of AMK to the CaM-nNOS peptide complex might look like. The model 1 (the most energetically favourable pose) docking pose was selected as the starting point for the simulation. The RMSD plot from the 10 ns minimization and equilibration showed a sufficiently minimized system for production simulations (Figure 4.12). Ove the course of the 10 ns, AMK migrated from between the ends to the N- and C-terminal domains towards the N-terminal. Here, it wedges itself between the first helical segment in the N-terminal domain and the central helical region (Figure 4.13).

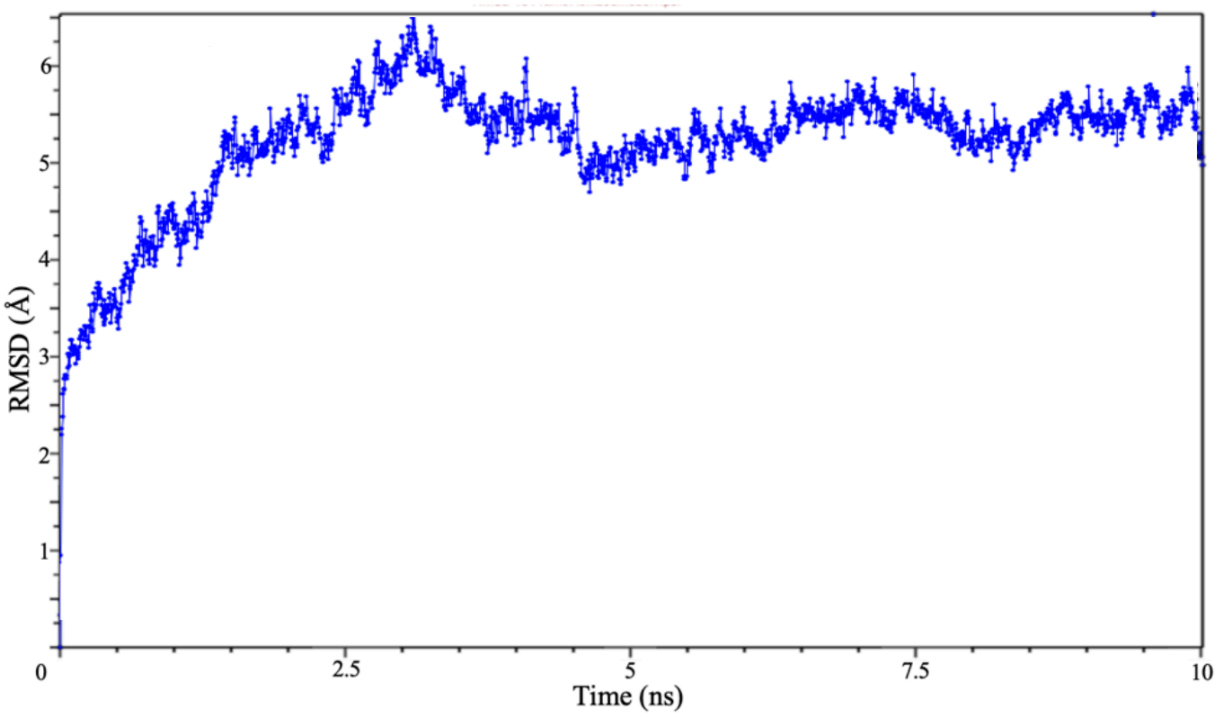

Figure 4.12 RMSD of AMK-CaM-nNOS minimization MD simulation.
RMSD of a 10 ns minimization and equilibration with model 1 used to generate starting coordinates showing suitable energy minimization.

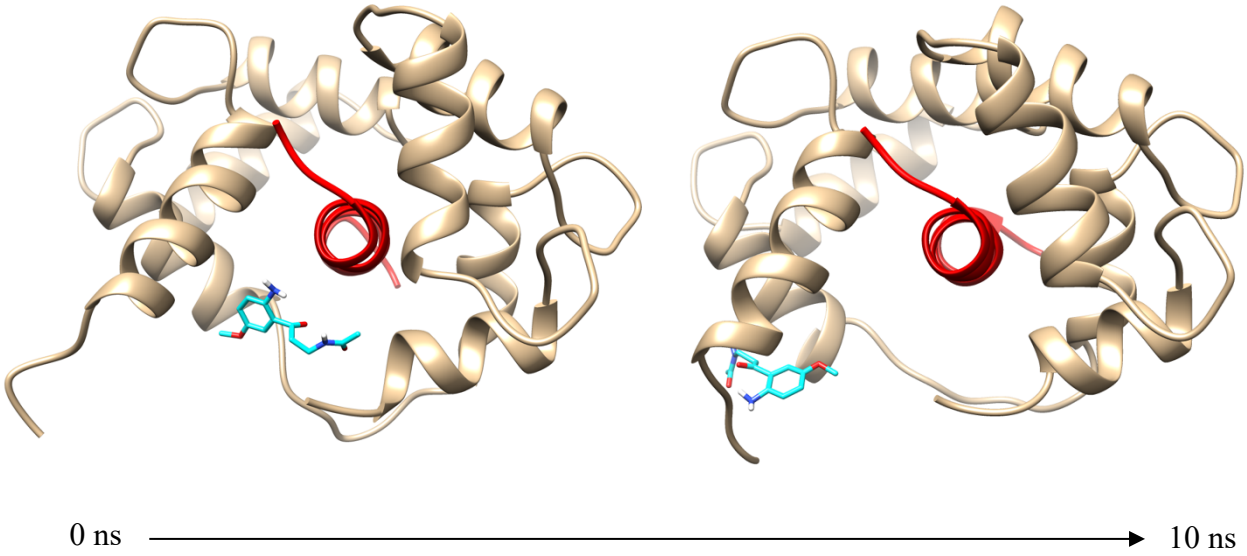

Figure 4.13 Visual AMK-CaM-nNOS minimization MD trajectory.
The minimization MD trajectory of AMK and the CaM-nNOS peptide complex from the highest affinity docking pose. CaM is shown in beige, the peptide is red and AMK in cyan. The structures were prepared using USCF Chimera v 1.13.1.

This position is not unlike that which AMK assumes during the model 1 CaM-AMK minimization simulation. The 20 ns production simulation saw little change in localization with respect to the final frame of the minimization run. The binding mode appears to be relatively stable, with AMK remaining firmly wedged between the N-terminal tail and the central linker region, near hydrophobic residues such as L4, F12, L4, L69 and M71 (Figure 4.14). In this position, the amine group near the phenyl moiety in AMK forms hydrogen bonds with backbones of nearby residues. Oxygen-containing segments of AMK also associate electrostatically with R74 in a highly transient manner. Many of these residues, particularly L4, L69 and R74, are the same residues that exhibited among the largest AMK-mediated chemical shift perturbations in our 2D NMR titrations.

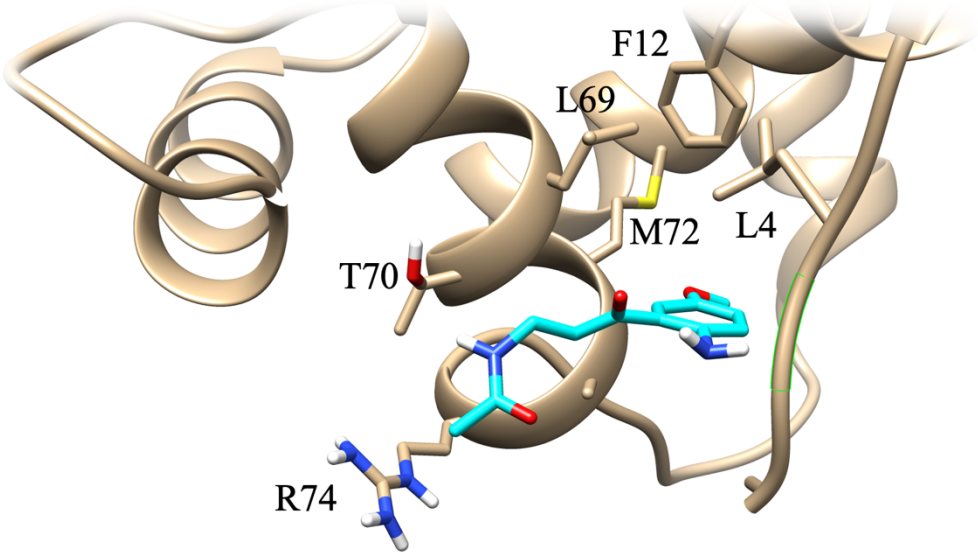

Figure 4.14 Proximal residues to AMK during the production MD simulation.
Residues in close proximity to, and interacting with CaM are shown. CaM and sidechains are shown in beige and AMK in cyan. Oxygen is depicted in red, nitrogen in blue, hydrogen in white and sulphur in yellow. The structures were prepared using USCF Chimera v 1.13.1.

4.4 Conclusions

The results of these MD studies add to the compiling evidence suggesting that AMK does not bind to CaM particularly strongly. The interaction appears to be weak and highly dynamic based on the extremely mobile nature of AMK throughout each simulation, even in its most stable binding modes. It is, therefore, not surprising that such a complex would not be amenable to more conventional NOE-based NMR structure determination methods. MD simulations are in agreement with our 2D NMR titration data; residues in CaM closest to AMK during the simulations closely mirror the residues that exhibited large, AMK-mediated changes in chemical shifts. AMK appears to situate itself within the hydrophobic cavity in a highly dynamic fashion. MD simulations also revealed a reasonable prediction of an AMK-CaM-nNOS complex in which AMK might exert allosteric effects. During these simulations, AMK primarily associates with

the linker region and the N-terminal tail, which also exhibits a likely binding surface as per the 2D NMR titrations. How such a complex might cause inhibition of nNOS in a more biologically relevant environment remains to be elucidated.

Chapter 5
Summary and Future Work

5.1 Summary

In Chapter 2, the strength of binding between CaM and prospective antagonists aMT and AMK was interrogated under saturated Ca^{2+} conditions using an array of biophysical techniques. Far-UV CD showed no saturable interaction involving AMK, and less so in the case of aMT. Furthermore, the large decreases in α-helical signal are likely the result of optical activity of the compounds, particularly aMT, as opposed to veritable alterations in secondary structure. Near-UV CD showed no change in molar ellipticity induced by either compound. AMK and aMT were similarly ineffective in impacting the electrophoretic mobility of CaM in the presence and absence of stoichiometric amounts of nNOS peptide, even at significantly elevated concentrations. ITC experiments failed to produce a viable isotherm necessary to generate parameters to quantify CaM-AMK binding. Oxyhemoglobin capture assays with AMK showed no reduction in enzyme activity regardless of ligand concentration. There were, however, suggestions of isoform-dependent reduction in affinity between CaM and nNOS induced by AMK. SPR competition experiments revealed a notable reduction in K_d values for nNOS (albeit mainly at extremely high levels of ligand), but such an occurrence was not observed with eNOS. Furthermore, the change in molar ellipticity during far-UV CD titrations upon CaM complexation with the nNOS peptide was observably reduced when CaM was pre-incubated with AMK. The same was not seen with any other NOS isoform. CaM-nNOS and CaM-eNOS isotherms were also significantly modified by the presence of AMK during ITC competition assays. Two overarching conclusions can be drawn from these experiments; the association

between CaM and AMK is weak, and AMK may have a subtle capacity to selectively modulate CaM-nNOS peptide complex formation.

In Chapter 3, NMR spectroscopy was used to conduct a more refined structural detailing of AMK interactions with CaM. Solution structures of CaM when bound to AMK in Ca^{2+}-saturating conditions closely resembled unbound holo-CaM, with the N-and C-terminal globular domains retaining their orientational independence from one another. It appears that AMK is unable to cause the significant structural rearrangements seen when CaM binds to biological targets or antagonists such as TFP.[58,59] Similar independence of globular domains was, however, seen in interactions with antagonists such as W-7 in previous studies.[122] Furthermore, no intermolecular NOEs could be observed between CaM and AMK, consistent with a very low affinity system. Monitoring of chemical shift perturbations of isotopically labelled CaM induced by AMK were observed as a means to quantify association. Approximately one third of residues exhibited significant changes in chemical shifts, distributed equally across both domains. The largest of these changes occurred within the hydrophobic pockets that are exposed upon CaM binding to Ca^{2+}. Independent fitting by non-linear regression yielded K_d values of approximately 3 mM, with the N-terminal displaying a marginally higher affinity. The overall conformation of CaM when bound to AMK and the likely binding surfaces indicate that AMK may act as a much weaker analogue of compounds such as W-7.

In Chapter 4, computational methods were used to visualize the dynamic relationship between CaM and AMK. Molecular docking simulations identified six docking sites according to free energy scoring; four on the N-terminal domain and two on the C-terminal domain. Representative poses from the various docking sites were selected for MD simulations with the only stable binding modes localized to the N-terminal. These modes are situated in the

hydrophobic cavity and characterized by close proximity to hydrophobic methionine residues and polar contacts with negatively charged aspartate and glutamate residues in the globular domain and a positively charged lysine near the central linker. A similar protocol was followed to analyze interactions between the ligand and the nNOS peptide, but no stable binding was observed, with AMK completely dissociating as the simulations progressed. MD simulations were also employed to replicate a system involving AMK, CaM and the nNOS peptide. These simulations produced a relatively stable binding mode in which AMK occupied the site between the N-terminal tail of CaM and the central helical region. Such a complex is plausible given that many of the same residues proximal to the ligand also exhibited large chemical shift changes in our 2D NMR titrations involving CaM and AMK. How nNOS might be inhibited in such a complex in a physiological setting remains unknown.

Collectively, our results are confirmation of a similar interaction between CaM and AMK as previously seen in the case of CaM and aMT. Both proceed with very low affinities and affecting similar regions of the protein. The nature of this interaction suggests that a potent competition for the hydrophobic binding sites in CaM (as exhibited by antagonists such as W-7) or limiting availability of binding regions through inducing major conformational changes (as seen with TFP) are not likely. Instead, inhibition is likely achieved through a gentle modulation of protein function *via* allosteric interaction with a CaM-nNOS complex.

5.2 Recommendations for Future Work

5.2.1 Binding Analysis under Physiological Ca^{2+} Concentrations.

Experimental work in the present study was conducted under saturating Ca^{2+} conditions. There is evidence to suggest that the antagonistic effects of AMK may be amplified under

physiological Ca^{2+} concentrations ranging from 100-225 nM, as CaM has been shown to associate more loosely with NOS when in a partially Ca^{2+}-replete state. This may help bridge the gap between enzyme inhibition seen *in vivo* and the low affinities seen in our experiments.

5.2.2 Recreation of Previously Conducted Biophysical Analyses

This analysis of AMK and its potential antagonism of CaM would be made stronger still if certain biophysical experiments could reproduce the results of previously conducted studies. Most importantly, replicating the inhibition of nNOS *in vitro* would greatly complement our structural data. It is possible that alteration of protocol or enzyme source may yield the desired effect. Further optimization of our gel mobility assays would also prove to be highly useful. It is especially strange that our assays did not show effects show in prior studies, given that experimental conditions were identical.

5.2.3 Solution Structure of CaM-AMK in complex with nNOS.

Despite the absence of intermolecular NOEs between AMK and CaM, it may be worthwhile to obtain solution structures of CaM bound to the NOS peptides in the presence of AMK. Although the localization of the ligand itself may be hard to pinpoint, any influences upon the complexation between the protein and the peptide should be apparent when comparing resonance assignments to existing NMR datasets.

Appendix A

Calmodulin Expression Information

Lysogeny Broth medium (per litre)
10 g tryptone
5 g yeast extract
5 g NaCl
100 µL 10 N NaOH
15 g agar (for plates)

M9 Medium (per litre)
6 g $Na_2HPO_4 \bullet 7H_2O$
3 g KH_2PO_4
0.5 g NaCl
1 mL 1000X micronutrients
1 mL 2 M $MgSO_4$
100 µL 1 M $CaCl_2$
100 µL 10 mM $FeSO_4$
10 mL 1 M $^{13}C_6$ D-glucose
10 mL 2 M $^{15}NH_4Cl$

1000X micronutrient Stock (per 100 mL)
30 µL 10 mM $(NH_4)_6Mo_7O_{24}$
1 mL 40 mM H_3BO_3
300 µL 10 mM $CoCl_2$
100 µL 10 mM $CuSO_4$
800 µL 10 mM $MnCl_2 \bullet 7H_2O$
100 µL 10 mM $ZnCl_2$

SDS PAGE Gel of Purified CaM Fractions

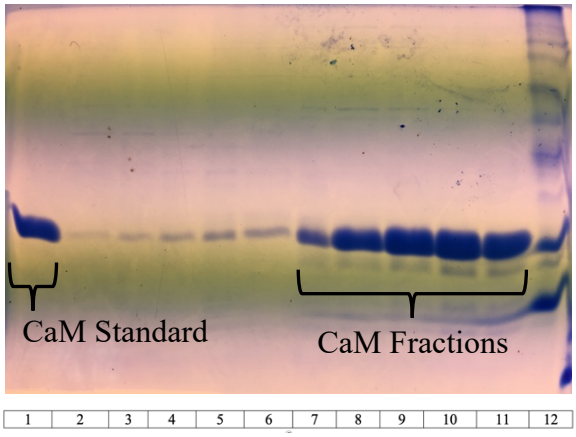

Lane 1: CaM standard
Lanes 2-6: Weak CaM fractions
Lanes 7-11: Strong CaM fractions
Lane 12: Rainbow protein standard

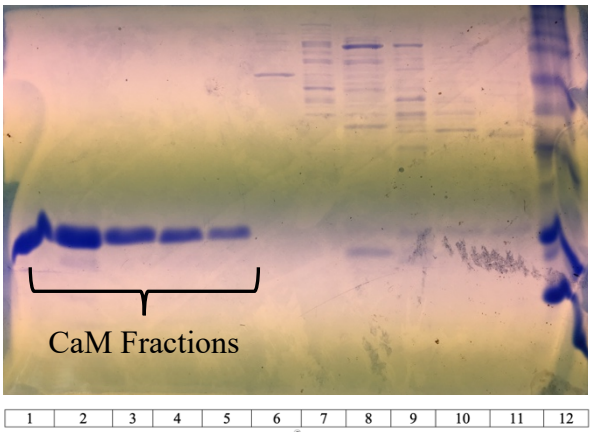

Lanes 1-5: Strong CaM fractions
Lanes 6-11: Cellular debris fractions
Lane 12: Rainbow protein standard

Appendix B

NMR Pulse Program Information

^{15}N-HSQC:

```
# 1 "/opt/xwinnmr/exp/stan/nmr/lists/pp/hsqcetf3gpsi"
;hsqcetf3gpsi
;avance-version (02/07/15)
;HSQC

;2D H-1/X correlation via double inept transfer
; using sensitivity improvement
;phase sensitive using Echo/Antiecho-TPPI gradient selection

;with decoupling during acquisition
;using trim pulses in inept transfer
;using f3 - channel
;A.G. Palmer III, J. Cavanagh, P.E. Wright & M. Rance, J. Magn.

; Reson. 93, 151-170 (1991)
;L.E. Kay, P. Keifer & T. Saarinen, J. Am. Chem. Soc. 114, ;
10663-5 (1992)
;J. Schleucher, M. Schwendinger, M. Sattler, P. Schmidt, O.
Schedletzky,
; S.J. Glaser, O.W. Sorensen & C. Griesinger, J. Biomol. NMR 4,
; 301-306 (1994)
```

HNCA:

```
# 1 "/opt/xwinnmr/exp/stan/nmr/lists/pp/hncagp3d" ;hncagp3d
;avance-version (02/05/31)
;HNCA

;3D sequence with
; inverse correlation for triple resonance using multiple
; inept transfer steps
; F1(H) -> F3(N) -> F2(Ca,t1) -> F3(N,t2) -> F1(H,t3) ;on/off
resonance Ca and C=O pulses using shaped pulse ;phase sensitive
(t1)
;phase sensitive using Echo/Antiecho gradient selection (t2) ;using
constant time in t2
;(use parameterset HNCAGP3D)
;S. Grzesiek & A. Bax, J. Magn. Reson. 96, 432 - 440 (1992)
;(J. Schleucher, M. Sattler & C. Griesinger, Angew. Chem. Int. Ed.
32,
; 1489-1491 (1993))
;(L.E. Kay, G.Y. Xu & T. Yamazaki, J. Magn. Reson. A109, 129-
133 (1994))
prosol relations=<triple>
```

HNcoCA:

```
# 1 "/opt/xwinnmr/exp/stan/nmr/lists/pp/hncocagp3d" ;hncocagp3d
;avance-version (03/08/05)

;HN(CO)CA
;3D sequence with
; inverse correlation for triple resonance using multiple
; inept transfer steps
; F1(H) -> F3(N) -> F2(C=O) -> F2(Ca,t1)
; -> F2(C=O) -> F3(N,t2) -> F1(H,t3)
;on/off resonance Ca and C=O pulses using shaped pulse ;phase
sensitive (t1)
;phase sensitive using Echo/Antiecho gradient selection (t2) ;using
constant time in t2
;(use parameterset HNCOCAGP3D)
;S. Grzesiek & A. Bax, J. Magn. Reson. 96, 432 - 440 (1992)
;(L.E. Kay, G.Y. Xu & T. Yamazaki, J. Magn. Reson. A109, 129-
133 (1994))
prosol relations=<triple>
```

CBCAcoNH:

```
# 1 "C:/Bruker/XWIN-
NMR/exp/stan/nmr/lists/pp/cbcaconhgpwg3d" ;cbcaconhgpwg3d
;avance-version (02/05/31)
;CBCACONH
;3D sequence with
; inverse correlation for triple resonance using inept transfer steps
; F1(H) -> F2(Caliph.,t1 -> Ca) -> F2(C=O) -> F3(N,t2) ->
F1(H,t3)
;on/off resonance Ca and C=O pulses using shaped pulse ;phase
sensitive (t1)
;phase sensitive (t2)
;using constant time in t1
;using constant time in t2
;water suppression using watergate sequence
;(use parameterset CBCACONHGPWG3D)
;S. Grzesiek & A. Bax, J. Biomol. NMR 3, 185-204 (1993) ;(D.R.
Muhandiram & L.E. Kay, J. Magn. Reson. B 103, 203-216 (1994))
prosol relations=<triple>
```

^{13}C-NOESY HSQC:

```
#1 "C:/Bruker/XWIN-
NMR/exp/stan/nmr/lists/pp/noesyhsqcetgp3d" ;noesyhsqcetgp3d
;avance-version (02/07/15)
;NOESY-HSQC
;3D sequence with
; homonuclear correlation via dipolar coupling
; dipolar coupling may be due to noe or chemical exchange. ; H-
1/X correlation via double inept transfer

; using sensitivity improvement
;phase sensitive (t1)
;phase sensitive using Echo/Antiecho-TPPI gradient selection (t2)
;using trim pulses in inept transfer
;with decoupling during acquisition
;using shaped pulses for inversion on f2 - channel
;(use parameterset NOESYHSQCETGP3D)
;A.L. Davis, J. Keeler, E.D. Laue & D. Moskau, J. Magn. Reson.
98,
; 207-216 (1992)
;A.G. Palmer III, J. Cavanagh, P.E. Wright & M. Rance, J. Magn.
```

; Reson. 93, 151-170 (1991)
;L.E. Kay, P. Keifer & T. Saarinen, J. Am. Chem. Soc. 114, ; 10663-5 (1992)
;J. Schleucher et al., Angew. Chem. 114(10), 1518 (1993)

^{15}N-NOESY HSQC:

1 "C:/Bruker/XWIN-NMR/exp/stan/nmr/lists/pp/noesyhsqcfpf3gpsi3d"
;noesyhsqcfpf3gpsi3d
;avance-version (03/06/18)
;NOESY-HSQC
;3D sequence with
; homonuclear correlation via dipolar coupling
; dipolar coupling may be due to noe or chemical exchange ; H-1/X correlation via double inept transfer
; using sensitivity improvement
;phase sensitive (t1)
;phase sensitive using Echo/Antiecho-TPPI gradient selection (t2)
;with decoupling during acquisition
;using flip-back pulse
;using f3 - channel
;(use parameterset NOESYHSQCFPF3GPSI3D)
;O. Zhang, L.E. Kay, J.P. Olivier & J.D. Forman-Kay,
; J. Biomol. NMR 4, 845 - 858 (1994)
;A.G. Palmer III, J. Cavanagh, P.E. Wright & M. Rance, J. Magn. ; Reson. 93, 151-170 (1991)
;L.E. Kay, P. Keifer & T. Saarinen, J. Am. Chem. Soc. 114, ; 10663-5 (1992)
;J. Schleucher, M. Schwendinger, M. Sattler, P. Schmidt, O. Schedletzky,
; S.J. Glaser, O.W. Sorensen & C. Griesinger, J. Biomol. NMR 4, ; 301-306 (1994)
prosol relations=<triple>

^{15}N-double-filtered NOESY:

1 "C:/Bruker/XWIN-NMR/exp/stan/nmr/lists/pp/noesygpphwgxf" ;noesygpphwgxf
;avance-version (02/02/07)

;2D homonuclear correlation via dipolar coupling
;dipolar coupling may be due to noe or chemical exchange ;phase sensitive
;selecting C-12 or N-14 bound protons in F1 and F2
;water suppression using watergate sequence
;
;M. Ikura & A. Bax, J. Am. Chem. Soc. 114, 2433-2440 (1992)
;M. Piotto, V. Saudek & V. Sklenar, J. Biomol. NMR 2, 661 - 666 (1992)
;V. Sklenar, M. Piotto, R. Leppik $ V. Saudek, J. Magn. Reson., ; Series A 102, 241 -245 (1993)

HC(C)H-TOCSY:

1 "C:/Bruker/XWIN- NMR/exp/stan/nmr/lists/pp/hcchdigp3d"
;hcchdigp3d
;avance-version (03/01/17)
;HCCH-TOCSY
;3D sequence with
; inverse correlation using multiple inept transfer and
; C-C DIPSI3 spinlock
; F1(H,t1) -> F2(C,t2) -> F2(C') -> F1(H',t3)
;off resonance C=O pulse using shaped pulse
;phase sensitive (t1)
;phase sensitive (t2)
;spinlock during z-filter
;(use parameterset HCCHDIGP3D)
;(L.E. Kay, G.Y. Xu, A.U. Singer, D.R. Muhandiram & J. D. Forman-Kay
; J. Magn. Reson. B 101, 333 - 337 (1993))
prosol relations=<triple>

(H)CCH-TOCSY:

1 "C:/Bruker/XWIN- NMR/exp/stan/nmr/lists/pp/hcchdigp3d2"
;hcchdigp3d2
;avance-version (02/07/16) ;HCCH-TOCSY
;3D sequence with

;
;
;
;off resonance C=O pulse using shaped pulse ;phase sensitive (t1)

inverse correlation using multiple inept transfer and C-C DIPSI3 spinlock
F1(H) -> F2(C,t1) -> F2(C',t2) -> F1(H',t3)

;phase sensitive (t2)
;spinlock during z-filter
;(use parameterset HCCHDIGP3D2)
;(L.E. Kay, G.Y. Xu, A.U. Singer, D.R. Muhandiram & J. D. Forman-Kay
; J. Magn. Reson. B 101, 333 - 337 (1993))

Appendix C

CaM-AMK Assigned Chemical Shifts

1	ALA	CA	C	51.770	8	GLN	HG2	H	2.371	14	GLU	HG3	H	2.309	21	LYS	HE3	H	2.941
1	ALA	CB	C	15.092	8	GLN	HG3	H	2.371	14	GLU	N	N	121.109	21	LYS	N	N	125.092
1	ALA	H	H	8.316	8	GLN	N	N	121.167	15	ALA	CA	C	52.574	22	ASP	CA	C	50.100
1	ALA	HA	H	4.066	9	ILE	CA	C	63.522	15	ALA	CB	C	15.508	22	ASP	CB	C	37.452
1	ALA	HB	H	1.343	9	ILE	CB	C	35.033	15	ALA	H	H	7.857	22	ASP	H	H	7.902
1	ALA	N	N	123.948	9	ILE	CG1	C	27.324	15	ALA	HA	H	4.236	22	ASP	HA	H	4.557
3	GLN	CA	C	56.734	9	ILE	CG2	C	14.619	15	ALA	HB	H	1.917	22	ASP	HB2	H	3.018
3	GLN	CB	C	25.300	9	ILE	CD1	C	10.275	15	ALA	N	N	123.422	22	ASP	HB3	H	3.018
3	GLN	CG	C	31.255	9	ILE	H	H	8.248	16	PHE	CA	C	59.286	22	ASP	N	N	114.556
3	GLN	H	H	7.787	9	ILE	HA	H	3.656	16	PHE	CB	C	37.045	23	GLY	CA	C	44.486
3	GLN	HA	H	3.833	9	ILE	HB	H	1.903	16	PHE	H	H	8.686	23	GLY	H	H	7.546
3	GLN	HB2	H	2.092	9	ILE	HG12	H	1.066	16	PHE	HA	H	3.196	23	GLY	HA2	H	3.818
3	GLN	HG2	H	2.363	9	ILE	HG2	H	1.018	16	PHE	HB2	H	3.133	23	GLY	HA3	H	3.818
3	GLN	N	N	118.748	9	ILE	HD1	H	0.819	16	PHE	HB3	H	3.133	23	GLY	N	N	109.956
4	LEU	CA	C	56.559	9	ILE	N	N	120.276	16	PHE	N	N	120.047	24	ASP	CA	C	51.121
4	LEU	CB	C	39.755	10	ALA	CA	C	52.705	17	SER	CA	C	58.822	24	ASP	CB	C	38.387
4	LEU	CG	C	23.297	10	ALA	CB	C	15.276	17	SER	CB	C	60.552	24	ASP	H	H	8.249
4	LEU	CD1	C	21.186	10	ALA	H	H	7.864	17	SER	H	H	7.830	24	ASP	HA	H	4.446
4	LEU	CD2	C	19.995	10	ALA	HA	H	4.038	17	SER	HA	H	4.087	24	ASP	HB2	H	2.911
4	LEU	H	H	7.572	10	ALA	HB	H	1.486	17	SER	HB2	H	3.996	24	ASP	HB3	H	2.911
4	LEU	HA	H	3.993	10	ALA	N	N	121.903	17	SER	N	N	113.565	24	ASP	N	N	121.400
4	LEU	HB2	H	1.839	11	GLU	CA	C	56.688	18	LEU	CA	C	54.437	25	GLY	CA	C	42.909
4	LEU	HB3	H	1.753	11	GLU	CB	C	25.733	18	LEU	CB	C	39.430	25	GLY	H	H	10.500
4	LEU	HG	H	1.522	11	GLU	CG	C	33.312	18	LEU	CG	C	23.405	25	GLY	HA2	H	4.328
4	LEU	HD1	H	0.798	11	GLU	H	H	7.648	18	LEU	CD1	C	21.348	25	GLY	HA3	H	4.326
4	LEU	HD2	H	0.753	11	GLU	HA	H	3.983	18	LEU	CD2	C	19.941	25	GLY	N	N	113.852
4	LEU	N	N	122.359	11	GLU	HB2	H	2.069	18	LEU	H	H	7.261	26	THR	CA	C	57.059
5	THR	CA	C	57.755	11	GLU	HB3	H	2.009	18	LEU	HA	H	4.079	26	THR	CB	C	69.832
5	THR	CB	C	68.455	11	GLU	HG2	H	2.362	18	LEU	HB2	H	1.837	26	THR	CG2	C	18.870
5	THR	CG2	C	19.013	11	GLU	HG3	H	2.310	18	LEU	HB3	H	1.769	26	THR	H	H	8.002
5	THR	H	H	8.624	11	GLU	N	N	120.402	18	LEU	HG	H	1.524	26	THR	HA	H	5.278
5	THR	HA	H	4.391	12	PHE	CA	C	56.502	18	LEU	HD1	H	0.794	26	THR	HB	H	3.810
5	THR	HB	H	4.749	12	PHE	CB	C	34.985	18	LEU	HD2	H	0.759	26	THR	HG2	H	0.983
5	THR	HG2	H	1.286	12	PHE	H	H	8.448	18	LEU	N	N	121.520	26	THR	N	N	113.489
5	THR	N	N	113.769	12	PHE	HA	H	4.997	19	PHE	CA	C	56.595	27	ILE	CA	C	57.709
6	GLU	CA	C	57.291	12	PHE	HB2	H	3.480	19	PHE	CB	C	38.157	27	ILE	CB	C	36.982
6	GLU	CB	C	25.772	12	PHE	HB3	H	3.398	19	PHE	H	H	7.123	27	ILE	CG1	C	24.349
6	GLU	CG	C	33.545	12	PHE	N	N	120.961	19	PHE	HA	H	4.229	27	ILE	CG2	C	14.817
6	GLU	H	H	8.894	13	LYS	CA	C	57.430	19	PHE	HB2	H	2.632	27	ILE	CD1	C	12.648
6	GLU	HA	H	3.973	13	LYS	CB	C	29.496	19	PHE	HB3	H	2.632	27	ILE	H	H	9.691
6	GLU	HB2	H	2.063	13	LYS	CG	C	21.808	19	PHE	N	N	115.449	27	ILE	HA	H	4.928
6	GLU	HB3	H	2.009	13	LYS	CD	C	25.923	20	ASP	CA	C	49.497	27	ILE	HB	H	1.742
6	GLU	HG2	H	2.360	13	LYS	CE	C	39.240	20	ASP	CB	C	35.744	27	ILE	HG12	H	0.265
6	GLU	HG3	H	2.306	13	LYS	H	H	9.079	20	ASP	H	H	7.692	27	ILE	HG2	H	0.837
6	GLU	N	N	121.153	13	LYS	HA	H	3.956	20	ASP	HA	H	4.511	27	ILE	HD1	H	0.216
7	GLU	CA	C	55.760	13	LYS	HB2	H	1.824	20	ASP	HB2	H	1.479	27	ILE	N	N	127.639
7	GLU	CB	C	26.455	13	LYS	HB3	H	1.824	20	ASP	HB3	H	1.458	28	THR	CA	C	56.690
7	GLU	CG	C	33.296	13	LYS	HG2	H	1.349	20	ASP	N	N	118.306	28	THR	CB	C	69.890
7	GLU	H	H	8.600	13	LYS	HG3	H	1.349	21	LYS	CA	C	55.760	28	THR	CG2	C	18.637
7	GLU	HA	H	4.062	13	LYS	HD2	H	1.615	21	LYS	CB	C	29.929	28	THR	H	H	8.287
7	GLU	HB2	H	2.063	13	LYS	HD3	H	1.615	21	LYS	CG	C	21.808	28	THR	HA	H	4.776
7	GLU	HB3	H	2.018	13	LYS	HE2	H	2.941	21	LYS	CD	C	26.031	28	THR	HB	H	4.786
7	GLU	HG2	H	2.353	13	LYS	HE3	H	2.941	21	LYS	CE	C	39.349	28	THR	HG2	H	1.286
7	GLU	HG3	H	2.308	13	LYS	N	N	124.361	21	LYS	H	H	7.545	28	THR	N	N	117.149
7	GLU	N	N	120.295	14	GLU	CA	C	56.471	21	LYS	HA	H	3.971	29	THR	CA	C	63.701
8	GLN	CA	C	56.502	14	GLU	CB	C	26.166	21	LYS	HB2	H	1.824	29	THR	CB	C	65.547
8	GLN	CB	C	25.436	14	GLU	CG	C	33.204	21	LYS	HB3	H	1.824	29	THR	CG2	C	19.397
8	GLN	CG	C	31.228	14	GLU	H	H	7.649	21	LYS	HG2	H	1.348	29	THR	H	H	8.988
8	GLN	H	H	7.621	14	GLU	HA	H	3.994	21	LYS	HG3	H	1.348	29	THR	HA	H	3.697
8	GLN	HA	H	3.796	14	GLU	HB2	H	2.060	21	LYS	HD2	H	1.634	29	THR	HB	H	4.245
8	GLN	HB2	H	2.086	14	GLU	HB3	H	2.010	21	LYS	HD3	H	1.634	29	THR	HG2	H	1.218
8	GLN	HB3	H	2.086	14	GLU	HG2	H	2.372	21	LYS	HE2	H	2.941	29	THR	N	N	113.487

30 LYS H H 7.400
30 LYS N N 120.979
31 GLU CA C 56.456
31 GLU CB C 26.600
31 GLU CG C 33.421
31 GLU H H 7.532
31 GLU HA H 4.062
31 GLU HB2 H 2.072
31 GLU HB3 H 2.013
31 GLU HG2 H 2.356
31 GLU HG3 H 2.302
31 GLU N N 121.579
32 LEU CA C 55.308
32 LEU CB C 39.705
32 LEU CG C 23.351
32 LEU CD1 C 21.186
32 LEU CD2 C 19.887
32 LEU H H 8.582
32 LEU HA H 4.083
32 LEU HB2 H 1.841
32 LEU HB3 H 1.752
32 LEU HG H 1.522
32 LEU HD1 H 0.802
32 LEU HD2 H 0.757
32 LEU N N 121.387
33 GLY CA C 45.646
33 GLY H H 8.527
33 GLY HA2 H 3.942
33 GLY HA3 H 3.942
33 GLY N N 106.367
34 THR CA C 64.247
34 THR CB C 66.035
34 THR CG2 C 18.854
34 THR H H 7.757
34 THR HA H 3.878
34 THR HB H 4.285
34 THR HG2 H 1.228
34 THR N N 118.306
35 VAL CA C 63.601
35 VAL CB C 28.724
35 VAL CG1 C 20.766
35 VAL CG2 C 20.766
35 VAL H H 7.487
35 VAL HA H 3.489
35 VAL HB H 1.942
35 VAL HG1 H 0.645
35 VAL HG2 H 0.645
35 VAL N N 122.742
36 MET CA C 56.377
36 MET CB C 28.488
36 MET CG C 29.929
36 MET CE C 18.939
36 MET H H 8.359
36 MET HA H 4.092
36 MET HB2 H 1.940
36 MET HB3 H 1.940
36 MET HG2 H 2.553
36 MET HG3 H 2.553
36 MET N N 119.266
37 ARG CA C 57.180
37 ARG CB C 29.794
37 ARG CG C 25.950
37 ARG CD C 39.269
37 ARG H H 8.400
37 ARG HA H 4.786
37 ARG HB2 H 1.830
37 ARG HB3 H 1.830
37 ARG HG2 H 1.614
37 ARG HG3 H 1.614
37 ARG HD2 H 2.941
37 ARG HD3 H 2.941
37 ARG N N 119.685
38 SER CA C 56.290
38 SER CB C 61.040
38 SER H H 7.826
38 SER HA H 4.408
38 SER HB2 H 3.917
38 SER HB3 H 4.016
38 SER N N 119.447
39 LEU CA C 54.418
39 LEU CB C 39.542
39 LEU CG C 23.401
39 LEU CD1 C 21.220
39 LEU CD2 C 19.911
39 LEU H H 7.246
39 LEU HA H 4.074
39 LEU HB2 H 1.754
39 LEU HB3 H 1.754
39 LEU HG H 1.601
39 LEU HD1 H 0.792
39 LEU HD2 H 0.792
39 LEU N N 121.490
40 GLY CA C 42.816
40 GLY H H 7.721
40 GLY HA2 H 4.205
40 GLY HA3 H 4.205
40 GLY N N 107.609
41 GLN CA C 51.724
41 GLN CB C 27.687
41 GLN CG C 31.093
41 GLN H H 7.651
41 GLN HA H 4.453
41 GLN HB2 H 1.595
41 GLN HB3 H 1.595
41 GLN HG2 H 2.200
41 GLN HG3 H 2.200
41 GLN N N 119.165
42 ASN CA C 48.476
42 ASN CB C 35.994
42 ASN H H 8.587
42 ASN HA H 5.250
42 ASN HB2 H 2.316
42 ASN HB3 H 2.235
42 ASN N N 116.919
44 THR CA C 57.755
44 THR CB C 68.382
44 THR CG2 C 19.046
44 THR H H 8.615
44 THR HA H 4.404
44 THR HB H 4.753
44 THR HG2 H 1.286
44 THR N N 113.744
45 GLU CA C 57.198
45 GLU CB C 25.660
45 GLU CG C 33.467
45 GLU H H 8.674
45 GLU HA H 4.046
45 GLU HB2 H 2.063
45 GLU HB3 H 2.011
45 GLU HG2 H 2.354
45 GLU HG3 H 2.300
45 GLU N N 121.336
46 ALA CA C 52.280
46 ALA H H 8.135
46 ALA HA H 4.071
46 ALA HB H 1.338
46 ALA N N 121.491
47 GLU CA C 56.224
47 GLU CB C 26.563
47 GLU CG C 33.079
47 GLU H H 7.561
47 GLU HA H 3.989
47 GLU HB2 H 2.073
47 GLU HB3 H 2.011
47 GLU HG2 H 2.354
47 GLU HG3 H 2.306
47 GLU N N 119.459
48 LEU CA C 55.203
48 LEU CB C 39.646
48 LEU CG C 23.297
48 LEU CD1 C 21.051
48 LEU CD2 C 19.697
48 LEU H H 8.050
48 LEU HA H 4.084
48 LEU HB2 H 1.839
48 LEU HB3 H 1.769
48 LEU HG H 1.518
48 LEU HD1 H 0.803
48 LEU HD2 H 0.751
48 LEU N N 121.129
49 GLN CA C 55.806
49 GLN CG C 31.580
49 GLN H H 8.051
49 GLN HA H 3.789
49 GLN HB2 H 2.087
49 GLN HB3 H 2.087
49 GLN HG2 H 2.372
49 GLN HG3 H 2.372
49 GLN N N 118.961
50 ASP CA C 54.879
50 ASP CB C 37.640
50 ASP H H 7.951
50 ASP HA H 4.284
50 ASP HB2 H 2.739
50 ASP HB3 H 2.739
50 ASP N N 120.696
51 MET CA C 56.424
51 MET CB C 29.781
51 MET CG C 29.781
51 MET CE C 15.556
51 MET H H 7.766
51 MET HA H 4.008
51 MET HB2 H 2.200
51 MET HB3 H 2.200
51 MET HG2 H 2.480
51 MET HG3 H 2.480
51 MET HE H 1.925
51 MET N N 119.636
52 ILE CA C 61.977
52 ILE CB C 34.273
52 ILE CG1 C 26.129
52 ILE CG2 C 13.207
52 ILE CD1 C 9.950
52 ILE H H 7.580
52 ILE HA H 3.474
52 ILE HB H 1.911
52 ILE HG12 H 1.027
52 ILE HG13 H 0.954
52 ILE HD1 H 0.656
52 ILE N N 118.883
53 ASN CA C 53.162
53 ASN CB C 35.129
53 ASN H H 8.465
53 ASN HA H 4.351
53 ASN HB2 H 2.950
53 ASN HB3 H 2.950
53 ASN N N 118.347
54 GLU CA C 56.131
54 GLU CB C 26.491
54 GLU CG C 33.451
54 GLU H H 7.436
54 GLU HA H 3.984
54 GLU HB2 H 2.065
54 GLU HB3 H 2.008
54 GLU HG2 H 2.351
54 GLU HG3 H 2.310
54 GLU N N 117.149
55 VAL CA C 58.080
55 VAL CB C 30.091
55 VAL CG1 C 18.939
55 VAL CG2 C 18.939
55 VAL H H 7.059
55 VAL HA H 4.404
55 VAL HB H 2.304
55 VAL HG1 H 0.779
55 VAL HG2 H 0.779
55 VAL N N 109.605
56 ASP CA C 50.955
56 ASP H H 7.541
56 ASP N N 122.277
57 ALA CA C 51.584
57 ALA CB C 15.231
57 ALA H H 8.255
57 ALA HA H 4.061
57 ALA HB H 1.343
57 ALA N N 132.403
58 ASP CA C 50.146
58 ASP CB C 36.713
58 ASP H H 8.016
58 ASP HA H 4.537
58 ASP HB2 H 3.027
58 ASP HB3 H 3.027
58 ASP N N 114.404
59 GLY CA C 44.718
59 GLY H H 7.444
59 GLY HA2 H 3.814
59 GLY HA3 H 3.814
59 GLY N N 109.187
60 ASN CA C 56.468
60 ASN CB C 35.082
60 ASN H H 7.987
60 ASN HA H 5.003
60 ASN HB2 H 3.483
60 ASN HB3 H 3.483
60 ASN N N 119.224
61 GLY CA C 42.723
61 GLY H H 10.468
61 GLY HA2 H 4.198
61 GLY HA3 H 4.198
61 GLY N N 114.117
62 THR CA C 56.734
62 THR CB C 69.832
62 THR CG2 C 18.870
62 THR H H 7.529
62 THR HA H 4.789
62 THR HB H 3.983
62 THR HG2 H 1.255
62 THR N N 109.565
63 ILE CA C 57.013
63 ILE CB C 36.822
63 ILE CG1 C 24.642
63 ILE CG2 C 15.290
63 ILE CD1 C 10.614
63 ILE H H 8.742
63 ILE HA H 5.148
63 ILE HB H 2.037
63 ILE HG2 H 1.183
63 ILE HD1 H 0.789
63 ILE N N 124.376
64 ASP CA C 49.311

64 ASP CB C 36.375
64 ASP H H 8.679
64 ASP HA H 5.160
64 ASP HB2 H 2.739
64 ASP HB3 H 2.476
64 ASP N N 128.861
65 PHE CA C 60.724
65 PHE CB C 33.250
65 PHE H H 8.807
65 PHE HA H 3.951
65 PHE HB2 H 2.774
65 PHE HB3 H 2.774
65 PHE N N 119.342
67 GLU CA C 56.131
67 GLU CB C 26.564
67 GLU CG C 33.079
67 GLU H H 7.888
67 GLU HA H 4.110
67 GLU HB2 H 2.070
67 GLU HB3 H 2.014
67 GLU HG2 H 2.353
67 GLU HG3 H 2.306
67 GLU N N 118.370
68 PHE CA C 58.590
68 PHE CB C 36.747
68 PHE H H 8.685
68 PHE HA H 3.929
68 PHE HB2 H 3.197
68 PHE HB3 H 3.112
68 PHE N N 124.361
69 LEU CA C 55.210
69 LEU CB C 38.212
69 LEU CG C 22.891
69 LEU CD2 C 21.159
69 LEU H H 8.336
69 LEU HA H 3.291
69 LEU HB2 H 1.112
69 LEU HB3 H 1.112
69 LEU HG H 0.958
69 LEU HD2 H 0.569
69 LEU N N 119.876
70 THR CA C 63.694
70 THR CB C 65.313
70 THR CG2 C 20.401
70 THR H H 7.422
70 THR HA H 3.757
70 THR HB H 4.248
70 THR HG2 H 1.216
70 THR N N 116.349
71 MET CA C 56.595
71 MET CB C 29.942
71 MET CG C 29.563
71 MET CE C 15.907
71 MET H H 7.536
71 MET HA H 4.013
71 MET HB2 H 2.006
71 MET HB3 H 2.006
71 MET HG2 H 2.311
71 MET HG3 H 2.311
71 MET HE H 1.523
71 MET N N 122.388
72 MET CA C 53.023
72 MET CB C 29.278
72 MET CG C 29.448
72 MET CE C 15.053
72 MET H H 7.935
72 MET HA H 3.947
72 MET HB2 H 1.065
72 MET HB3 H 1.065
72 MET HG2 H 1.252
72 MET HG3 H 1.252
72 MET HE H 1.922
72 MET N N 117.760
73 ALA CA C 51.850
73 ALA CB C 15.556
73 ALA H H 8.083
73 ALA HA H 4.004
73 ALA HB H 1.352
73 ALA N N 122.962
74 ARG H H 7.314
74 ARG N N 116.847
75 LYS CA C 56.317
75 LYS CB C 29.604
75 LYS CG C 21.917
75 LYS CD C 25.815
75 LYS CE C 39.240
75 LYS H H 7.527
75 LYS HA H 3.985
75 LYS HB2 H 1.828
75 LYS HB3 H 1.828
75 LYS HG2 H 1.430
75 LYS HG3 H 1.430
75 LYS HD2 H 1.629
75 LYS HD3 H 1.629
75 LYS HE2 H 2.946
75 LYS HE3 H 2.946
75 LYS N N 119.423
76 MET CA C 53.950
76 MET CB C 29.577
76 MET CG C 29.577
76 MET H H 7.704
76 MET HA H 4.313
76 MET HB2 H 2.132
76 MET HB3 H 2.132
76 MET HG2 H 2.614
76 MET HG3 H 2.614
76 MET N N 119.163
77 LYS CA C 52.559
77 LYS CB C 29.279
77 LYS CG C 21.808
77 LYS CD C 26.248
77 LYS CE C 39.240
77 LYS H H 7.779
77 LYS HA H 4.326
77 LYS HB2 H 1.748
77 LYS HB3 H 1.748
77 LYS HG2 H 1.355
77 LYS HG3 H 1.355
77 LYS HD2 H 1.623
77 LYS HD3 H 1.623
77 LYS HE2 H 2.939
77 LYS HE3 H 2.939
77 LYS N N 121.137
78 ASP CA C 51.944
78 ASP CB C 38.563
78 ASP H H 8.129
78 ASP HA H 4.589
78 ASP HB2 H 2.637
78 ASP HB3 H 2.637
78 ASP N N 122.316
79 THR CA C 59.657
79 THR CB C 67.284
79 THR CG2 C 18.637
79 THR H H 7.965
79 THR HA H 4.252
79 THR HB H 4.189
79 THR HG2 H 1.130
79 THR N N 115.433
80 ASP CA C 51.677
80 ASP CB C 38.507
80 ASP H H 8.157
80 ASP HA H 4.583
80 ASP HB2 H 2.523
80 ASP HB3 H 2.523
80 ASP N N 123.859
81 SER CA C 56.595
81 SER CB C 60.922
81 SER H H 8.304
81 SER HA H 4.409
81 SER HB2 H 3.918
81 SER HB3 H 3.918
81 SER N N 117.940
82 GLU CA C 55.992
82 GLU CB C 26.418
82 GLU CG C 33.497
82 GLU H H 8.365
82 GLU HA H 4.072
82 GLU HB2 H 2.062
82 GLU HB3 H 2.007
82 GLU HG2 H 2.358
82 GLU HG3 H 2.307
82 GLU N N 123.180
83 GLU CA C 55.902
83 GLU CB C 26.127
83 GLU CG C 33.326
83 GLU H H 8.214
83 GLU HA H 4.094
83 GLU HB2 H 2.069
83 GLU HB3 H 2.001
83 GLU HG2 H 2.297
83 GLU HG3 H 2.356
83 GLU N N 120.409
84 GLU CA C 56.661
84 GLU CB C 26.419
84 GLU CG C 33.329
84 GLU H H 8.009
84 GLU HA H 4.074
84 GLU HB2 H 2.062
84 GLU HB3 H 2.008
84 GLU HG2 H 2.374
84 GLU HG3 H 2.315
84 GLU N N 119.430
85 ILE CA C 62.047
85 ILE CB C 34.695
85 ILE CG1 C 26.092
85 ILE CG2 C 16.073
85 ILE CD1 C 10.301
85 ILE H H 7.892
85 ILE HA H 3.965
85 ILE HB H 2.117
85 ILE HG12 H 1.043
85 ILE HG13 H 1.043
85 ILE HG2 H 1.043
85 ILE HD1 H 0.743
85 ILE N N 122.881
86 ARG CA C 57.430
86 ARG CB C 29.631
86 ARG CD C 39.376
86 ARG H H 8.285
86 ARG HA H 3.963
86 ARG HB2 H 1.821
86 ARG HB3 H 1.771
86 ARG HG2 H 1.647
86 ARG HG3 H 1.624
86 ARG HD2 H 2.946
86 ARG HD3 H 2.935
86 ARG N N 122.450
87 GLU CA C 57.616
87 GLU CB C 25.556
87 GLU CG C 33.545
87 GLU H H 7.949
87 GLU HA H 3.978
87 GLU HB2 H 2.072
87 GLU HB3 H 2.012
87 GLU HG2 H 2.359
87 GLU HG3 H 2.303
87 GLU N N 119.254
88 ALA CA C 52.605
88 ALA CB C 15.122
88 ALA H H 7.769
88 ALA HA H 4.172
88 ALA HB H 1.736
88 ALA N N 122.950
89 PHE CA C 59.364
89 PHE CB C 36.662
89 PHE H H 8.406
89 PHE HA H 3.189
89 PHE HB2 H 3.113
89 PHE HB3 H 3.113
89 PHE N N 119.609
90 ARG CA C 56.131
90 ARG CB C 27.503
90 ARG CG C 24.792
90 ARG CD C 40.732
90 ARG H H 7.570
90 ARG HA H 3.839
90 ARG HB2 H 1.923
90 ARG HB3 H 1.923
90 ARG HG3 H 1.841
90 ARG HD2 H 3.165
90 ARG HD3 H 3.165
90 ARG N N 116.501
91 VAL CA C 63.044
91 VAL CB C 28.883
91 VAL CG1 C 19.966
91 VAL CG2 C 19.966
91 VAL H H 7.382
91 VAL HA H 3.470
91 VAL HB H 2.108
91 VAL HG1 H 0.970
91 VAL HG2 H 0.970
91 VAL N N 119.033
92 PHE CA C 55.490
92 PHE CB C 37.479
92 PHE H H 7.401
92 PHE HA H 4.320
92 PHE HB2 H 2.718
92 PHE HB3 H 2.600
92 PHE N N 117.569
93 ASP CA C 49.497
93 ASP CB C 35.843
93 ASP H H 7.704
93 ASP HA H 4.509
93 ASP HB2 H 1.315
93 ASP HB3 H 1.315
93 ASP N N 117.577
94 LYS CA C 54.786
94 LYS CB C 30.579
94 LYS CG C 21.808
94 LYS CD C 26.031
94 LYS CE C 39.349
94 LYS H H 7.606
94 LYS HA H 4.082
94 LYS HB2 H 1.765
94 LYS HB3 H 1.765
94 LYS HG2 H 1.348
94 LYS HG3 H 1.348
94 LYS HD2 H 1.625
94 LYS HD3 H 1.625
94 LYS HE2 H 2.941

94 LYS HE3 H 2.941
94 LYS N N 126.417
95 ASP CA C 50.217
95 ASP CB C 36.713
95 ASP H H 8.046
95 ASP HA H 4.496
95 ASP HB2 H 3.025
95 ASP HB3 H 3.025
95 ASP N N 114.652
96 GLY CA C 44.486
96 GLY H H 7.646
96 GLY HA2 H 3.827
96 GLY HA3 H 3.827
96 GLY N N 110.010
97 ASN CA C 49.914
97 ASN CB C 36.662
97 ASN H H 8.178
97 ASN HA H 4.528
97 ASN HB2 H 2.608
97 ASN HB3 H 2.608
97 ASN N N 120.276
98 GLY CA C 42.611
98 GLY H H 10.514
98 GLY HA2 H 4.010
98 GLY HA3 H 4.010
98 GLY N N 113.700
99 TYR CA C 53.348
99 TYR CB C 40.340
99 TYR H H 7.480
99 TYR HA H 5.019
99 TYR HB2 H 2.509
99 TYR HB3 H 2.461
99 TYR N N 116.539
100 ILE CA C 57.755
100 ILE CG1 C 24.142
100 ILE CG2 C 14.817
100 ILE CD1 C 12.648
100 ILE H H 9.994
100 ILE HA H 4.923
100 ILE HB H 1.752
100 ILE HG12 H 0.262
100 ILE HG2 H 0.841
100 ILE HD1 H 0.212
100 ILE N N 127.958
101 SER CA C 53.116
101 SER CB C 63.664
101 SER H H 8.804
101 SER HA H 4.815
101 SER HB2 H 3.950
101 SER HB3 H 3.950
101 SER N N 124.494
102 ALA CA C 53.116
102 ALA CB C 15.201
102 ALA H H 9.079
102 ALA HA H 3.899
102 ALA HB H 1.419
102 ALA N N 123.653
103 ALA CA C 52.466
103 ALA CB C 15.596
103 ALA H H 8.111
103 ALA HA H 3.984
103 ALA HB H 1.352
103 ALA N N 119.056
104 GLU CA C 56.688
104 GLU CB C 25.551
104 GLU CG C 33.358
104 GLU H H 7.737
104 GLU HA H 4.001
104 GLU HB2 H 2.066
104 GLU HB3 H 2.009
104 GLU HG2 H 2.362
104 GLU HG3 H 2.315
104 GLU N N 120.549
105 LEU CA C 55.435
105 LEU CG C 23.696
105 LEU CD1 C 21.159
105 LEU CD2 C 19.907
105 LEU H H 8.452
105 LEU HA H 4.086
105 LEU HB2 H 1.838
105 LEU HB3 H 1.780
105 LEU HG H 1.517
105 LEU HD1 H 0.798
105 LEU HD2 H 0.752
105 LEU N N 121.762
106 ARG CA C 53.157
106 ARG CB C 29.252
106 ARG CG C 26.004
106 ARG CD C 39.213
106 ARG H H 8.444
106 ARG HA H 4.343
106 ARG HB2 H 1.822
106 ARG HB3 H 1.768
106 ARG HG2 H 1.642
106 ARG HG3 H 1.619
106 ARG HD2 H 2.947
106 ARG HD3 H 2.935
106 ARG N N 118.210
107 HIS CA C 56.237
107 HIS CB C 27.033
107 HIS H H 7.804
107 HIS HA H 4.329
107 HIS HB3 H 3.311
107 HIS N N 119.565
108 VAL CA C 58.911
108 VAL CB C 35.675
108 VAL CG1 C
14.657
108 VAL CG2 C
14.657
108 VAL H H 7.761
108 VAL HA H 3.611
108 VAL HB H 1.959
108 VAL HG1 H 0.923
108 VAL HG2 H 0.923
108 VAL N N 119.795
109 MET CB C 31.008
109 MET CG C 31.008
109 MET CE C 19.047
109 MET H H 8.141
109 MET HA H 4.454
109 MET HB2 H 1.930
109 MET HB3 H 1.930
109 MET HG2 H 2.190
109 MET HG3 H 2.190
109 MET N N 117.092
110 THR CA C 62.951
110 THR CB C 66.307
110 THR CG2 C
18.745
110 THR H H 8.025
110 THR HA H 4.116
110 THR HB H 4.243
110 THR HG2 H 1.184
110 THR N N 115.739
111 ASN CA C 52.420
111 ASN CB C 38.398
111 ASN H H 7.805
111 ASN HA H 4.616
111 ASN HB2 H 2.632
111 ASN HB3 H 2.632
111 ASN N N 122.761
112 LEU CA C 51.724
112 LEU CB C 39.540
112 LEU CG C 23.252
112 LEU CD1 C 21.118
112 LEU CD2 C 19.846
112 LEU H H 7.706
112 LEU HA H 4.443
112 LEU HB2 H 1.839
112 LEU HB3 H 1.759
112 LEU HG H 1.522
112 LEU HD1 H 0.801
112 LEU HD2 H 0.787
112 LEU N N 119.226
113 GLY CA C 42.816
113 GLY H H 7.750
113 GLY HA2 H 4.198
113 GLY HA3 H 4.198
113 GLY N N 107.622
114 GLU CA C 56.502
114 GLU CB C 26.600
114 GLU CG C 33.342
114 GLU H H 7.686
114 GLU HA H 4.095
114 GLU HB2 H 2.070
114 GLU HB3 H 2.010
114 GLU HG2 H 2.361
114 GLU HG3 H 2.307
114 GLU N N 121.196
115 LYS CA C 52.791
115 LYS CB C 29.252
115 LYS CG C 21.917
115 LYS CD C 26.248
115 LYS H H 8.448
115 LYS HA H 4.346
115 LYS HB2 H 1.758
115 LYS HB3 H 1.758
115 LYS HG2 H 1.353
115 LYS HG3 H 1.353
115 LYS HD2 H 1.615
115 LYS HD3 H 1.615
115 LYS HE3 H 2.932
115 LYS N N 124.715
116 LEU CA C 51.306
116 LEU CB C 39.349
116 LEU CG C 23.216
116 LEU CD1 C 21.082
116 LEU CD2 C 19.993
116 LEU H H 7.972
116 LEU HA H 4.446
116 LEU HB2 H 1.842
116 LEU HB3 H 1.758
116 LEU HG H 1.520
116 LEU HD1 H 0.796
116 LEU HD2 H 0.758
116 LEU N N 125.517
117 THR CA C 57.848
117 THR CB C 68.370
117 THR CG2 C
18.854
117 THR H H 9.085
117 THR HA H 4.406
117 THR HB H 4.745
117 THR HG2 H 1.282
117 THR N N 115.354
118 ASP CA C 55.203
118 ASP CB C 37.636
118 ASP H H 8.757
118 ASP HA H 4.325
118 ASP HB2 H 2.640
118 ASP HB3 H 2.640
118 ASP N N 121.684
119 GLU CA C 57.059
119 GLU CB C 25.551
119 GLU CG C 33.405
119 GLU H H 8.538
119 GLU HA H 3.980
119 GLU HB2 H 2.070
119 GLU HB3 H 2.009
119 GLU HG2 H 2.361
119 GLU HG3 H 2.307
119 GLU N N 119.819
120 GLU CA C 56.502
120 GLU CB C 25.842
120 GLU CG C 33.204
120 GLU H H 7.621
120 GLU HA H 3.996
120 GLU HB2 H 2.059
120 GLU HB3 H 2.059
120 GLU HG2 H 2.369
120 GLU HG3 H 2.310
120 GLU N N 121.226
121 VAL CA C 64.170
121 VAL CB C 28.630
121 VAL CG1 C
20.996
121 VAL CG2 C
20.996
121 VAL H H 7.940
121 VAL HA H 3.568
121 VAL HB H 2.168
121 VAL HG1 H 0.914
121 VAL HG2 H 0.914
121 VAL N N 121.814
122 ASP CA C 54.786
122 ASP CB C 37.422
122 ASP H H 7.900
122 ASP HA H 4.325
122 ASP HB2 H 2.719
122 ASP HB3 H 2.719
122 ASP N N 120.391
123 GLU CA C 56.178
123 GLU CB C 26.455
123 GLU CG C 33.296
123 GLU H H 7.844
123 GLU HA H 4.041
123 GLU HB2 H 2.062
123 GLU HB3 H 2.010
123 GLU HG2 H 2.346
123 GLU HG3 H 2.307
123 GLU N N 120.238
124 MET CA C 56.688
124 MET CB C 29.523
124 MET CG C 29.523
124 MET H H 7.717
124 MET HA H 4.005
124 MET HB2 H 2.197
124 MET HB3 H 2.197
124 MET HG2 H 2.465
124 MET HG3 H 2.465
124 MET N N 120.048
125 ILE CA C 61.137
125 ILE CB C 33.459
125 ILE CG1 C 25.206
125 ILE CG2 C 13.479
125 ILE CD1 C 7.941
125 ILE H H 7.819
125 ILE HA H 3.474
125 ILE HB H 2.094

125 ILE HG12 H 1.259
125 ILE HG13 H 1.259
125 ILE HG2 H 0.688
125 ILE HD1 H 0.678
125 ILE N N 119.153
126 ARG CA C 55.853
126 ARG CB C 29.902
126 ARG CG C 25.896
126 ARG CD C 39.213
126 ARG H H 8.045
126 ARG HA H 4.003
126 ARG HB2 H 1.819
126 ARG HB3 H 1.765
126 ARG HG2 H 1.641
126 ARG HG3 H 1.620
126 ARG HD2 H 2.948
126 ARG HD3 H 2.936
126 ARG N N 118.995
127 GLU CA C 55.714
127 GLU CB C 26.564
127 GLU CG C 33.187
127 GLU H H 7.807
127 GLU HA H 3.978
127 GLU HB2 H 2.062
127 GLU HB3 H 2.010
127 GLU HG2 H 2.355
127 GLU HG3 H 2.307
127 GLU N N 116.921
128 ALA CA C 49.265
128 ALA CB C 16.097
128 ALA H H 7.188
128 ALA HA H 4.257
128 ALA HB H 1.361
128 ALA N N 119.386
129 ASP CA C 49.543
129 ASP CB C 36.452
129 ASP H H 7.721
129 ASP HA H 4.513
129 ASP HB2 H 2.332
129 ASP HB3 H 2.332
129 ASP N N 117.657
130 ILE CA C 60.632
130 ILE CB C 35.636
130 ILE CG1 C 25.118
130 ILE CG2 C 14.492
130 ILE CD1 C 9.612
130 ILE H H 8.197
130 ILE HA H 3.868
130 ILE HB H 1.958
130 ILE HG12 H 1.285
130 ILE HG13 H 1.285
130 ILE HG2 H 0.895
130 ILE HD1 H 0.845
130 ILE N N 128.492
131 ASP CA C 51.121
131 ASP CB C 38.563
131 ASP H H 8.167
131 ASP HA H 4.582
131 ASP HB2 H 2.624
131 ASP HB3 H 2.624
131 ASP N N 117.245
132 GLY CA C 44.672
132 GLY H H 7.440
132 GLY HA2 H 3.801
132 GLY HA3 H 3.801
132 GLY N N 109.147
133 ASP CA C 50.981
133 ASP H H 8.196
133 ASP HA H 4.575
133 ASP HB2 H 2.636
133 ASP HB3 H 2.636
133 ASP N N 121.555
134 GLY CA C 42.909
134 GLY H H 10.217
134 GLY HA2 H 4.006
134 GLY HA3 H 4.006
134 GLY N N 113.583
135 GLN CA C 50.425
135 GLN CB C 29.930
135 GLN CG C 30.473
135 GLN H H 7.819
135 GLN HA H 4.838
135 GLN HB2 H 1.661
135 GLN HB3 H 1.661
135 GLN HG2 H 1.906
135 GLN HG3 H 1.906
135 GLN N N 116.063
136 VAL CA C 59.008
136 VAL CB C 30.775
136 VAL CG1 C
19.122
136 VAL H H 9.001
136 VAL HA H 5.167
136 VAL HB H 2.254
136 VAL HG1 H 1.226
136 VAL HG2 H 0.888
136 VAL N N 126.088
137 ASN CA C 48.383
137 ASN H H 9.370
137 ASN HA H 5.137
137 ASN HB2 H 2.751
137 ASN HB3 H 2.479
137 ASN N N 129.697
138 TYR CA C 59.965
138 TYR CB C 34.840
138 TYR H H 8.313
138 TYR HA H 3.373
138 TYR HB2 H 2.327
138 TYR HB3 H 2.327
138 TYR N N 119.170
139 GLU CA C 56.707
139 GLU CB C 26.203
139 GLU CG C 33.545
139 GLU H H 8.012
139 GLU HA H 3.997
139 GLU HB2 H 2.063
139 GLU HB3 H 2.009
139 GLU HG2 H 2.357
139 GLU HG3 H 2.312
139 GLU N N 119.324
140 GLU CA C 55.760
140 GLU CB C 26.455
140 GLU CG C 33.296
140 GLU H H 8.624
140 GLU HA H 4.069
140 GLU HB2 H 2.069
140 GLU HB3 H 2.015
140 GLU HG2 H 2.354
140 GLU HG3 H 2.320
140 GLU N N 120.448
141 PHE CA C 58.961
141 PHE CB C 37.262
141 PHE H H 8.781
141 PHE HA H 3.917
141 PHE N N 125.424
142 VAL CA C 64.297
142 VAL CB C 28.735
142 VAL CG1 C
20.048
142 VAL CG2 C
20.048
142 VAL H H 8.436
142 VAL HA H 3.068
142 VAL HB H 1.806
142 VAL HG1 H 0.446
142 VAL HG2 H 0.446
142 VAL N N 120.162
143 GLN CA C 56.131
143 GLN CB C 25.436
143 GLN CG C 31.282
143 GLN H H 7.286
143 GLN HA H 3.792
143 GLN HB2 H 2.086
143 GLN HB3 H 2.086
143 GLN HG2 H 2.366
143 GLN HG3 H 2.366
143 GLN N N 118.871
144 MET CA C 58.850
144 MET CB C 36.968
144 MET CG C 37.402
144 MET H H 7.775
144 MET HA H 3.923
144 MET HB2 H 2.003
144 MET HB3 H 2.004
144 MET HG2 H 2.319
144 MET HG3 H 2.319
144 MET N N 119.756
145 MET CA C 52.559
145 MET CB C 29.170
145 MET CG C 29.713
145 MET CE C 15.122
145 MET H H 7.705
145 MET HA H 4.246
145 MET HB2 H 1.620
145 MET HB3 H 1.620
145 MET HG2 H 1.749
145 MET HG3 H 1.749
145 MET HE H 1.924
145 MET N N 115.739
147 ALA CA C 50.100
147 ALA CB C 16.269
147 ALA H H 7.598
147 ALA HA H 4.263
147 ALA HB H 1.355
147 ALA N N 127.202
148 LYS CA C 54.739
148 LYS CB C 26.274
148 LYS CG C 21.815
148 LYS CD C 30.787
148 LYS CE C 39.649
148 LYS H H 7.576
148 LYS HA H 4.072
148 LYS HB2 H 1.621
148 LYS HB3 H 1.621
148 LYS HG2 H 1.350
148 LYS HG3 H 1.350
148 LYS HD2 H 1.767
148 LYS HD3 H 1.767
148 LYS HE2 H 2.927
148 LYS HE3 H 2.927
148 LYS N N 126.240

Bibliography

(1) Clapham, D. E. Calcium Signaling. *Cell* **2007**, *131* (6), 1047–1058. https://doi.org/10.1016/j.cell.2007.11.028.

(2) Berridge, M. J.; Bootman, M. D.; Lipp, P. Calcium - a Life and Death Signal. *Nature* **1998**, *395* (6703), 645–648. https://doi.org/10.1038/27094.

(3) Evenäs, J.; Malmendal, A.; Forsén, S. Calcium. *Curr. Opin. Chem. Biol.* **1998**, *2* (2), 293–302. https://doi.org/10.1016/S1367-5931(98)80072-0.

(4) Babu, Y. S.; Bugg, C. E.; Cook, W. J. Structure of Calmodulin Refined at 2.2 Å Resolution. *J. Mol. Biol.* **1988**, *204* (1), 191–204. https://doi.org/10.1016/0022-2836(88)90608-0.

(5) Strynadka, N. C. J.; James, M. N. G. Crystal Structures of the Helix-Loop-Helix Calcium-Binding Proteins. *Annu. Rev. Biochem.* **1989**, *58* (1), 951–999. https://doi.org/10.1146/annurev.bi.58.070189.004511.

(6) Ikura, M. Calcium Binding and Conformational Response in EF-Hand Proteins. *Trends in Biochemical Sciences*. **1996**, *21* (1), 14–17. https://doi.org/10.1016/S0968-0004(06)80021-6.

(7) Ikura, M.; Ames, J. B. Genetic Polymorphism and Protein Conformational Plasticity in the Calmodulin Superfamily: Two Ways to Promote Multifunctionality. *Proc. Natl. Acad. Sci. U. S. A.* **2006**, *103* (5), 1159–1164. https://doi.org/10.1073/pnas.0508640103.

(8) Stevens, F. C. Calmodulin: An Introduction. *Canadian journal of biochemistry and cell biology = Revue canadienne de biochimie et biologie cellulaire*. **1983**, *61* (1), 906–910. https://doi.org/10.1139/o83-115.

(9) Sparrow, M. P.; Mrwa, U.; Hofmann, F.; Rüegg, J. C. Calmodulin Is Essential for Smooth Muscle Contraction. *FEBS Lett.* **1981**, *125* (2), 141–145. https://doi.org/10.1016/0014-5793(81)80704-1.

(10) Walsh, M. P. Calmodulin and the Regulation of Smooth Muscle Contraction. *Mol. Cell. Biochem.* **1994**, *135* (1), 21–41. https://doi.org/10.1007/bf00925958.

(11) Mizunami, M.; Nemoto, Y.; Terao, K.; Hamanaka, Y.; Matsumoto, Y. Roles of Calcium/Calmodulin-Dependent Kinase II in Long-Term Memory Formation in Crickets. *PLoS One* **2014**, *9* (9), e107442. https://doi.org/10.1371/journal.pone.0107442.

(12) Lisman, J.; Yasuda, R.; Raghavachari, S. Mechanisms of CAMKII Actio in LTP. *Nat. Rev. Neurosci.* **2014**, *13* (3), 169–182. https://doi.org/10.1038/nrn3192.Mechanisms.

(13) Nishizawa, Y.; Okui, Y.; Inaba, M.; Okuno, S.; Yukioka, K.; Miki, T.; Watanabe, Y.; Morii, H. Calcium/Calmodulin-Mediated Action of Calcitonin on Lipid Metabolism in Rats. *J. Clin. Invest.* **1988**, *82* (4), 1165–1172. https://doi.org/10.1172/JCI113713.

(14) Crouchl, T. H.; Klee, C. B. Positive Cooperative Binding of Calcium to Bovine Brain Calmodulin. *Biochemistry* **1980**, *19* (16), 3692–3698. https://doi.org/10.1021/bi00557a009.

(15) Kilhoffer, M. C.; Kubina, M.; Travers, F.; Haiech, J. Use of Engineered Proteins with Internal Tryptophan Reporter Groups and Pertubation Techniques To Probe the Mechanism of Ligand-Protein Interactions: Investigation of the Mechanism of Calcium Binding to Calmodulin. *Biochemistry* **1992**, *31* (34), 8098–8106. https://doi.org/10.1021/bi00149a046.

(16) Zhang, M.; Tanaka, T.; Ikura, M. Calcium-Induced Conformational Transition Revealed

by the Solution Structure of Apo Calmodulin. *Nat. Struct. Biol.* **1995**, *2* (9), 758–767. https://doi.org/10.1038/nsb0995-758.
(17) Gellman, S. H. On the Role of Methionine Residues in the Sequence-Independent Recognition of Nonpolar Protein Surfaces. *Biochemistry* **1991**, *30* (27), 6633–6636. https://doi.org/10.1021/bi00241a001.
(18) Smith, D. M. A.; Straatsma, T. P.; Squier, T. C. Retention of Conformational Entropy upon Calmodulin Binding to Target Peptides Is Driven by Transient Salt Bridges. *Biophys. J.* **2012**, *103* (7), 1576–1584. https://doi.org/10.1016/j.bpj.2012.08.037.
(19) Yamniuk, A. P.; Vogel, H. J. Calmodulin's Flexibility Allows for Promiscuity in Its Interactions with Target Proteins and Peptides. *Appl. Biochem. Biotechnol. - Part B Mol. Biotechnol.* **2004**, *27* (1), 33–57. https://doi.org/10.1385/mb:27:1:33.
(20) Mruk, K.; Farley, B. M.; Ritacco, A. W.; Kobertz, W. R. Calmodulation Meta-Analysis: Predicting Calmodulin Binding via Canonical Motif Clustering. *J. Gen. Physiol.* **2014**, *144* (1), 105–114. https://doi.org/10.1085/jgp.201311140.
(21) Jurado, L. A.; Chockalingam, P. S.; Jarrett, H. W. Apocalmodulin. *Physiological Reviews*. **1999**, *79* (3), 661–682. https://doi.org/10.1152/physrev.1999.79.3.661.
(22) Tidow, H.; Nissen, P. Structural Diversity of Calmodulin Binding to Its Target Sites. In *FEBS Journal*. **2013**, *280* (21), 5551–5565. https://doi.org/10.1111/febs.12296.
(23) Westerlund, A. M.; Delemotte, L. Effect of Ca2+on the Promiscuous Target-Protein Binding of Calmodulin. *PLoS Comput. Biol.* **2018**, *14* (4). https://doi.org/10.1371/journal.pcbi.1006072.
(24) Crivici, A. E.; Ikura, M. Structural Basis of Target Recognition By Calmodulin. *Biophys. Chem.* **1995**, *24*, 85–116. https://doi.org/10.1146/annurev.bb.24.060195.000505
(25) Shirran, S.; Garnaud, P.; Daff, S.; McMillan, D.; Barran, P. The Formation of a Complex between Calmodulin and Neuronal Nitric Oxide Synthase Is Determined by ESI-MS. *J. R. Soc. Interface* **2005**, *2* (5), 465–476. https://doi.org/10.1098/rsif.2005.0055.
(26) Janssens, S. P. Encoding Human Endothelium- Derived Relaxing Factor / Nitric Oxide Synthase. *Biochemistry* **1992**, *267* (21), 14519–14522.
(27) Alderton, W. K.; Cooper, C. E.; Knowles, R. G. Nitric Oxide Synthases: Structure, Function and Inhibition. *Biochem. J.* **2001**, *357* (3), 593–615. https://doi.org/10.1042/0264-6021:3570593.
(28) Piazza, M.; Futrega, K.; Spratt, D. E.; Dieckmann, T.; Guillemette, J. G. Structure and Dynamics of Calmodulin (CaM) Bound to Nitric Oxide Synthase Peptides: Effects of a Phosphomimetic CaM Mutation. *Biochemistry* **2012**, *51* (17), 3651–3661. https://doi.org/10.1021/bi300327z.
(29) Zhang, J.; Martàsek, P.; Paschke, R.; Shea, T.; Masters, B. S. S.; Kim, J. J. P. Crystal Structure of the FAD/NADPH-Binding Domain of Rat Neuronal Nitric-Oxide Synthase: Comparisons with NADPH-Cytochrome P450 Oxidoreductase. *J. Biol. Chem.* **2001**, *276* (40), 37506–37513. https://doi.org/10.1074/jbc.M105503200.
(30) Förstermann, U.; Sessa, W. C. Nitric Oxide Synthases: Regulation and Function. *Eur. Heart J.* **2012**, *33* (7), 829–837. https://doi.org/10.1093/eurheartj/ehr304.
(31) Landskron, G.; De La Fuente, M.; Thuwajit, P.; Thuwajit, C.; Hermoso, M. A. Chronic Inflammation and Cytokines in the Tumor Microenvironment. *Journal of Immunology Research*. **2014**, 149185. https://doi.org/10.1155/2014/149185.
(32) Knowles, R. G.; Moncada, S. Nitric Oxide Synthases in Mammals. *Biochem. J.* **1994**, *298* (2), 249–258. https://doi.org/10.1042/bj2980249.

(33) Stateva, S. R.; Salas, V.; Benaim, G.; Menéndez, M.; Solís, D.; Villalobo, A. Characterization of Phospho-(Tyrosine)-Mimetic Calmodulin Mutants. *PLoS One* **2015**, *10* (4), 1–20. https://doi.org/10.1371/journal.pone.0120798.
(34) Aoyagi, M.; Arvai, A. S.; Tainer, J. A.; Getzoff, E. D. Structural Basis for Endothelial Nitric Oxide Synthase Binding to Calmodulin. *EMBO J.* **2003**, *22* (4), 766–775. https://doi.org/10.1093/emboj/cdg078.
(35) Spratt, D. E.; Taiakina, V.; Palmer, M.; Guillemette, J. G. Differential Binding of Calmodulin Domains to Constitutive and Inducible Nitric Oxide Synthase Enzymes. *Biochemistry* **2007**, *46* (28), 8288–8300. https://doi.org/10.1021/bi062130b.
(36) Garcin, E. D.; Bruns, C. M.; Lloyd, S. J.; Hosfield, D. J.; Tiso, M.; Gachhui, R.; Stuehr, D. J.; Tainer, J. A.; Getzoff, E. D. Structural Basis for Isozyme-Specific Regulation of Electron Transfer in Nitric-Oxide Synthase. *J. Biol. Chem.* **2004**, *279* (36), 37918–37927. https://doi.org/10.1074/jbc.M406204200.
(37) Li, J.; Zheng, H.; Feng, C. Deciphering Mechanism of Conformationally Controlled Electron Transfer in Nitric Oxide Synthases. *Front. Biosci. - Landmark* **2018**, *23*, 1803-1821. https://doi.org/10.2741/4674.
(38) Marletta, M. A.; Hurshman, A. R.; Rusche, K. M. Catalysis by Nitric Oxide Synthase. *Curr. Opin. Chem. Biol.* **1998**, *2* (5), 656–663. https://doi.org/10.1016/S1367-5931(98)80098-7.
(39) Li, D.; Kabir, M.; Stuehr, D. J.; Rousseau, D. L.; Yeh, S. R. Substrate- and Isoform-Specific Dioxygen Complexes of Nitric Oxide Synthase. *J. Am. Chem. Soc.* **2007**, *129* (21), 6943–6951. https://doi.org/10.1021/ja070683j.
(40) Ghosh, D. K.; Salerno, J. C. Nitric Oxide Synthases: Domain Structure and Alignment in Enzyme Function and Control. *Front. Biosci.* **2003**, *8*, d193-209. https://doi.org/10.2741/959.
(41) Venema, R. C.; Sayegh, H. S.; Kent, J. D.; Harrison, D. G. Identification, Characterization, and Comparison of the Calmodulin-Binding Domains of the Endothelial and Inducible Nitric Oxide Synthases. *J. Biol. Chem.* **1996**, *271* (11), 6435–6440. https://doi.org/10.1074/jbc.271.11.6435.
(42) Venema, V. J.; Ju, H.; Zou, R.; Venema, R. C. Interaction of Neuronal Nitric-Oxide Synthase with Caveolin-3 in Skeletal Muscle: Identification of a Novel Caveolin Scaffolding/Inhibitory Domain. *J. Biol. Chem.* **1997**, *272* (45), 28187–28190. https://doi.org/10.1074/jbc.272.45.28187.
(43) Mukherjee, P.; Cinelli, M. A.; Kang, S.; Silverman, R. B. Development of Nitric Oxide Synthase Inhibitors for Neurodegeneration and Neuropathic Pain. *Chem. Soc. Rev.* **2014**, *43* (19), 6814–6838. https://doi.org/10.1039/c3cs60467e.
(44) Steinert, J. R.; Robinson, S. W.; Tong, H.; Haustein, M. D.; Kopp-Scheinpflug, C.; Forsythe, I. D. Nitric Oxide Is an Activity-Dependent Regulator of Target Neuron Intrinsic Excitability. *Neuron* **2011**, *71* (2), 291–305. https://doi.org/10.1016/j.neuron.2011.05.037.
(45) Malinski, T.; Bailey, F.; Zhang, Z. G.; Chopp, M. Nitric Oxide Measured by a Porphyrinic Microsensor in Rat Brain after Transient Middle Cerebral Artery Occlusion. *J. Cereb. Blood Flow Metab.* **1993**, *13* (3), 355–358. https://doi.org/10.1038/jcbfm.1993.48.
(46) Blough, N. V.; Zafiriou, O. C. Reaction of Superoxide with Nitric Oxide to Form Peroxonitrite in Alkaline Aqueous Solution. *Inorg. Chem.* **1985**, *24* (22), 3502–3504. https://doi.org/10.1021/ic00216a003.

(47) Lipton, S. A.; Choi, Y. B.; Pan, Z. H.; Lei, S. Z.; Chen, H. S. V.; Sucher, N. J.; Loscalzo, J.; Singel, D. J.; Stamler, J. S. A Redox-Based Mechanism for the Neuroprotective and Neurodestructive Effects of Nitric Oxide and Related Nitroso-Compounds. *Nature* **1993**, *364* (6438), 626–632. https://doi.org/10.1038/364626a0.
(48) Bossy-Wetzel, E.; Talantova, M. V.; Lee, W. D.; Schölzke, M. N.; Harrop, A.; Mathews, E.; Götz, T.; Han, J.; Ellisman, M. H.; Perkins, G. A.; Lipton, S. A. Crosstalk between Nitric Oxide and Zinc Pathways to Neuronal Cell Death Involving Mitochondrial Dysfunction and P38-Activated K+ Channels. *Neuron* **2004**, *41* (3), 351–365. https://doi.org/10.1016/S0896-6273(04)00015-7.
(49) Dorheim, M. A.; Tracey, W. R.; Pollock, J. S.; Grammas, P. Nitric Oxide Synthase Activity Is Elevated in Brain Microvessels in Alzheimer′s Disease. *Biochem. Biophys. Res. Commun.* **1994**, *205* (1), 659–665. https://doi.org/10.1006/bbrc.1994.2716.
(50) Chung, K. K. K.; Thomas, B.; Li, X.; Pletnikova, O.; Troncoso, J. C.; Marsh, L.; Dawson, V. L.; Dawson, T. M. S-Nitrosylation of Parkin Regulates Ubiquitination and Compromises Parkin's Protective Function. *Science* **2004**, *304* (5675), 1328–1331. https://doi.org/10.1126/science.1093891.
(51) Zhu, X.; Dong, J.; Han, B.; Huang, R.; Zhang, A.; Xia, Z.; Chang, H.; Chao, J.; Yao, H. Neuronal Nitric Oxide Synthase Contributes to PTZ Kindling Epilepsy-Induced Hippocampal Endoplasmic Reticulum Stress and Oxidative Damage. *Front. Cell. Neurosci.* **2017**, *11*, 377. https://doi.org/10.3389/fncel.2017.00377.
(52) Lipton, P. Ischemic Cell Death in Brain Neurons. *Physiological Reviews*. **1999**, *79* (4), 1431–1568. https://doi.org/10.1152/physrev.1999.79.4.1431.
(53) Hantraye, P.; Brouillet, E.; Ferrante, R.; Palfi, S.; Dolan, R.; Matthews, R. T.; Beal, M. F. Inhibition of Neuronal Nitric Oxide Synthase Prevents MPTP-Induced Parkinsonism in Baboons. *Nat. Med.* **1996**, *2* (9), 1017–1021. https://doi.org/10.1038/nm0996-1017.
(54) Kazakov, A.; Hall, R.; Jagoda, P.; Bachelier, K.; Müller-Best, P.; Semenov, A.; Lammert, F.; Böhm, M.; Laufs, U. Inhibition of Endothelial Nitric Oxide Synthase Induces and Enhances Myocardial Fibrosis. *Cardiovasc. Res.* **2013**, *100* (2), 211–221. https://doi.org/10.1093/cvr/cvt181.
(55) Jones, S. P.; Greer, J. J. M.; Van Haperen, R.; Duncker, D. J.; De Crom, R.; Lefer, D. J. Endothelial Nitric Oxide Synthase Overexpression Attenuates Congestive Heart Failure in Mice. *Proc. Natl. Acad. Sci. U. S. A.* **2003**, *100* (8), 4891–4896. https://doi.org/10.1073/pnas.0837428100.
(56) Banerjee, S.; Melnyk, S. B.; Krager, K. J.; Aykin-Burns, N.; McCullough, S. S.; James, L. P.; Hinson, J. A. Trifluoperazine Inhibits Acetaminophen-Induced Hepatotoxicity and Hepatic Reactive Nitrogen Formation in Mice and in Freshly Isolated Hepatocytes. *Toxicol. Reports* **2017**, *4*, 134–142. https://doi.org/10.1016/j.toxrep.2017.02.005.
(57) Mittal, C. K.; Jadhav, A. L. Calcium-Dependent Inhibition of Constitutive Nitric Oxide Synthase. *Biochem. Biophys. Res. Commun.* **1994**, *203* (1), 8–15. https://doi.org/10.1006/bbrc.1994.2141.
(58) Cook, W. J.; Walter, L. J.; Walter, M. R. Drug Binding by Calmodulin: Crystal Structure of a Calmodulin-Trifluoperazine Complex. *Biochemistry* **1994**, *33* (51), 15259–15265. https://doi.org/10.1021/bi00255a006.
(59) Vandonselaar, M.; Hickie, R. A.; Quail, J. W.; Delbaere, L. T. J. Trifluoperazine-Induced Conformational Change in Ca2+-Calmodulin. *Nat. Struct. Biol.* **1994**, *1* (11), 795–801. https://doi.org/10.1038/nsb1194-795.

(60) Polischouk, A. G.; Holgersson, Å.; Zong, D.; Stenerlöw, B.; Karlsson, H. L.; Möller, L.; Viktorsson, K.; Lewensohn, R. The Antipsychotic Drug Trifluoperazine Inhibits DNA Repair and Sensitizes Non-Small Cell Lung Carcinoma Cells to DNA Double-Strand Break-Induced Cell Death. *Mol. Cancer Ther.* **2007**, *6* (8), 2303–2309. https://doi.org/10.1158/1535-7163.MCT-06-0402.

(61) León, J.; Macías, M.; Escames, G.; Camacho, E.; Khaldy, H.; Martín, M.; Espinosa, A.; Gallo, M. A.; Acuña-Castroviejo, D. Structure-Related Inhibition of Calmodulin-Dependent Neuronal Nitric-Oxide Synthase Activity by Melatonin and Synthetic Kynurenines. *Mol. Pharmacol.* **2000**, *58* (5), 967–975. https://doi.org/10.1124/mol.58.5.967.

(62) León, J.; Escames, G.; Rodríguez, M. I.; López, L. C.; Tapias, V.; Entrena, A.; Camacho, E.; Carrión, M. D.; Gallo, M. A.; Espinosa, A.; Tan, D. X.; Reiter, R. J.; Acuña-Castroviejo, D. Inhibition of Neuronal Nitric Oxide Synthase Activity by N 1-Acetyl-5-Methoxykynuramine, a Brain Metabolite of Melatonin. *J. Neurochem.* **2006**, *98* (6), 2023–2033. https://doi.org/10.1111/j.1471-4159.2006.04029.x.

(63) E. Camacho, M.; D. Carrion, M.; C. Lopez-Cara, L.; Entrena, A.; A. Gallo, M.; Espinosa, A.; Escames, G.; Acuna-Castroviejo, D. Melatonin Synthetic Analogs as Nitric Oxide Synthase Inhibitors. *Mini-Reviews Med. Chem.* **2012**, *12* (7), 600–617. https://doi.org/10.2174/138955712800626674.

(64) Lerner, A. B.; Case, J. D.; Takahashi, Y.; Lee, T. H.; Mori, W. Isolation of Melatonin, the Pineal Gland Factor That Lightens Melanocytes. *J. Am. Chem. Soc.* **1958**, *80* (10), 2587. https://doi.org/10.1021/ja01543a060.

(65) Reiter, R. J. The Melatonin Rhythm: Both a Clock and a Calendar. *Experientia* **1993**, *49* (8), 654–664. https://doi.org/10.1007/BF01923947.

(66) Hardeland, R. Antioxidative Protection by Melatonin: Multiplicity of Mechanisms from Radical Detoxification to Radical Avoidance. *Endocrine* **2005**, *27* (2), 119–130. https://doi.org/10.1385/ENDO:27:2:119.

(67) Morgan, P. J.; Barrett, P.; Howell, H. E.; Helliwell, R. Melatonin Receptors: Localization, Molecular Pharmacology and Physiological Significance. *Neurochemistry International*. **1994**, *24* (2), 101–146 https://doi.org/10.1016/0197-0186(94)90100-7.

(68) Dubocovich, M. L.; Markowska, M. Functional MT 1 and MT 2 Melatonin Receptors in Mammals. *Endocrine*. **2005**, *27* (2), 101–110. https://doi.org/10.1385/ENDO:27:2:101.

(69) Peschke, E.; Mühlbauer, E.; Mußhoff, U.; Csernus, V. J.; Chankiewitz, E.; Peschke, D. Receptor (MT1) Mediated Influence of Melatonin on CAMP Concentration and Insulin Secretion of Rat Insulinoma Cells INS-1. *J. Pineal Res.* **2002**, *33* (2), 63–71. https://doi.org/10.1034/j.1600-079X.2002.02919.x.

(70) Hardeland, R. Taxon- and Site-Specific Melatonin Catabolism. *Molecules* **2017**, *22* (11), 2015. https://doi.org/10.3390/molecules22112015.

(71) Benítez-King, G.; Huerto-Delgadillo, L.; Antón-Tay, F. Binding of 3H-Melatonin to Calmodulin. *Life Sci.* **1993**, *53* (3), 201–207. https://doi.org/10.1016/0024-3205(93)90670-X.

(72) Romero, M. P.; García-Pergañeda, A.; Guerrero, J. M.; Osuna, C. Membrane-bound Calmodulin in Xenopus Laevis Oocytes as a Novel Binding Site for Melatonin. *FASEB J.* **1998**, *12* (13), 1401–1408. https://doi.org/10.1096/fasebj.12.13.1401.

(73) Ouyang, H.; Vogel, H. J. Melatonin and Serotonin Interactions with Calmodulin: NMR, Spectroscopic and Biochemical Studies. *Biochim. Biophys. Acta - Protein Struct. Mol.*

Enzymol. **1998**, *1383* (1), 37–47. https://doi.org/10.1016/S0167-4838(97)00157-X.
(74) Turjanski, A. G.; Estrin, D. A.; Rosenstein, R. E.; McCormick, J. E.; Martin, S. R.; Pastore, A.; Biekofsky, R. R.; Martorana, V. NMR and Molecular Dynamics Studies of the Interaction of Melatonin with Calmodulin. *Protein Sci.* **2008**, *13* (11), 2925–2938. https://doi.org/10.1110/ps.04611404.
(75) Pozo, D.; Reiter, R. J.; Calvo, J. R.; Guerrero, J. M. Inhibition of Cerebellar Nitric Oxide Synthase and Cyclic GMP Production by Melatonin via Complex Formation with Calmodulin. *J. Cell. Biochem.* **1997**, *65* (3), 430–442. https://doi.org/10.1002/(SICI)1097-4644(19970601)65:3<430::AID-JCB12>3.0.CO;2-J.
(76) Widmer, H.; Wüthrich, K. Simulation of Two-Dimensional NMR Experiments Using Numerical Density Matrix Calculations. *J. Magn. Reson.* **1986**, *70* (2), 270–279. https://doi.org/10.1016/0022-2364(86)90009-0.
(77) Vogt, F. G. Nuclear Magnetic Resonance. *Analytical Instrumentation Handbook, Third Edition*. **2004**. https://doi.org/10.1201/9781420078930.ch6.
(78) Marion, D.; Driscoll, P. C.; Kay, L. E.; Wingfield, P. T.; Bax, A.; Gronenborn, A. M.; Clore, G. M. Overcoming the Overlap Problem in the Assignment of 1H NMR Spectra of Larger Proteins by Use of Three-Dimensional Heteronuclear 1H-15N Hartmann-Hahn-Multiple Quantum Coherence and Nuclear Overhauser-Multiple Quantum Coherence Spectroscopy: Application to Interleukin 1 Beta . *Biochemistry* **1989**, *28* (15), 6150–6156. https://doi.org/10.1021/bi00441a004.
(79) Fu, Y.; Zhao, J.; Chen, Z. Insights into the Molecular Mechanisms of Protein-Ligand Interactions by Molecular Docking and Molecular Dynamics Simulation: A Case of Oligopeptide Binding Protein. *Comput. Math. Methods Med.* **2018**, *2018,* 1–12. https://doi.org/10.1155/2018/3502514.
(80) Swegat, W.; Schlitter, J.; Krüger, P.; Wollmer, A. MD Simulation of Protein-Ligand Interaction: Formation and Dissociation of an Insulin-Phenol Complex. *Biophys. J.* **2003**, *84* (3), 1493–1506. https://doi.org/10.1016/S0006-3495(03)74962-5.
(81) Salmaso, V.; Moro, S. Bridging Molecular Docking to Molecular Dynamics in Exploring Ligand-Protein Recognition Process: An Overview. *Frontiers in Pharmacology.* **2018**, *9,* 923. https://doi.org/10.3389/fphar.2018.00923.
(82) Guedes, I. A.; de Magalhães, C. S.; Dardenne, L. E. Receptor-Ligand Molecular Docking. *Biophysical Reviews*. **2014**, *6* (1), 75–87. https://doi.org/10.1007/s12551-013-0130-2.
(83) Loria, J. P.; Rance, M.; Palmer, A. G. Transverse-Relaxation-Optimized (TROSY) Gradient-Enhanced Triple-Resonance NMR Spectroscopy. *Journal of Magnetic Resonance*. **1999**, *141* (1), 180–184. https://doi.org/10.1006/jmre.1999.1891.
(84) Brooks, B. R.; Brooks, C. L.; Mackerell, A. D.; Nilsson, L.; Petrella, R. J.; Roux, B.; Won, Y.; Archontis, G.; Bartels, C.; Boresch, S.; Caflisch, A.; Caves, L.; Cui, Q.; Dinner, A. R.; Feig, M.; Fischer, S.; Gao, J.; Hodoscek, M.; Im, W.; Kuczera, K.; Lazaridis, T.; Ma, J.; Ovchinnikov, V.; Paci, E.; Pastor, R. W.; Post, C. B.; Pu, J. Z.; Schaefer, M.; Tidor, B.; Venable, R. M.; Woodcock, H. L.; Wu, X.; Yang, W.; York, D. M.; Karplus, M. CHARMM: The Biomolecular Simulation Program. *J. Comput. Chem.* **2009**, *30* (10), 1545–1614. https://doi.org/10.1002/jcc.21287.
(85) Schmid, N.; Christ, C. D.; Christen, M.; Eichenberger, A. P.; Van Gunsteren, W. F. Architecture, Implementation and Parallelisation of the GROMOS Software for Biomolecular Simulation. *Comput. Phys. Commun.* **2012**, *183,* 890–903. https://doi.org/10.1016/j.cpc.2011.12.014.

(86) Jorgensen, W. L.; Tirado-Rives, J. The OPLS Potential Functions for Proteins. Energy Minimizations for Crystals of Cyclic Peptides and Crambin. *J. Am. Chem. Soc.* **1988**, *110* (6), 1657–1666. https://doi.org/10.1021/ja00214a001.
(87) Case, D. A.; Cheatham, T. E.; Darden, T.; Gohlke, H.; Luo, R.; Merz, K. M.; Onufriev, A.; Simmerling, C.; Wang, B.; Woods, R. J. The Amber Biomolecular Simulation Programs. *Journal of Computational Chemistry*. **2005**, *26* (16), 1668–1688. https://doi.org/10.1002/jcc.20290.
(88) Fernando, P.; Abdulle, R.; Mohindra, A.; Guillemette, J. G.; Heikkila, J. J. Mutation or Deletion of the C-Terminal Tail Affects the Function and Structure of Xenopus Laevis Small Heat Shock Protein, Hsp30. *Comp. Biochem. Physiol. - B Biochem. Mol. Biol.* **2002**, *133* (1), 95–103. https://doi.org/10.1016/S1096-4959(02)00110-0.
(89) Benesch, R. E.; Benesch, R.; Yung, S. Equations for the Spectrophotometric Analysis of Hemoglobin Mixtures. *Anal. Biochem.* **1973**, *55* (1), 245–248. https://doi.org/10.1016/0003-2697(73)90309-6.
(90) Hevel, J. M.; Marletta, M. A. Nitric-Oxide Synthase Assays. *Methods Enzymol.* **1994**, *233,* 250–258. https://doi.org/10.1016/S0076-6879(94)33028-X.
(91) Gross, S. S. Microtiter Plate Assay for Determining Kinetics of Nitric Oxide Synthesis. *Methods Enzymol.* **1996**, *12* (3), 275–279. https://doi.org/10.1016/s0076-6879(96)68018-5.
(92) Micsonai, A.; Wien, F.; Bulyáki, É.; Kun, J.; Moussong, É.; Lee, Y. H.; Goto, Y.; Réfrégiers, M.; Kardos, J. BeStSel: A Web Server for Accurate Protein Secondary Structure Prediction and Fold Recognition from the Circular Dichroism Spectra. *Nucleic Acids Res.* **2018**, *46*, 315–322. https://doi.org/10.1093/nar/gky497.
(93) Micsonai, A.; Wien, F.; Kernya, L.; Lee, Y. H.; Goto, Y.; Réfrégiers, M.; Kardos, J. Accurate Secondary Structure Prediction and Fold Recognition for Circular Dichroism Spectroscopy. *Proc. Natl. Acad. Sci. U. S. A.* **2015**, *112* (24), 3095–3103. https://doi.org/10.1073/pnas.1500851112.
(94) Vermeer, L. S.; Marquette, A.; Schoup, M.; Fenard, D.; Galy, A.; Bechinger, B. Simultaneous Analysis of Secondary Structure and Light Scattering from Circular Dichroism Titrations: Application to Vectofusin-1. *Sci. Rep.* **2016**, *6*, 1–7. https://doi.org/10.1038/srep39450.
(95) Shepherd, N. E.; Hoang, H. N.; Abbenante, G.; Fairlie, D. P. Single Turn Peptide Alpha Helices with Exceptional Stability in Water. *J. Am. Chem. Soc.* **2005**, *127* (9), 2974–2983. https://doi.org/10.1021/ja0456003.
(96) Chin, D. H.; Woody, R. W.; Rohl, C. A.; Baldwin, R. L. Circular Dichroism Spectra of Short, Fixed-Nucleus Alanine Helices. *Proc. Natl. Acad. Sci. U. S. A.* **2002**, *99* (24), 15416–15421. https://doi.org/10.1073/pnas.232591399.
(97) Wang, D.; Chen, K.; Kulp, J. L.; Arora, P. S. Evaluation of Biologically Relevant Short α-Helices Stabilized by a Main-Chain Hydrogen-Bond Surrogate. *J. Am. Chem. Soc.* **2006**, *128* (28), 9248–9256. https://doi.org/10.1021/ja062710w.
(98) Matsubara, M.; Hayashi, N.; Titani, K.; Taniguchi, H. Circular Dichroism and 1H NMR Studies on the Structures of Peptides Derived from the Calmodulin-Binding Domains of Inducible and Endothelial Nitric-Oxide Synthase in Solution and in Complex with Calmodulin: Nascent α- Helical Structures Are Stabilized By . *J. Biol. Chem.* **1997**, *272*, 23050–23056. https://doi.org/10.1074/jbc.272.37.23050.
(99) Lee, S. J.; Stull, J. T. Calmodulin-Dependent Regulation of Inducible and Neuronal Nitric-

Oxide Synthase. *J. Biol. Chem.* **1998**, *273* (42), 27430–27437. https://doi.org/10.1074/jbc.273.42.27430.
(100) Vorherr, T.; Knöpfel, L.; Hofmann, F.; Carafoli, E.; Mollner, S.; Pfeuffer, T. The Calmodulin Binding Domain of Nitric Oxide Synthase and Adenylyl Cyclase. *Biochemistry* **1993**, *32* (23), 6081–6088. https://doi.org/10.1021/bi00074a020.
(101) Censarek, P.; Beyermann, M.; Koch, K. W. Target Recognition of Apocalmodulin by Nitric Oxide Synthase I Peptides. *Biochemistry* **2002**, *41* (27), 8598–8604. https://doi.org/10.1021/bi025681k.
(102) Turnbull, W. B. Divided We Fall? Studying Low Affinity Fragments of Ligands by ITC. *Microcal Appl. notes* **2005**.
(103) Zhang, Y. L.; Zhang, Z. Y. Low-Affinity Binding Determined by Titration Calorimetry Using a High- Affinity Coupling Ligand: A Thermodynamic Study of Ligand Binding to Protein Tyrosine Phosphatase 1B. *Anal. Biochem.* **1998**, *275* (44), 34205–34212. https://doi.org/10.1006/abio.1998.2738.
(104) Taiakina, V.; Boone, A. N.; Fux, J.; Senatore, A.; Weber-Adrian, D.; Guillemette, J. G.; Spafford, J. D. The Calmodulin-Binding, Short Linear Motif, NSCaTE Is Conserved in L-Type Channel Ancestors of Vertebrate Cav1.2 and Cav1.3 Channels. *PLoS One* **2013**, *9* (1). https://doi.org/10.1371/journal.pone.0061765.
(105) Bredt, D. S.; Snyder, S. H. Nitric Oxide Mediates Glutamate-Linked Enhancement of CGMP Levels in the Cerebellum. *Proc. Natl. Acad. Sci. U. S. A.* **1989**, *86* (22), 9030–9033. https://doi.org/10.1073/pnas.86.22.9030.
(106) Liu, L.; Labani, N.; Cecon, E.; Jockers, R. Melatonin Target Proteins: Too Many or Not Enough? *Frontiers in Endocrinology*. **2019**, *10*, 791. https://doi.org/10.3389/fendo.2019.00791.
(107) Piazza, M.; Dieckmann, T.; Guillemette, J. G. Structural Studies of a Complex between Endothelial Nitric Oxide Synthase and Calmodulin at Physiological Calcium Concentration. *Biochemistry* **2016**, *55* (42), 5962–5971. https://doi.org/10.1021/acs.biochem.6b00821.
(108) Piazza, M.; Guillemette, J. G.; Dieckmann, T. Dynamics of Nitric Oxide Synthase-Calmodulin Interactions at Physiological Calcium Concentrations. *Biochemistry* **2015**, *54* (11), 1989–2000. https://doi.org/10.1021/bi501353s.
(109) Zoche, M.; Bienert, M.; Beyermann, M.; Koch, K. W. Distinct Molecular Recognition of Calmodulin-Binding Sites in the Neuronal and Macrophage Nitric Oxide Synthases: A Surface Plasmon Resonance Study. *Biochemistry* **1996**, *35* (26), 8742–8747. https://doi.org/10.1021/bi960445t.
(110) Bettahi, I.; Pozo, D.; Osuna, C.; Reiter, R. J.; Acuña-Castroviejo, D.; Guerrero, J. M. Melatonin Reduces Nitric Oxide Synthase Activity in Rat Hypothalamus. *J. Pineal Res.* **1996**, *20* (4), 205–210. https://doi.org/10.1111/j.1600-079X.1996.tb00260.x.
(111) Tamura, E. K.; Silva, C. L. M.; Markus, R. P. Melatonin Inhibits Endothelial Nitric Oxide Production in Vitro. *J. Pineal Res.* **2006**, *41* (3), 267–274. https://doi.org/10.1111/j.1600-079X.2006.00366.x.
(112) Ziarek, J. J.; Peterson, F. C.; Lytle, B. L.; Volkman, B. F. Binding Site Identification and Structure Determination of ProteinLigand Complexes by NMR: A Semiautomated Approach. In *Methods in Enzymology*. **2011**, *493*, 241–275. https://doi.org/10.1016/B978-0-12-381274-2.00010-8.
(113) Keller, R. Optimizing the Process of Nuclear Magnetic Resonance Spectrum Analysis and

Computer Aided Resonance Assignment. *Swiss Fed. Inst. Technol. Zurich* **2004**. https://doi.org/citeulike-article-id:3918632.
(114) Grzesiek, S.; Bax, A. Correlating Backbone Amide and Side Chain Resonances in Larger Proteins by Multiple Relayed Triple Resonance NMR. *J. Am. Chem. Soc.* **1992**, *114* (16), 6291–6293. https://doi.org/10.1021/ja00042a003.
(115) Muhandiram, D. R.; Kay, L. E. Gradient-Enhanced Triple-Resonance Three-Dimensional NMR Experiments with Improved Sensitivity. *J. Magn. Reson. Ser. B* **1994**, *103* (3), 203–216. https://doi.org/10.1006/jmrb.1994.1032.
(116) Bax, A.; Clore, G. M.; Gronenborn, A. M. 1H1H Correlation via Isotropic Mixing of 13C Magnetization, a New Three-Dimensional Approach for Assigning 1H and 13C Spectra of 13C-Enriched Proteins. *J. Magn. Reson.* **1990**, *88,* 425–431. https://doi.org/10.1016/0022-2364(90)90202-K.
(117) Fesik, S. W.; Zuiderweg, E. R. P. Heteronuclear Three-Dimensional NMR Spectroscopy of Isotopically Labelled Biological Macromolecules. *Q. Rev. Biophys.* **1990**, *23* (2), 97–131. https://doi.org/10.1017/S0033583500005515.
(118) Clore, G. M.; Gronenborn, A. M. Structures of Larger Proteins in Solution: Three- and Four-Dimensional Heteronuclear NMR Spectroscopy. *Science* **1991**, *252* (5011), 1390–1399. https://doi.org/10.1126/science.2047852.
(119) Bax, A.; Ikura, M. An Efficient 3D NMR Technique for Correlating the Proton And15N Backbone Amide Resonances with the α-Carbon of the Preceding Residue in Uniformly15N/13C Enriched Proteins. *J. Biomol. NMR* **1991**, *1* (1), 99–104. https://doi.org/10.1007/BF01874573.
(120) Shen, Y.; Delaglio, F.; Cornilescu, G.; Bax, A. TALOS+: A Hybrid Method for Predicting Protein Backbone Torsion Angles from NMR Chemical Shifts. *J. Biomol. NMR* **2009**, *44* (4), 213–223. https://doi.org/10.1007/s10858-009-9333-z.
(121) Brünger, A. T.; Adams, P. D.; Clore, G. M.; Delano, W. L.; Gros, P.; Grossekunstleve, R. W.; Jiang, J. S.; Kuszewski, J.; Nilges, M.; Pannu, N. S.; Read, R. J.; Rice, L. M.; Simonson, T.; Warren, G. L. Crystallography & NMR System: A New Software Suite for Macromolecular Structure Determination. *Acta Crystallogr. Sect. D Biol. Crystallogr.* **1998**, *54*, 905–921. https://doi.org/10.1107/S0907444998003254.
(122) Osawa, M.; Swindells, M. B.; Tanikawa, J.; Tanaka, T.; Mase, T.; Furuya, T.; Ikura, M. Solution Structure of Calmodulin-W-7 Complex: The Basis of Diversity in Molecular Recognition. *J. Mol. Biol.* **1998**, *276* (1), 165–176. https://doi.org/10.1006/jmbi.1997.1524.
(123) Benítez-King, G.; Ríos, A.; Martínez, A.; Antón-Tay, F. In Vitro Inhibition of Ca2+/Calmodulin-Dependent Kinase II Activity by Melatonin. *Biochim. Biophys. Acta - Gen. Subj.* **1996**, *1290* (2), 191–196. https://doi.org/10.1016/0304-4165(96)00025-6.
(124) Zuiderweg, E. R. P. Mapping Protein-Protein Interactions in Solution by NMR Spectroscopy. *Biochemistry* **2002**, *41* (1), 1–7. https://doi.org/10.1021/bi011870b.
(125) Choi, S. B.; Yap, B. K.; Choong, Y. S.; Wahab, H. Molecular Dynamics Simulations in Drug Discovery. *Encycl. Bioinforma. Comput. Biol. ABC Bioinforma.* **2018**, *1–3*, 652–665. https://doi.org/10.1016/B978-0-12-809633-8.20154-4.
(126) Trott, O.; Olson, A. J. AutoDock Vina: Improving the Speed and Accuracy of Docking with a New Scoring Function, Efficient Optimization, and Multithreading. *J. Comput. Chem.* **2009**, *31* (2), 455–461. https://doi.org/10.1002/jcc.21334.
(127) Pettersen, E. F.; Goddard, T. D.; Huang, C. C.; Couch, G. S.; Greenblatt, D. M.; Meng, E.

C.; Ferrin, T. E. UCSF Chimera - A Visualization System for Exploratory Research and Analysis. *J. Comput. Chem.* **2004***, 25* (13), 1605–1612. https://doi.org/10.1002/jcc.20084.
(128) Humphrey, W.; Dalke, A.; Schulten, K. VMD: Visual Molecular Dynamics. *J. Mol. Graph.* **1996**, *14* (1), 33–38. https://doi.org/10.1016/0263-7855(96)00018-5.
(129) Zoete, V.; Cuendet, M. A.; Grosdidier, A.; Michielin, O. SwissParam: A Fast Force Field Generation Tool for Small Organic Molecules. *J. Comput. Chem.* **2011**, *32* (11), 2359–2368. https://doi.org/10.1002/jcc.21816.
(130) Phillips, J. C.; Braun, R.; Wang, W.; Gumbart, J.; Tajkhorshid, E.; Villa, E.; Chipot, C.; Skeel, R. D.; Kalé, L.; Schulten, K. Scalable Molecular Dynamics with NAMD. *Journal of Computational Chemistry*. **2005**, *26* (16), 1781–1802. https://doi.org/10.1002/jcc.20289.